THE HONG KONG POLYTECHNIC UNIVERSITY

DEPARTMENT OF APPLIED PHYSICS

Capacitance Effect on Spin-Torque Oscillators with Thermal Fluctuation

GUAN Bo

A thesis submitted in partial fulfillment of the requirements for the degree of

Master of Philosophy

December 2008

CERTIFICATE OF ORIGINALITY

I hereby declare that this thesis is my own work and that, to the best of my knowledge and belief, it reproduces no material previously published or written nor material which has been accepted for the award of any other degree or diploma, except where due acknowledgement has been made in the text.

_____ (Signed)

GUAN Bo (Name of Student)

05/12/2008 (Date)

Abstract

This thesis describes the theoretical study and numerical simulation of spin-torque oscillators (STOs) based on a typical giant magneto-resistance (GMR) trilayer spin valve system and magnetic tunneling junction (MTJ) structure.

Theory predicted that a spin-polarized current can exert a torque on a nano-scale magnet. This torque can excite magnetization precessional motion with a steady microwave frequency ranging from 5 to 40 GHz that is tunable by adjusting current and applied magnetic field. The quality factor Q can be as high as 18,000. The high Q value and the current tunability of these STOs suggest their potential application in microwave signal processing. However, the very limited power output (typically less than 1 nW) has to be improved dramatically up to about 1 mW for any realistic application.

In our STO model, typical trilayer spin valve device structures have been adopted, with one 'fixed' and one 'free' ferromagnetic layer sepa-

rated by a nonmagnetic spacer. The dynamics of the 'free' layer magnetization is determined by the Landau-Lifshitz-Gilbert-Slonczewski (LLGS) equation. To study the temperature effects on spin torque valve behavior, we model the thermal fluctuations by adding a Langevin random field into the effective field in the LLGS equation. The added thermal field is a fluctuating random field whose statistical properties obey the Gaussian distribution.

The capacitance effect on the microwave power spectra of an STO was initially investigated with thermal fluctuation. Here, an ideal capacitance is connected in parallel with the STO to represent the intrinsic capacitance of the structure or that of connecting leads, and a *dc* current source is applied. The emitted power at a given frequency is derived by Fast Fourier Transform, and the data are fitted to a Lorentzian profile, from which the quality factors Q are calculated. In the presence of thermal fluctuations, the microwave power spectrum gets broadened with increasing temperature. We have found that the capacitance effect does influence the stability of the system, and it can improve the Q factor value of the STO element even in the presence of thermal fluctuation. It is hence possible that one of the underlying reasons for the high quality factors observed in experiments

may be ascribed to either intrinsic or extrinsic sources of capacitance in parallel with the STO.

Apart from the thermal stability, we studied the capacitive tuning effect on oscillation frequencies. The LLGS equation has been developed to simulate the dynamics of precessional modes in the case of MTJ by adding a perpendicular term in the Slonczewski 'in-plane' spin-torque term. It is found that the oscillation frequency only varies with the values of capacitance, and will not change much with the temperature in both GMR and MTJ based situations. The precessional mode is determined by the applied *dc* current and the oscillation frequencies can be tuned by varying the capacitance. For the 'in-plane' (IP) precessional mode, an increase in capacitance would bring about a decrease in oscillation frequency for the GMR configuration; for the 'out-of-plane' (OOP) mode, the frequency shifts in the opposite way. For MTJ, the frequency does not vary monotonically with capacitance, which is quite an unexpected result. When the *dc* current is just below the IP/OOP critical region, where only IP precessional mode is expected, it is found that the mode can be switched to OOP with increasing capacitance. An analytical theory has been borrowed to explain the mechanism.

Acknowledgements

So many people have contributed in different ways towards the publication of this thesis and I feel truly indebted. I am grateful to my supervisors Prof. Franklin G. Shin and Prof. K. H. Wong for guiding me through the M.Phil. study and for proof reading this thesis. Special thanks to Prof. Johan Åkerman for his constant support and encouragement, for his excellent supervision and valuable comments throughout my six-month exchange study in KTH. Thanks to Dr. C. W. Ong, Dr. Y. W. Wong and Dr. Y. M. Poon for always having their office doors open, and for inspiring me with their deep insight in physics and engineering science. Thanks to Ms. Yonnie Cheung for contributing towards the smooth running of the students' affairs.

I would like to thank my colleague in the department for making it a fun place to work, Mr. Z. P. Wu, Mr. M. X. Cao, Ms. M. Chan, Mr. Y. B. Chan, Mr. K. H. Chau, Mr. Y. Jiang, Mr. J. Liu, Ms. C. S. Ng, Ms. R. X. Xiang, Dr. G. Y. Wang, Dr. H. F. Zhang as well as

former members Dr. S. H. Zhang, Dr. J. F. Qu, Ms. Y. M. Zhang, Mr. S. S. Wang, who don't realize what a difference they have made.

I would like to express my gratitude to the Graduate School of The Hong Kong Polytechnic University for financial support.

Needless to say, my friends and family have provided immeasurable support over the last several years. Sincere thanks to them all - this degree would not have been possible without them. Particular thanks to Dr. G. Y. Wang, Dr. Y. Zhou and Mr. Y. Jiang who have experienced all the highs and lows of my adult life since college and given unstinting support. Thanks to my parents for everything, they could not have been better.

Contents

List of Figures

Chapter 1

Introduction

The development of spin-torque oscillators (STOs) opened a possibility for using nano-sized magnetic devices as active microwave elements that do not involve any semiconductor materials (Silva and Rippard, 2008).

Theory predicted (Slonczewski, 1996, 1999; Berger, 1996, 2001) and then experiments verified (Kiselev et al., 2003) that a *dc* applied current propagating through a magnetized magnetic multilayered structure becomes spin-polarized in the direction of the 'fixed' layer magnetization (see Fig. (1.1)) and, if the current density is sufficiently high, this spin-polarized current can transfer the spin angular momentum between the magnetic layers to de-stabilize the equilibrium orientation of magnetization in the 'free' layer of the multilayered structure (Bertotti et al., 2005). This effect is now referred to as Spin-Transfer Torque (STT). Depending on the actual device configuration and properties of the magnetic structure and the magnitude of the external applied magnetic field, this

current-induced de-stabilization can lead either to the switching of the magnetization direction in the 'free' layer (Myers et al., 1999; Katine et al., 2000) or sustain a steady precessional motion of the magnetization by counteracting the Gilbert damping (Kiselev et al., 2003; Rippard et al., 2004; Krivorotov et al., 2005). The stationary precessional motion causes a periodic variation in the resistance of the system, due to giant magneto-resistance (GMR) or tunneling magneto-resistance (TMR) effects, resulting in a detectable *ac* voltage (Kiselev et al., 2003). Such devices, named Spin-Torque Oscillators (STOs), are able to generate frequencies ranging from 5 to 40 GHz, which lie in the microwave range and can be tuned by adjusting the bias magnetic field and the applied current (Kiselev et al., 2003).

As these spin-torque oscillators (STOs) can convert a *dc* applied current into microwave signals, or, convert a microwave signal into a *dc* voltage (Tulapurkar et al., 2005; Sankey et al., 2006b; Fuchs et al., 2007), it opens up a wide range of potential applications for STO as nano-sized microwave generator and detector, such as the development of a chip-scale microwave spectrum analyzer and nano-scale radiation source in wireless communications (Silva and Rippard, 2008).

Barriers to practical applications for the STOs that have yet to be solved include the signal strength and the noise performance (Silva and Rippard, 2008). Although theories have been developed to qualitatively explain the essential prop-

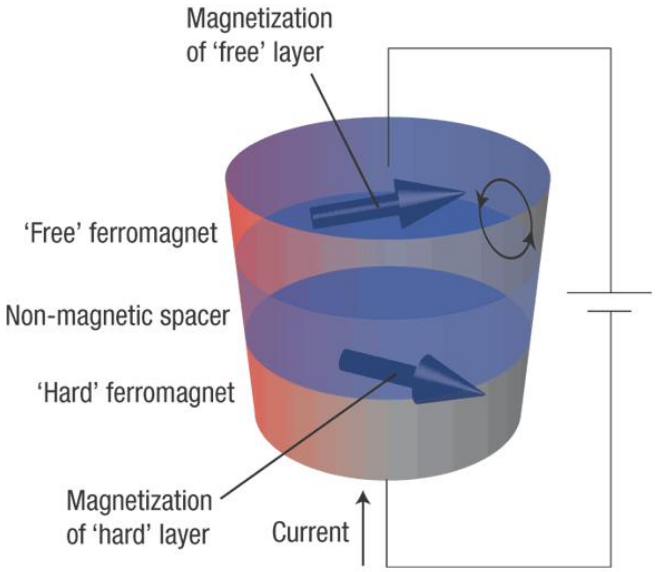

Figure 1.1: The current passing through a 'hard' or 'fixed' layer becomes spin-polarized. When this current is injected into a 'free' magnetic layer, it induces a torque on the magnetic moment, causing the magnetization of the 'free' layer to precess (Tsoi, 2008).

erties (Slavin and Tiberkevich, 2005; Kim et al., 2008), there are still a number of results which have not yet found a satisfactory interpretation, largely because accurate models for quantitative description of the device performance and the microwave properties are still missing.

The theoretical description of the process of microwave excitation by spin-polarized current was developed using many different techniques by different research groups. Several groups developed theories based on the direct analysis of the Landau-Lifshitz-Gilbert (LLG) equation (Slavin and Tiberkevich, 2005; Sun, 2000; Xi and Lin, 2004), while others were using general methods of the non-linear theory of dynamical system (Bertotti et al., 2005; Kim et al., 2008; Serpico et al., 2005; Bonin et al., 2006). Many efforts were directed at the numerical analysis (macrospin modeling and micromagnetic simulations) in different geometries of interest (Lee et al., 2004; Zhu et al., 2004; Berkov and Gorn, 2005; Montigny and Miltat, 2005; Consolo et al., 2007).

However, there remains a great deal of variability in device properties. Since the microwave power generated by STOs is comparable to the noise power in the magnetic material of the 'free' layer at room temperature, it is very important to study the influence of the thermal fluctuation on the operation of STOs (Kim et al., 2008; Tiberkevich et al., 2007). To improve STOs' stability and performance, a clear understanding of the current-induced microwave generation

processes in magnetic nano-structures is necessary for the successful design and optimization of such devices.

The theme of this thesis is the theoretical study and numerical simulation of the capacitance effect on spin-torque oscillators with thermal fluctuation.

Chapter 2 gives a brief review of the general background including different types of magneto-resistance, the issues associated with how spin transfer torques affect magnetic multilayer devices, and description of the possible geometries of magnetic nano-structure that can be used in spin-torque oscillators. A review is also given of the experimental and theoretical work already carried out within the field. Two different subjects are described, which are directly related to the following chapters: (1) the effect of thermal fluctuation on the performance of spin-torque oscillators, and (2) the synchronization of oscillators and other external sources.

The algorithm used in this work is described in Chapter 3, including the introduction of Landau-Lifshitz-Gilbert equation, a detailed description of the macrospin model used in our calculations, and a brief comment on micromagnetic simulations.

Chapter 4 gives the first computational results obtained from the macrospin model showing the influence of the additional capacitance on the thermal stability of the spin-torque oscillator system.

Chapter 5 describes the capacitance tuning effect on the oscillation frequencies, and an analytical framework has been introduced to try to explain the phenomena.

Finally this thesis ends with a summary of the results in Chapter 6 including a section on 'future work'.

Chapter 2

Background and Literature Reviews

2.1 Background

The spin-torque oscillator (STO) is based on the interaction of a spin-polarized current with a magnetic thin layer. This interaction results in two effects: magneto-resistance and spin-transfer torque. Magneto-resistance is the dependence of the electrical resistance on the relative orientation of the magnetization and the spin of the incident electrons. Spin-transfer torque is the torque exerted by the spin-polarized electrons on the magnetic thin layer. In the spin-torque oscillator (STO), the spin-transfer torque is used to drive a GHz oscillation of the magnetization direction of the magnetic thin layer. This oscillation is then transformed into an oscillating electrical signal by the magneto-resistance effect. The electrical signal can be used as a nano-sized reference oscillator in wireless application.

2.1.1 Magneto-resistance

Magneto-resistance (MR) can be defined by the change in the electrical resistance of a substance when an external magnetic field is applied to it. The signal response is often characterized by the percentage MR

$$\mathrm{MR}(\%) = \frac{\Delta R}{R} \tag{2.1}$$

where ΔR is the change in the electrical resistance when an external magnetic field is applied, and R is the resistance in the absence of the applied magnetic field.

MR effects have been discovered in a variety of material systems, for which various physical origins are responsible. In the following, a brief overview of the various MR effects is given.

2.1.1.1 Ordinary Magneto-resistance

When a magnetic field is applied to a metal perpendicular to an electrical field, the Lorentz force affects the trajectories of the incident electrons, giving rise to a change in the transverse resistivity $\Delta\rho_{\perp}$ (see Fig. (2.1)). In general, $\Delta R/R \approx \alpha H^2$, where α is a different constant for each metal (Pippard, 1989). A similar effect is also found when the magnetic field is applied parallel to the electrical field, giving a change in the longitudinal resistivity $\Delta\rho_{\parallel}$. The ordinary MR (OMR) however is very small ($< 1\%$) at a moderate magnetic field except for some

semiconductors.

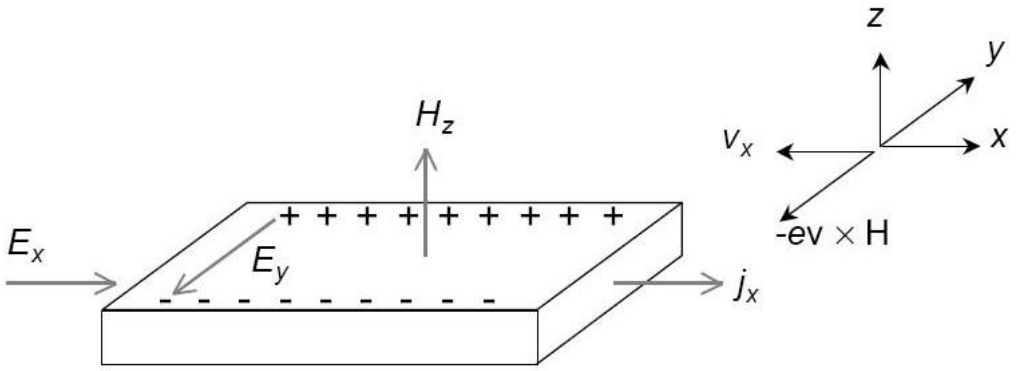

Figure 2.1: Schematic diagram of transverse magneto-resistance effect (Pippard, 1989).

2.1.1.2 Anisotropy Magneto-resistance

The electrical resistance of ferromagnetic metals or alloys under an external magnetic field is anisotropic and changes according to the relative orientation of the magnetization to the conduction current. The resistivity for the current parallel to the magnetic field increases with the magnitude of the field, and for the current perpendicular to the field, it decreases with the magnitude of the field. The physical origin of this anisotropy magneto-resistance (AMR) can be found in the asymmetric scattering cross section of the conduction electrons due to the spin-orbit coupling in the magnetic field as shown in Fig. (2.2).

The magnitude of AMR is typically a few percentage in low fields, e.g. AMR $\Delta R/R \approx 5\%$ at room temperature for Ni-Fe and Ni-Co alloys (McGuire and

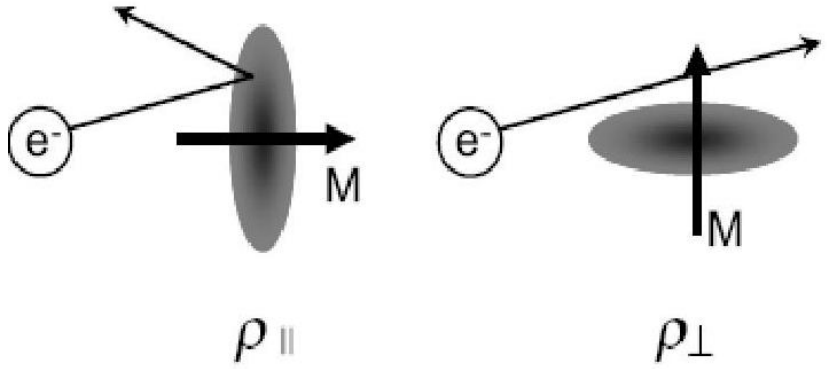

Figure 2.2: Asymmetric scattering cross-section of the conduction electrons (Parkin, 1994).

Potter, 2003). This moderate MR effect at low field finds application in magnetic read-heads commonly used in computer hard drives and other sensors. However they are now being replaced by spin valve and GMR multilayer sensors, which have larger sensing signals.

2.1.1.3 Giant Magneto-resistance

In 1988, Fert's group observed magneto-resistance changes as large as 50% at low temperatures in (001)Fe/(001)Cr multilayer structures (Baibich et al., 1988). The Fe layers were antiferromagnetically coupled across the Cr spacer layers, and the large change in the electrical resistance of the trilayer system was found to be due to the change in the relative orientation of the ferromagnetic layers from antiparallel to parallel alignment as the applied magnetic field was increased. In order to achieve a large resistance change it was necessary for the magnetization

of the Fe layers to be antiparallel in the absence of the external magnetic field (Baibich et al., 1988), and it was found that the interlayer coupling oscillated between ferromagnetic and antiferrromagnetic depending on the thickness of the Cr interlayer (Baibich et al., 1988). This GMR effect has since been observed for a variety of different transition metal/non-magnetic metal multilayers, including the Co/Cu system which displays GMR as large as 110% at room temperature for magnetic fields exceeding 20 kOe (Parkin, 1998). Magneto-resistance values of 50% - 60% are obtained in magnetic fields of several hundred Oersteds and values of 20% or more in fields of a few tens of Oersteds (Parkin, 1998). The resistance of the structure varies with the angle between the magnetization of adjacent magnetic layers as $\cos\theta$, and the change in resistance due to GMR effect can be described by

$$R(\theta) = R_P + \Delta R_{GMR}(1 - \cos\theta)/2 \tag{2.2}$$

The physical mechanism of GMR is extrinsic and it can be engineered, which is one of the reasons why there are such intense interests in optimizing the effect for applications. It is best described using a two current model which assumes that the conduction electrons are sub-divided into two spin sub-bands (Buttiker et al., 1985): those with spins parallel to the magnetization (majority) and those with spins antiparallel to the magnetization (minority). There is a dissimilar scattering rate for the two electron channels due to a difference in the available energy states

at the Fermi level. When the ferromagnetic layers are ferromagnetically coupled, the majority electrons have a low resistance channel through the entire structure, which leads to a lower resistance overall. When the ferromagnetic layers are antiferromagnetically coupled, both spin channels are equally scattered through the entire structure, leading to a higher resistance state. The GMR effect is shown schematically in Fig. (2.3).

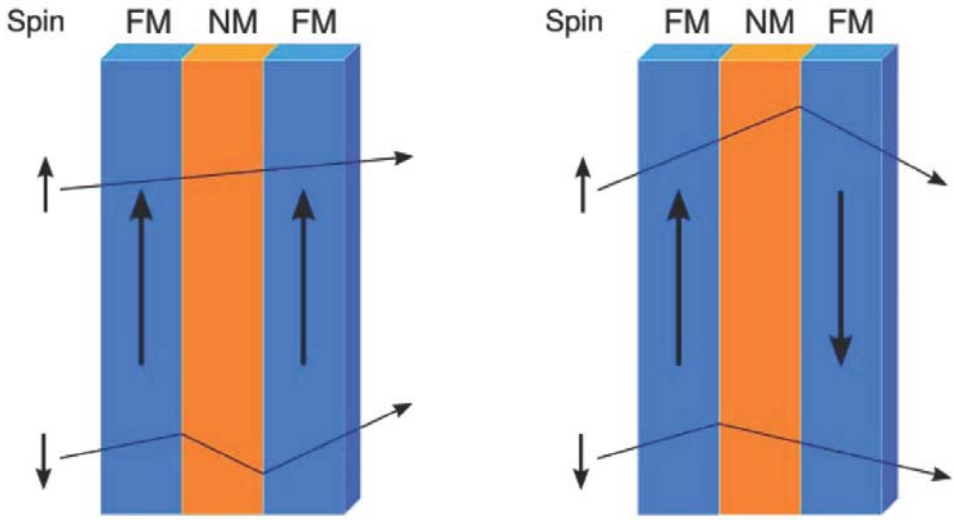

Figure 2.3: Schematic of conduction in multilayer magnetic film, showing how differential spin scattering rate produces a different resistance for parallel and antiparallel film magnetization (Hirota et al., 2002).

Since the initial discovery of GMR in magnetic/nonmagnetic multilayers, many alternative designs have been investigated to control the relative orientations of the ferromagnetic layers and to optimize the signal response and sensitivity. The GMR effect has been of great interest to the hard-disk drive industry

and IBM introduced the first GMR read-head sensor in 1997, within 10 years of its initial discovery. The major advantages over AMR are the improved signal response which enabled miniaturisation and therefore increased data storage density, and also the ability to engineer the response.

2.1.1.4 Colossal Magneto-resistance

A much larger magneto-resistance effect has been discovered in manganese based perovskite oxides, $Re_{1-x}Ae_xMnO_3$, where Re is a rare earth ion and Ae is a divalent alkaline (Nagaev, 2002). At first, von Helmolt observed an MR of 60% at room temperature in thin ferromagnetic films of $La_{2/3}Ba_{1/3}MnO_x$ on $SrTiO_3$ substrates (von Helmolt et al., 1993), and reported similar intrinsic MR effect in mixed valence $La-A-Mn$ oxide ($A = Ca, Sr, Ba$) in the following year (von Helmolt et al., 1994). In 1994, an MR effect in excess of a million percent at 77 K in $La_{0.67}Ca_{0.33}MnO_3$ thin film was discovered (Jin et al., 1994). This MR effect was called colossal magneto-resistance (CMR). Later, similar large MR effects were observed in other complex oxides such as layered perovskites, double perovskites Sr_2FeMoO_6 and pyrochlore $Tl_2Mn_2O_7$ (Kim et al., 1999; Imai et al., 2000). The CMR effect in the $Re_{1-x}Ae_xMnO_3$ is believed to arise from the close correlation between the magnetic phase transition and the electronic phase transition near the Curie temperature (T_C), e.g. double exchange and Jahn-Teller effect (Nagaev, 2002) as shown in Fig. (2.4), although the fundamental

physics is yet to be understood. Because the CMR devices usually require a large magnetic field, typically in the range of several Teslas near the Curie temperature T_C, the imminent technological application of the CMR effect is largely limited so far. CMR materials are known to possess a uniquely high spin-polarization of conduction electrons, and this has an important implication in the study of spin-polarized transport, e.g. spin-polarized tunneling (Nagaev, 2002).

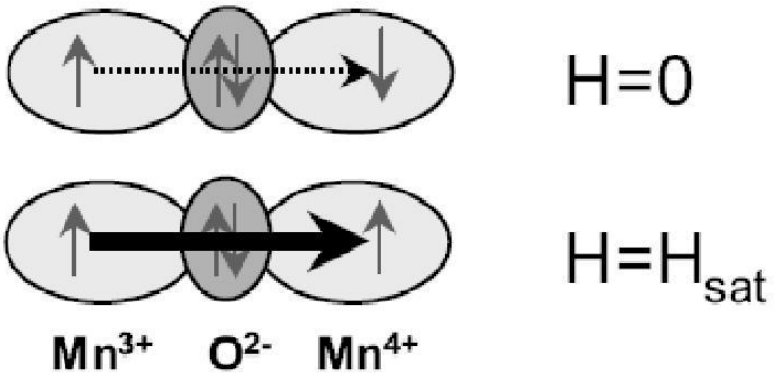

Figure 2.4: Schematic diagram of intrinsic double exchange and Jahn-Teller effect (Nagaev, 2002).

2.1.1.5 Tunneling Magneto-resistance

Tunneling magneto-resistance (TMR) exploits the quantum mechanical tunneling process between two ferromagnetic layers separated by an ultra thin insulating barrier, and the tunneling current between the two ferromagnetic layers depends on the relative angle between the magnetization in the two layers (Moodera et al., 1999; Mallinson, 2002).

This phenomenon was first observed in 1975 by M. Julliere in Fe/Ge/Co junctions, the experiment however was carried out at an extremely low temperature of 4.2 K (Julliere, 1975). Subsequently, Slonczewski showed theoretically that the tunneling electrical conductance varies as $\cos\theta$, where θ is the angle between magnetization in the adjacent ferromagnetic layers (Slonczewski, 1989). This TMR effect can be understood based on the two spin sub-channels model as for the GMR effect except that the metallic layer in the GMR devices is replaced by an insulating tunnel barrier. However, it is qualitatively different in that TMR is due to the conductance J_R for parallel magnetization is greater than the one for the antiparallel case because of the asymmetry of density of states (DOS) $\boldsymbol{D}$ of majority and minority sub-spin bands as presented in Fig. (2.5), while GMR occurs due to the spin scattering asymmetry through the entire structure (Mallinson, 2002). In principle, the magnitude of TMR is strongly dependent on the spin polarization of the conduction electrons, i.e. the spin asymmetry of the density of states (DOS) at the Fermi level (Mallinson, 2002). TMR ratios above 100% and as high as 500% have been achieved at room temperature in MgO based magneto-resistance tunneling junctions (MTJ) (Lee et al., 2007) as shown in Fig. (2.6).

Such advances in TMR investigation have already opened up a range of potential applications for nano-sized devices including nonvolatile tunneling junction

random access memories and MR sensors for high density magnetic storage (HD drives). However, problems related to the insulating barrier still need to be overcome, including reducing the junction resistance and improving the thermal stability (Mallinson, 2002; Petit et al., 2007). By sputtering a thin ferromagnetic layer on top of an antiferromagnetic layer, the orientation of the magnetization of this 'free' layer can be 'pinned' by the exchange coupling between the moment of the antiferromagnetic layer and the thin 'free' layer; then the thickness of this ferromagnetic 'free' layer must be thinner than the exchange length of the substance (Mallinson, 2002; Akerman, 2005). The magnetization of the other ferromagnetic layer can be easily switched by applying an external magnetic field if the film is made of 'soft' magnetic material. By this configuration, TMR changes sensitively depending on the external magnetic field, thus can be used as high sensitivity magneto-resistive devices such as magnetic random access memory (MRAM) (Petit et al., 2007; Akerman, 2005).

2.1.1.6 Ballistic Magneto-resistance

Even in controversy, ballistic magneto-resistance (BMR) is defined as "an effect that occurs in the conduction of spin-polarized electrons through highly constricted junctions in which the spin-flip mean free path is long compared with the magnetic domain-wall width" (Chung et al., 2002). For electrons passing through a nanocontact, the motion of these injection electrons is ballistic since

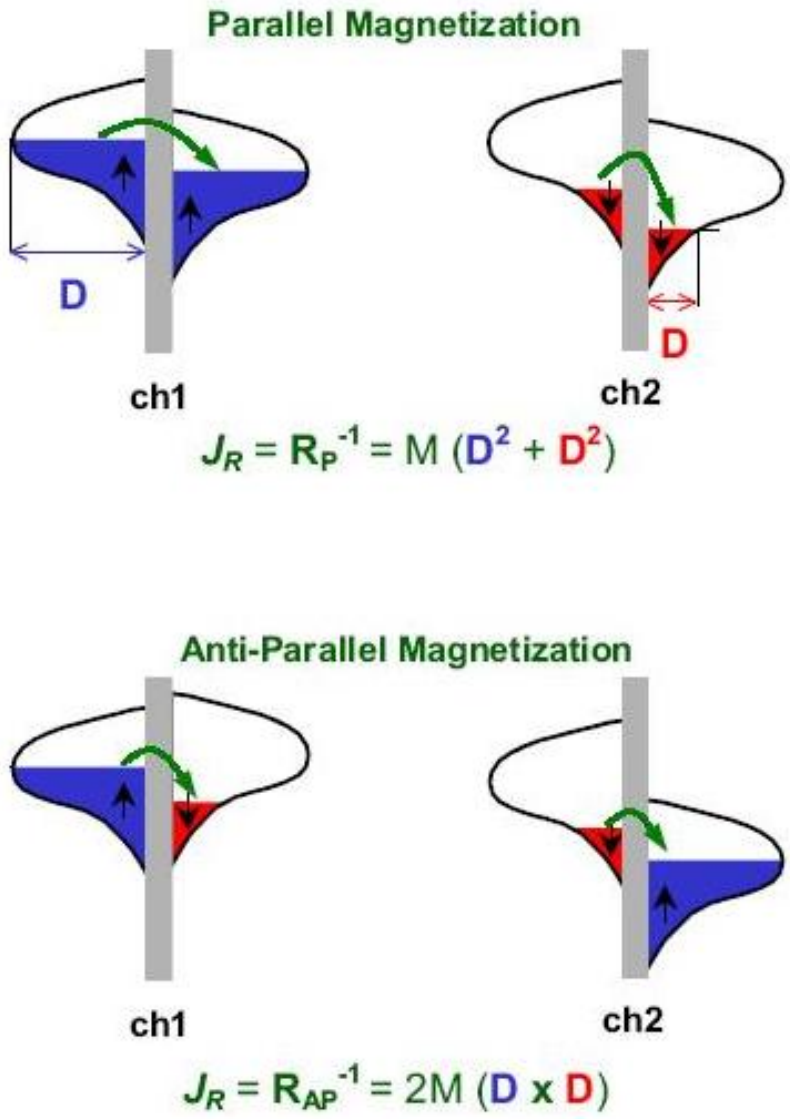

Figure 2.5: Conceptual representation of spin polarized tunneling. There is a differential tunneling conductance between asymmetric spin sub-bands. M stands for the matrix element for tunneling (Maekawa and Shinjo, 2002).

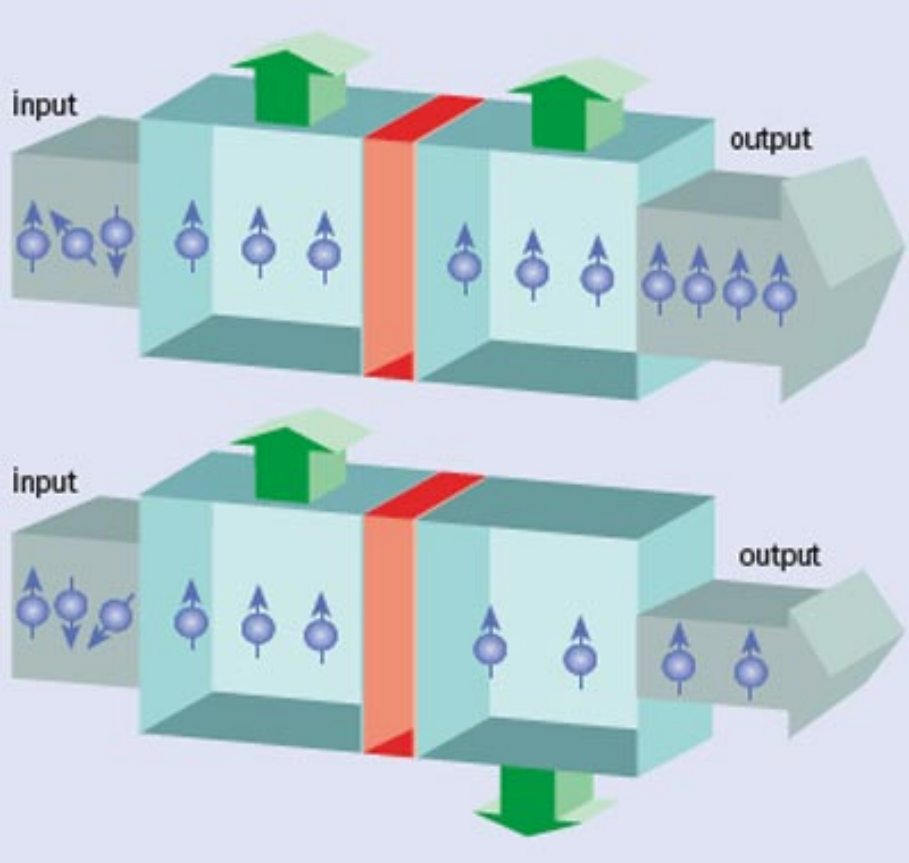

Figure 2.6: The magnetic tunnel junction (MTJ), which consists of two ferromagnetic layers separated by a tunneling barrier, exploits tunnel magneto-resistance to switch the output spin current between high and low. The first ferromagnetic layer acts as spin 'filter', while the second ferromagnetic layer acts as spin 'detector' (Bland et al., 2008).

the width of the constricted junction is usually less than the electron mean free path. When the magnetization across the nanocontact is in an opposite direction, the conduction electrons experience a huge scattering moment, which leads to a high resistance of the system. However, by applying an external magnetic field, the magnetization across the nanocontact can be switched to a parallel direction, then the resistance is relatively low (Brataas et al., 1999; Yang et al., 2004). Observed BMR ratio reaches a few hundred percent, much larger than reported GMR amplitudes (Yang et al., 2004; Brumfiel, 2003).

Systematical experiments have been carried out on BMR in various materials and large BMR ratio has been observed at room temperature and under low magnetic fields (Doudin and Viret, 2008). Garcia's group first observed BMR ratio up to 300% in simple Ni contacts made by mechanical methods and up to 700% in electrodeposited Ni nanocontacts (Garcia et al., 2001, 1999). In the following year, 540% BMR in mechanically formed Fe_3O_4 nanocontacts was subsequently observed (Verluijs et al., 2001). More recently, researchers reported over 3000% BMR (Chopra and Hua, 2002), and even 100,000% BMR (Hua and Chopra, 2003) at room temperature in electrodeposited Ni nanocontacts and mechanical pulled Ni wires respectively.

According to the existing theory, spin-ballistic transport through the nanocontact is the mechanism for BMR effect in different ferromagnetic systems, and it

is determined by the domain wall thickness only (Chung et al., 2002). However, several research groups are unable to reproduce the large BMR ratios in their experiments, and argued that the magnetism due to the reduced dimension of the contact is at the origin of the AMR effect (Brumfiel, 2003; Egelhoff et al., 2004).

2.1.2 Spin Transfer Torque

Spin-torque effect, predicted in 1996 by J. C. Slonczewski and L. Berger, refers to the torque exerted by a spin-polarized current on a ferromagnetic multilayer nano-sized structure (Slonczewski, 1996, 1999; Berger, 1996, 2001).

2.1.2.1 Spin-polarized Current

The basis of 'Spintronics' is the intrinsic spin of electrons and its associated magnetic moment in nano-sized devices. The electron is a negatively charged particle with intrinsic angular momentum (spin). This spin causes magnetic dipole effect, and makes every single electron act as a bar magnet (Chtchelkanova et al., 2003). For most materials, however, the spins of countless electrons within the body is randomly oriented such that their magnetic moments cancel out, and the material is nonmagnetic (see Fig. (2.7)). Only in magnetic materials, the electron spins will, on average, line up to produce a net magnetic field (see Fig. (2.8)).

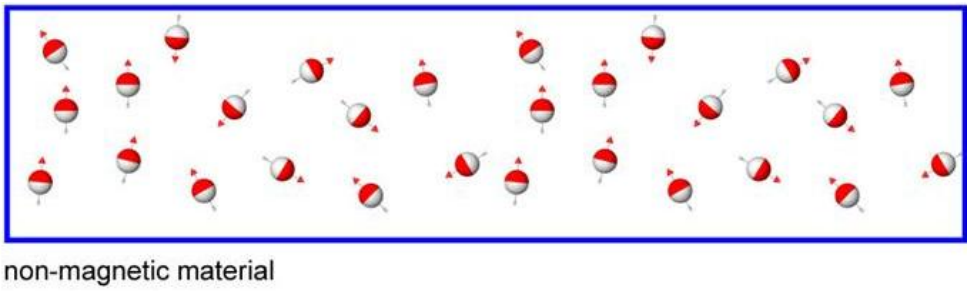

Figure 2.7: Non-magnetic material. The electron spins, represented by the arrows, are randomly oriented (TUNAMOS, 2008).

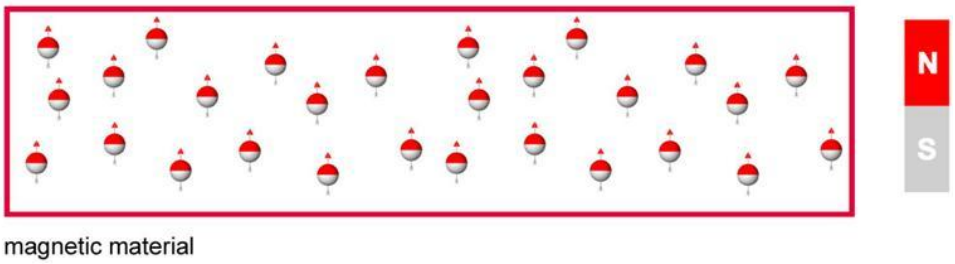

Figure 2.8: Magnetic material. The electron spins are added up to generate a net magnetic field (TUNAMOS, 2008).

For practical applications of Spintronics based on spin-polarized transport in solid-state devices, it is necessary to generate electric currents that have a net spin moment. Several methods for the creation of this spin-polarized current have been proposed, and the most convenient way is by injecting a electron current through the interface between a magnetic material and a nonmagnetic substance (Fiederling et al., 1999; Gurzhi et al., 2003). Passing through the magnetic material, the electron current will become spin-polarized. Subsequently, this spin-polarized current will be injected into the nonmagnetic material, retaining its spin polarization direction as in the magnetic material (see Fig. (2.9)) (Fiederling et al., 1999). The distance over which a considerable concentration of spin-polarization is retained is of the order of the spin relaxation length λ, which varies from 10 nm - 10 mm (TUNAMOS, 2008).

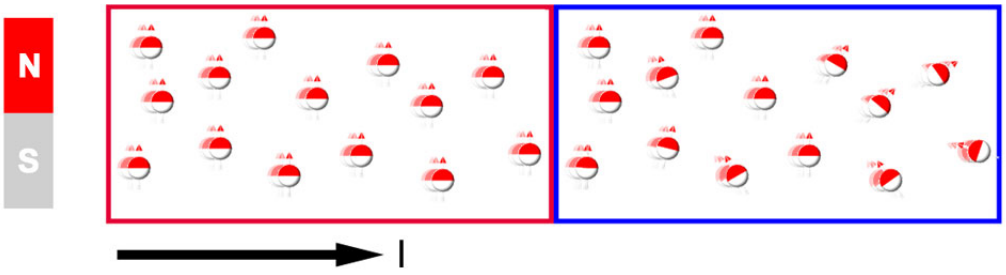

Figure 2.9: When an electron current is injected from a magnetic (left) to a nonmagnetic (right), its spin-polarization will be retained over a certain distance (TUNAMOS, 2008).

2.1.2.2 Spin-momentum Transfer

Spin-transfer torque is the torque exerted by a spin-polarized current on a magnetic layer. The conduction electrons passing through a magnetic material of fixed magnetization are spin polarized, with their spin aligned in the same direction as the magnetic layer even after they leave the magnetic layer. When this spin-polarized current is injected into a second magnetic layer and if the spin of the incident electrons and the magnetization of the second magnetic layer are not parallel, this magnetic layer will experience a torque resulting from the rotation of the electron spins (Ralph and Stiles, 2008). This process is illustrated schematically in Fig. (2.10).

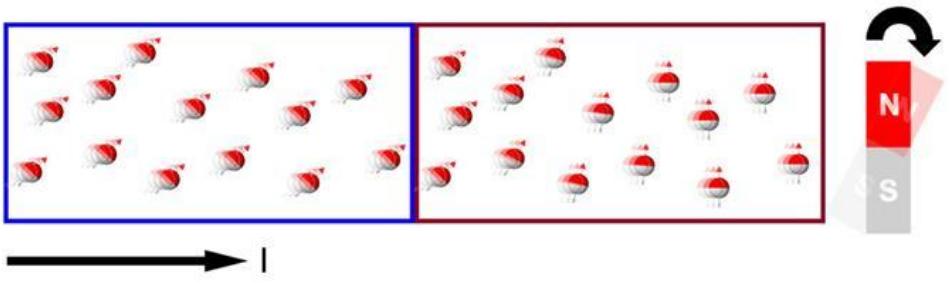

Figure 2.10: A spin-polarized electron current is injected into a magnetic layer (right). The spins of the incident electrons are quickly absorbed by the magnetic layer (TUNAMOS, 2008).

Depending on the magnitude of the current density and the properties of the system structure, this spin-polarized current can transfer enough spin angular momentum to cause either the switching of the magnetization direction in

the magnetic layer (current-induced switching) which is of great interest for application in MRAM, or the stable precession of the magnetization (spin-torque oscillator) which is the topic of this thesis (Ralph and Stiles, 2008).

2.1.3 Device Configuration

Trilayer system structures used for spin-torque oscillators typically consist of a relatively thick 'fixed' ferromagnetic layer (whose magnetization is static and determines the direction of the spin-polarization of the incident electrons), a spacer, and a relatively thin ferromagnetic 'free' layer (whose magnetization will experience precessional oscillation due to the spin-transfer-torque effect). The nonmagnetic spacer can be either metal (e.g. copper) or dielectric material (e.g. MgO). When the spacer is made of metal, the multilayer structure is generally called a giant magneto-resistance (GMR) spin valve, while in the second case it is referred to as a magnetic tunneling junction (MTJ) and its performance is based on the tunneling magneto-resistance effect (TMR).

There are two most common multilayer geometries for STO: magnetic nano-pillar and magnetic nano-contact (see Fig. (2.11)). For the nano-pillar structure, the 'free' ferromagnetic layer has finite lateral size, and the spin-polarized current can be considered as spatially nonuniform. Similarly, for a nano-contact, the 'free' ferromagnetic layer is not bounded in the plane, and the oscillations excited by

the spin-polarized current can excite propagating microwave signals within the 'free' layer.

However, in both the geometries described above, the cross-sections of the spin-polarized current must be nano-sized in order to produce an extremely high current densities ($10^7 - 10^8 \mathrm{A/cm^2}$), which is necessary to show a clear manifestation of the spin-transfer torque effect and sustain the microwave precessional oscillation (Ralph and Stiles, 2008).

2.2 Literature Review

Experimental evidence for the effects of spin-transfer torque comes from changes in the differential resistance of the trilayer system. For switching between parallel and antiparallel alignment, there is a discrete change in the differential resistance that would be expected from the GMR or TMR effect. For large applied magnetic fields, a peak in differential resistance at a certain critical current has been interpreted as an evidence for excitation of spin waves (Tsoi et al., 1998). Tsoi et al. first reported this differential resistance peaks in Co/Cu multilayers by current injection through a mechanical point contact (Tsoi et al., 1998).

However, the first direct measurements of current-induced microwave magnetization precession were made with a spin valve structure (Kiselev et al., 2003). In the experiment, the samples were made by sputtering a multilayer of com-

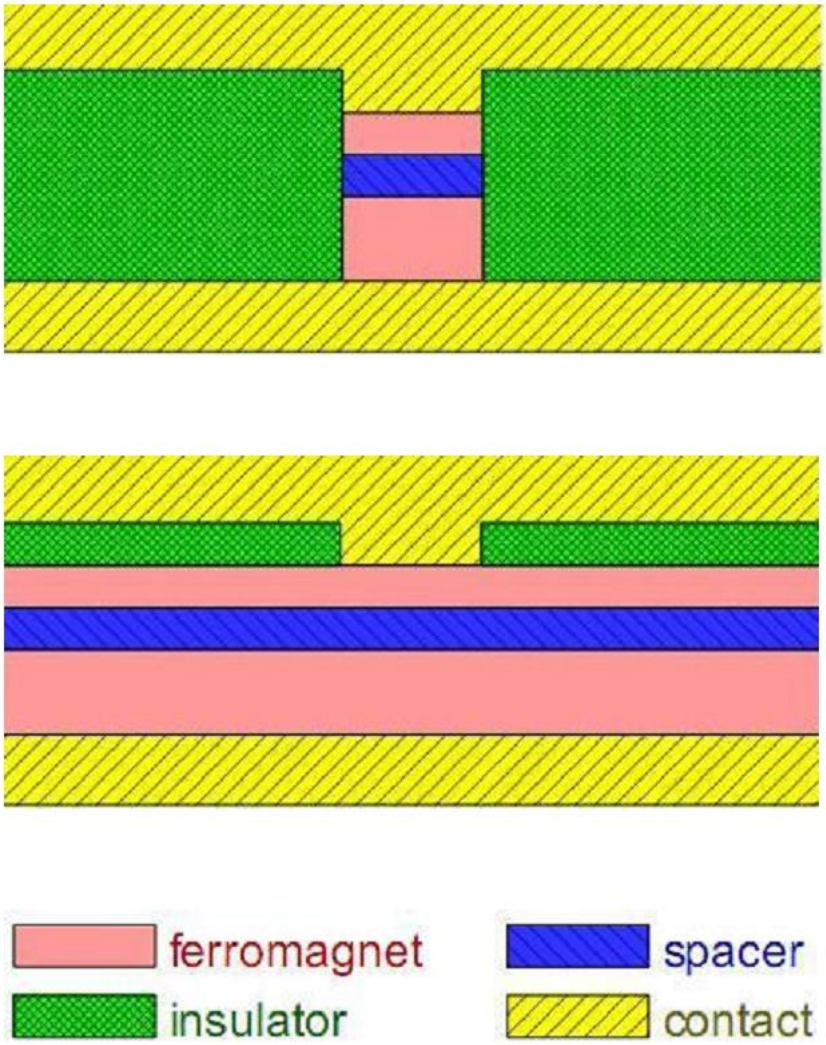

Figure 2.11: Nano-pillar (Top) and Nano-contact (Bottom) geometries. The thinner ferromagnetic layer is the 'free' layer and the thicker ferromagnetic layer is the 'fixed' layer. The spacer could be either metal or dielectric material (Ralph and Stiles, 2008).

position 80 nm Cu/40 nm Co/10 nm Cu/3 nm Co/2 nm Cu/30 nm Pt onto an oxidized silicon substrate and then milling through part of the multilayer to form a pillar with elliptical cross-section of lithographic dimensions 130 nm × 70 nm. Top contact was made with a Cu electrode (Kiselev et al., 2003). Transmission or reflection of electrons from the thicker 'fixed' Co layer produces a spin-polarized current that can generate a torque in the thinner 'free' Co layer. Subsequent oscillations of the 'free' layer magnetization relative to the 'fixed' layer change the device resistance to produce a time varying voltage signal, and different preamplifiers and mixers (see Fig. (2.12)) allow measurements over 0.5–18 GHz or 18–24 GHz.

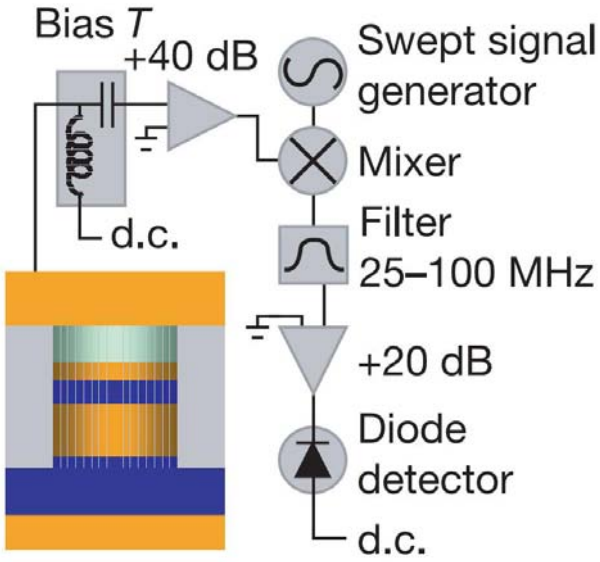

Figure 2.12: Schematic of the sample with Cu/Co multilayers together with heterodyne mixer circuit (Kiselev et al., 2003).

The variations in the generated spectra of magnetic excitations were studied as functions of the magnitude and direction of the external magnetic field (see Fig. (2.13)) and the bias current (see Fig. (2.14)). Fig. (2.13) shows the magnetic field dependence of the small-amplitude signal at $I = 3.6$ mA, from which a systematic frequency shift can be observed. Fig. (2.14) gives the microwave spectra at $H = 2.0$ kOe for current values from 1.7 to 3.0 mA, showing the evolution of the small-amplitude precessional peak (Kiselev et al., 2003).

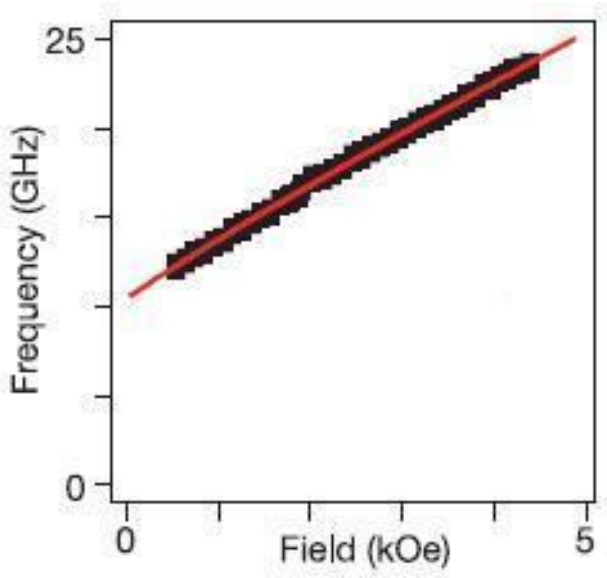

Figure 2.13: Magnetic field dependence of the small amplitude signal frequency at $I = 3.6$ mA (Kiselev et al., 2003).

At the same time, investigations of the current-induced spin wave excitations in nano-structures with a single magnetic layer were also conducted (Ji et al., 2003). In the experiment, a nano-contact geometry was adopted (see Fig. (2.15)).

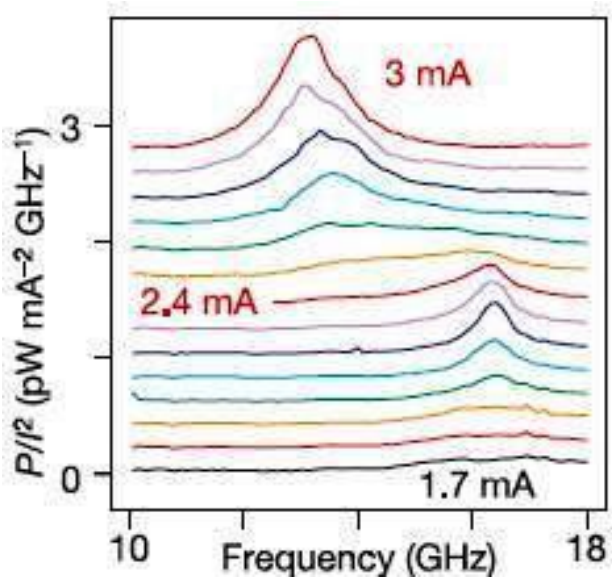

Figure 2.14: Microwave spectra at $H = 2.0$ kOe, for currents from 1.7 to 3.0 mA (Kiselev et al., 2003).

For the sake of simplicity, the author applied the trilayer structure model to the single film geometry. The current spreads out immediately after the injection into the Co film and the current density decreases rapidly due to the expanding geometry; under a certain depth, which is marked by a dashed line in Fig. (2.15), the current density is so low that it can not affect the magnetization of the material (Ji et al., 2003). All the spin moments below the dashed line are aligned in the direction of the external magnetic field. In analogy with the multilayer configuration, the region below acts as a 'fixed' layer in the configuration. The region above the boundary and under the point contact, where the current density is sufficiently high, acts as the 'free' layer (Ji et al., 2003). In this kind of

interpretation, the single Co film is separated into a 'free' layer below the point contact and a 'fixed' layer for the remainder of the Co film.

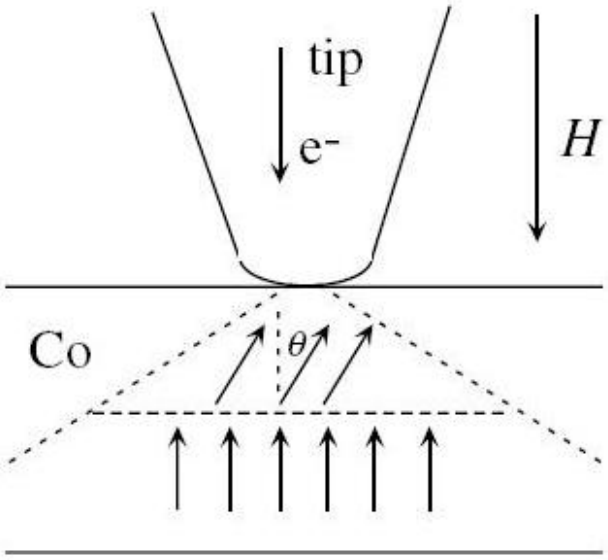

Figure 2.15: A microscopic picture of a point contact between a tip and single layer Co film (Ji et al., 2003).

Obviously, the physics of the spin-transfer torque effect in a single magnetic layer differs from that in a multilayer system, and the theoretical explanation of this effect was given by H. Xi (Xi et al., 2007).

In the meantime, a new form of current induced ferromagnetic resonance (FMR) that uses innovative methods (see Fig. (2.16)) has been developed to both drive and detect magnetic precession (Sankey et al., 2006a), and it has been demonstrated that spin-transfer-driven FMR measurements provide detailed information about the linear spin wave excitation modes.

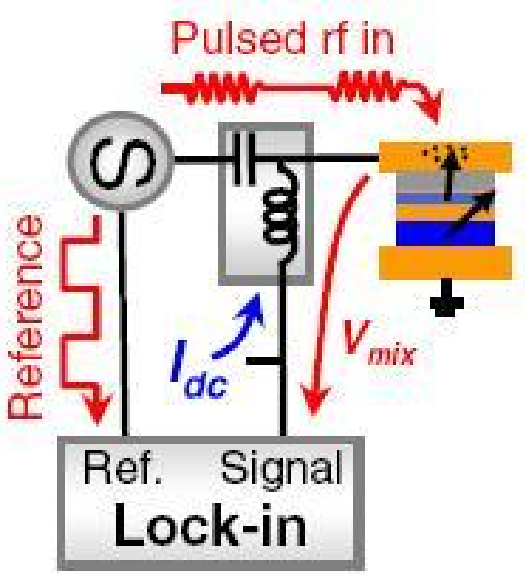

Figure 2.16: Schematic of circuit used for FMR measurements (Sankey et al., 2006a).

In the case when the 'free' layer of an STO is not magnetized by the external magnetic field and the anisotropy of this layer is not sufficient to create a spatially uniform ground state, the static magnetization of the 'free' layer could be in a vortex ground state, and it has been experimentally demonstrated in Py/Cu/Py nano-pillar structure that spin-polarized current can exert gyrotropic oscillations of such a vortex (Pribiag et al., 2007). The spin-torque driven vortex oscillations, which can be obtained in essentially zero magnetic field, exhibit linewidths that can be much narrower than 300 kHz at around 1.1 GHz, which is significantly narrower than that of spin-transfer-torque oscillations in magnetic spatially uniform spin valves (usually varies between 50 to 500 MHz) (Pribiag et al., 2007). The

author argues that the relevant vortex oscillation volume is the entire thick layer (Fig. (2.17)). The larger volume reduces the amplitude of the random Langevin magnetic field associated with the thermal fluctuation (Pribiag et al., 2007).

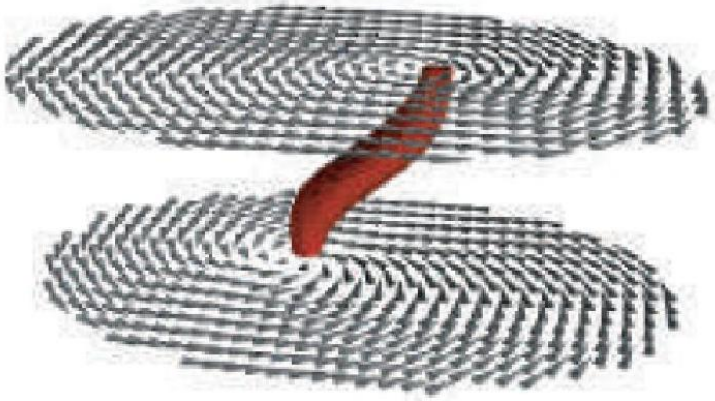

Figure 2.17: Magnetic configuration of the ferromagnetic layers, showing the in-plane components of the layer's upper and lower surfaces and the vortex core (Pribiag et al., 2007).

The forced dynamics of the GMR STOs under the influence of an external periodic signal of a relatively low frequency was studied experimentally in nano-contact geometry (Pufall et al., 2005). Point contacts are made on continuous thin multilayered film (5 nm NiFe/5 nm Cu/20nm CoFe). To examine the effects of an *ac* current on the resonance, an additional 40 MHz low frequency (compared to the *dc* generated microwave frequencies at the range of 9.5–10.1 GHz) *ac* current was applied together with the fixed bias *dc* current (Pufall et al., 2005). In Fig. (2.18), the spectral outputs are shown for several input *ac* current amplitudes ΔI. The additional *ac* current generates the frequency modulation effect, and

with increasing modulation current amplitude ΔI, more power is driven into sidebands positioned at $f = f_0 \pm n \cdot 40$ MHz, where n is the sideband order, and f_0 stands for the center frequency (Pufall et al., 2005). Also, the center frequency decreases significantly with ΔI. The simulation results reveal that these observed Frequency Modulation effects are not simply electrical (e.g., the results of signal mixing due to the nonlinear $I - V$ phase relation), but rather correspond to periodic variations in the orbit trajectory of the magnetization of the free layer of the nanocontact structure (Pufall et al., 2005).

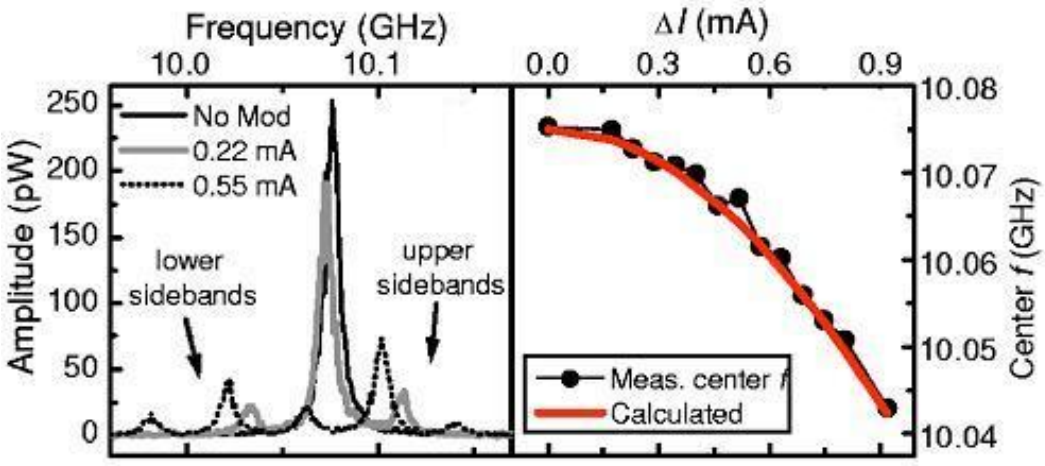

Figure 2.18: Spectral output of the STO for several different input modulation amplitudes ΔI, showing side band changes, and shift of center frequency vs ΔI (Pufall et al., 2005).

Also, the phase locking of an STO to an injected *ac* signal was directly measured (Rippard et al., 2005). An *ac* current, having frequency that is quite close to the STO's generation frequencies, was applied with the fixed *dc* biased current.

The dependence of the oscillation frequency on *dc* current for several different *ac* injection amplitudes is shown in Fig. (2.19). The STO locks to signals up to several hundred MHz away from its natural oscillation frequency (Rippard et al., 2005). This is not a frequency modulation effect, since in the modulation schemes the frequencies of the mixed signal are independent of the amplitude of the modulation signal. And the time-domain measurements of the microwave output has indicated that the oscillation has been phase 'pushed' or 'pulled' towards the injected *ac* signal (Rippard et al., 2005).

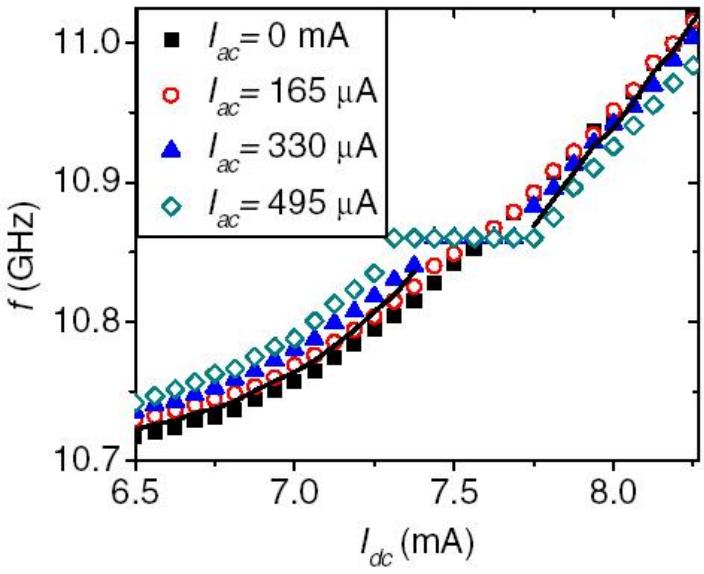

Figure 2.19: f as a function of I_{dc} for several different amplitudes of drive at 10.86 GHz (Rippard et al., 2005).

Subsequently, the mutual phase-locking in a pair of STOs was experimentally observed (Kaka et al., 2005; Pufall et al., 2006; Mancoff et al., 2005). The two

'independently' connected contacts A and B are separated by a distance r on the same substrate; the geometry of the device is shown in Fig. (2.20). In the first experiment (Kaka et al., 2005), the contact separation $r = 500$ nm, and the contacts are separately current biased, making each contact an 'independently' controlled STO. When the frequency of one STO is made to approach the other, interactions cause the oscillators to lock together. Fig. (2.21) plots the evolution of the combined spectrum from both STOs as current I_A through contact A is fixed while I_B increases. As I_B reaches 9.0 mA, f_A unites with f_B until I_B exceeds about 11 mA, these data show that both STOs frequency-lock over a 1.5 mA range in I_B (Kaka et al., 2005). When the phase shift between the two contacts is set to maximize the output power, the combined power in the phase-locked state is the coherent sum of the individual power of each oscillator (Kaka et al., 2005).

In contrast, another group (Mancoff et al., 2005) adopted a similar geometry but with relatively smaller separation distance ($r = 120$ nm) between the two contacts, and a total *dc* current was applied to the pair. In other words, the two nanocontact STOs were connected in parallel in the equivalent circuit. Only one oscillation is observed, and the closely spaced pairs are phase-locked with zero phase shift (Mancoff et al., 2005). The output power from these contact pairs with small spacing is approximately twice the total power from two contacts that undergo separate oscillations (Mancoff et al., 2005).

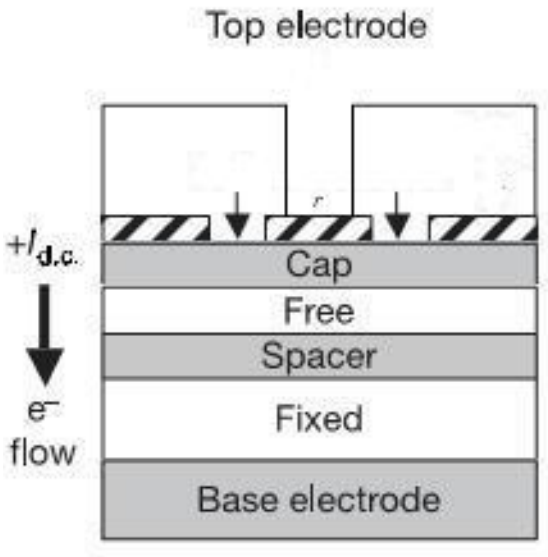

Figure 2.20: Schematic cross-section of two nano-contacts to a GMR based spin valve. Positive *dc* current flow is defined as electrons flowing from the 'free' to the 'fixed' layer (Kaka et al., 2005).

This mutual phase-locking may provide a potential means for frequency mixing, phase control, and coherent power by combining arrays of nanoscale microwave oscillators (Pufall et al., 2006).

Since the microwave power generated by STO is comparable to the noise power in the magnetic material of the 'free' layer at room temperature, it is very important to study the influence of the thermal noise on the performance of the STOs (Smith et al., 2006). Detailed measurement has been conducted to investigate the dependence of the oscillation frequencies, linewidths, and output powers of spin-transfer nano-contact oscillators as functions of applied magnetic field strength, bias current, and angle of the applied magnetic field at different

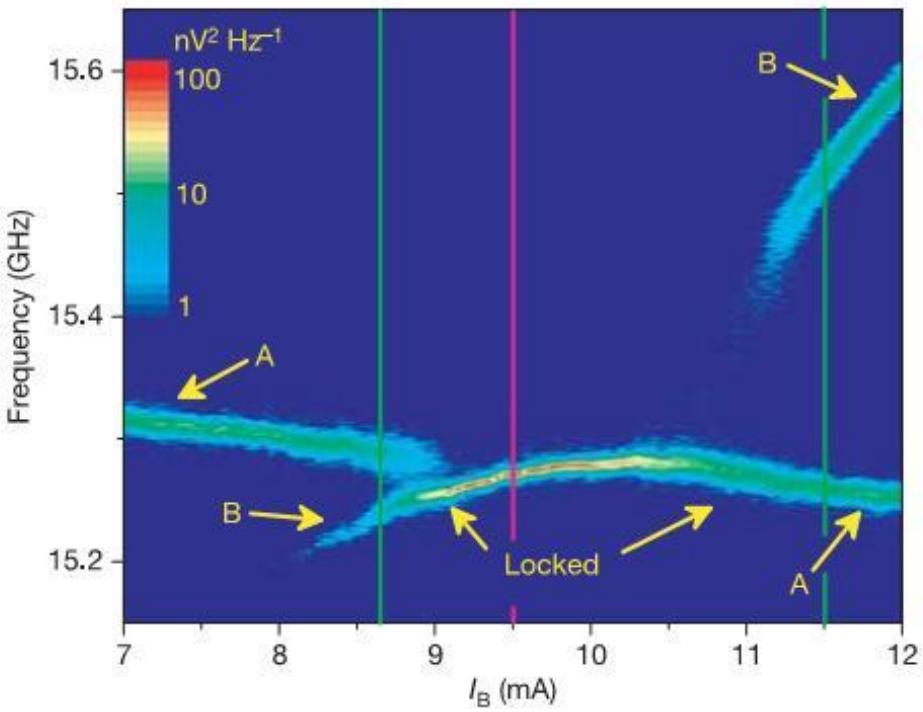

Figure 2.21: Combined spectrum from both STOs as current through one contact is ramped from 7 mA to 12 mA, while current through the other contact is fixed at 8 mA (Kaka et al., 2005).

temperatures (Sankey et al., 2005; Mistral et al., 2006; Rippard et al., 2006). With increasing temperature, the FWHM is expected to increase (Fig. (2.22)) and the oscillation frequency will decrease (Fig. (2.23)). Similar trends have been obtained under different experimental conditions with different geometries of STOs.

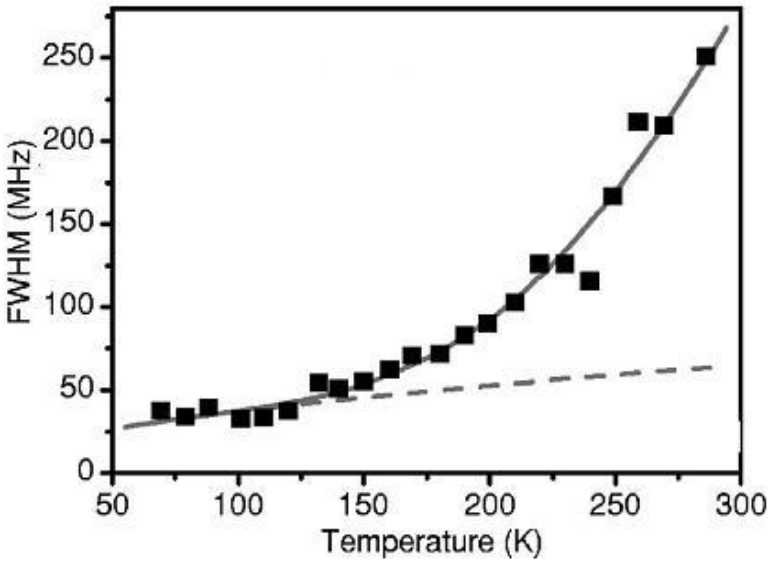

Figure 2.22: Measured linewidths as a function of temperature (Sankey et al., 2005).

Magnetic tunneling junctions (MTJs) with a thin dielectric spacer (e.g. MgO) between the magnetic layers have a much larger tunneling magneto-resistance (TMR) than fully metallic GMR spin valves, and it has been reported that MgO based MTJs can generate output powers in the μW range, which is compatible with applications for wireless telecommunications. (Deac et al., 2008). Therefore,

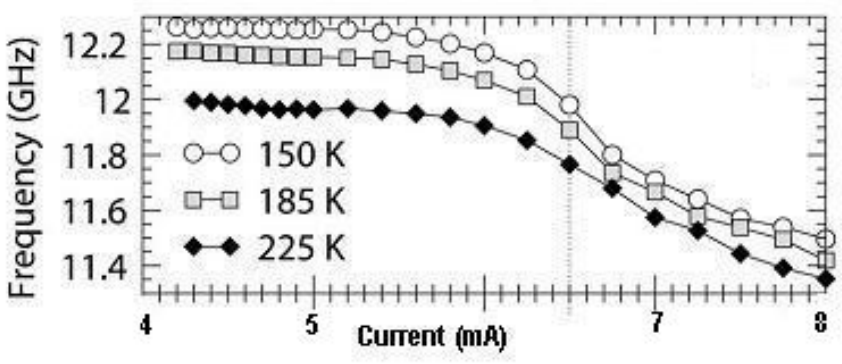

Figure 2.23: Oscillation frequencies as a function of applied current under different temperatures (Mistral et al., 2006).

MTJs are very promising for the development of practical STO devices.

The theoretical description of the dynamics of the microwave excitation by spin-polarized current was developed using many different techniques. Magnetization dynamics is most widely investigated using the macrospin model (Xiao and Zangwill, 2005). The macrospin approximation assumes that the magnetization of a sample stays spatially uniform throughout its motion and can be treated as a single macroscopic spin as it is shown in Fig. (2.24) (Ralph and Stiles, 2008). Since the spatial variation of the magnetization is neglected, exploring the dynamics of magnetic systems is much more tractable using the macrospin approximation than it is using full micromagnetic simulations (Berkov and Miltat, 2008). The macrospin model makes it easy to explore the phase space of different torque models, and it has been a very useful tool for gaining a zeroth-order understanding of spin-torque physics (Xiao and Zangwill, 2005).

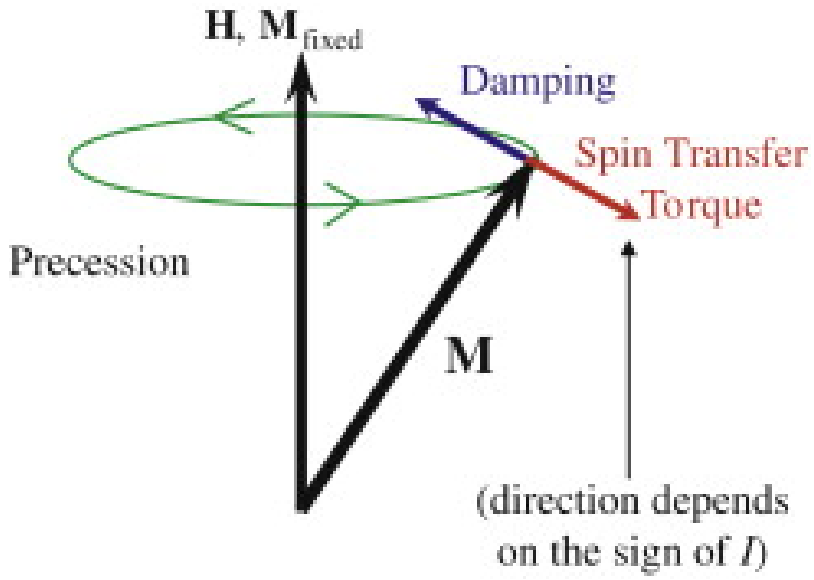

Figure 2.24: Directions of damping and spin-torque vectors for macrospin model (Ralph and Stiles, 2008).

For the practical application of STO, it is important to understand how these nano-sized oscillators will behave under the influence of external periodic signals or different kinds of fluctuations. A simulation with a sweeping *dc* noiseless current at 0 K under different magnetic fields shows the frequency of oscillation of the device as a function of current (see Fig. (2.25)) (Persson et al., 2007).

The noise in the *dc* current is simulated as an additive white noise, i.e. following a Gaussian normal distribution (Iacocca, 2008). The magnitude of the noise is proportional to the *dc* current and an input factor given as a percentage. So the added term in the current is:

$$I_{dc}\xi X \tag{2.3}$$

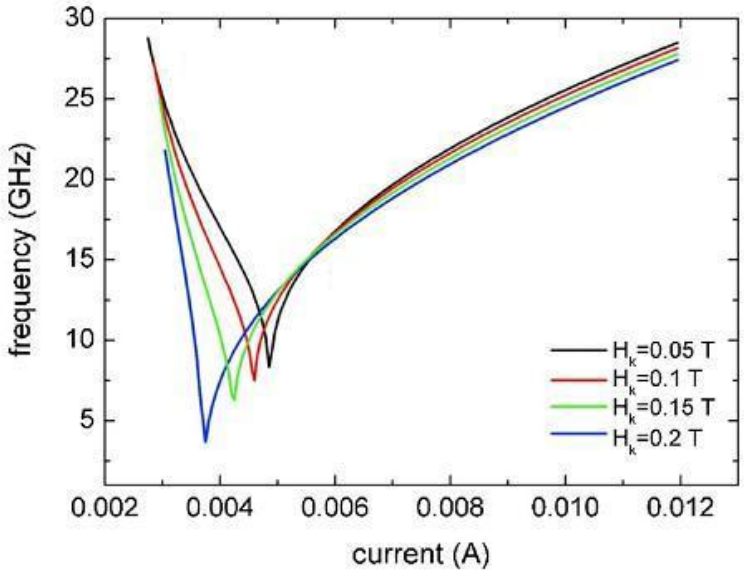

Figure 2.25: Oscillation frequency of STO as a function of applied *dc* current at 0 K for different H_k (Persson et al., 2007).

where X varies from 0 to 1, and ξ is a Gaussian distributed random number calculated using the Box-Muller algorithm, which is based on a uniformly distributed random number.

The simulation was conducted at 0 K, *dc* current of 11 mA and noise levels between 0 and 100%. The main parameters of the STO device have been kept constant during the simulations. In the calculation, the noise was increased in steps of 10%. At 30% of noise it was very difficult to fit with a Lorentzian or a Gaussian profile (Iacocca, 2008). A similar situation was found in higher noise levels and thus it suggested that a 'mixture' between both profiles should be adopted. To reflect this fact, the Voigt profile is adopted. With a Voigt profile,

the fit is possible as can be seen in Fig. (2.26). The STO data points are not shown smoothed, but the fitting was done after the smoothing. Also, the 3 curves shown below have the same half width at half-maximum (HWHM), and the Voigt function is fitted by changing the weight parameter (Iacocca, 2008).

From the fits, one can obtain the HWHM and frequency of oscillation and the quality factor Q can be determined for each noise level (see Fig. (2.27)).

It is important to note that even with *ac* noise, the STO can still oscillate at the same frequency with high Q factors.

Recently, numerical work has demonstrated that there exists an unexpected intrinsic phase shift between the spin-torque oscillator and the applied alternating current I_{ac} injected at the intrinsic frequency f_{STO} of the STO (Zhou et al., 2007).

A typical simulation illustrating the existence of an intrinsic phase shift between the STO resistance R_{STO} and the external drive signal I_{ac} is shown in Fig. (2.28). Before the alternating current is turned on, the STO is allowed to settle into a steady-state precession for about 24 ns. When the alternating current is turned on, the STO immediately starts adjusting its precession (Zhou et al., 2007). Note that the positive phase shift is defined when the resistance voltage lags the current.

Fig. (2.29) shows the temporal evolution of the relative phase shift $\Delta\varphi$. From Fig. (2.29) and Fig. (2.30), we can see that $\Delta\varphi$ gradually transits to the same

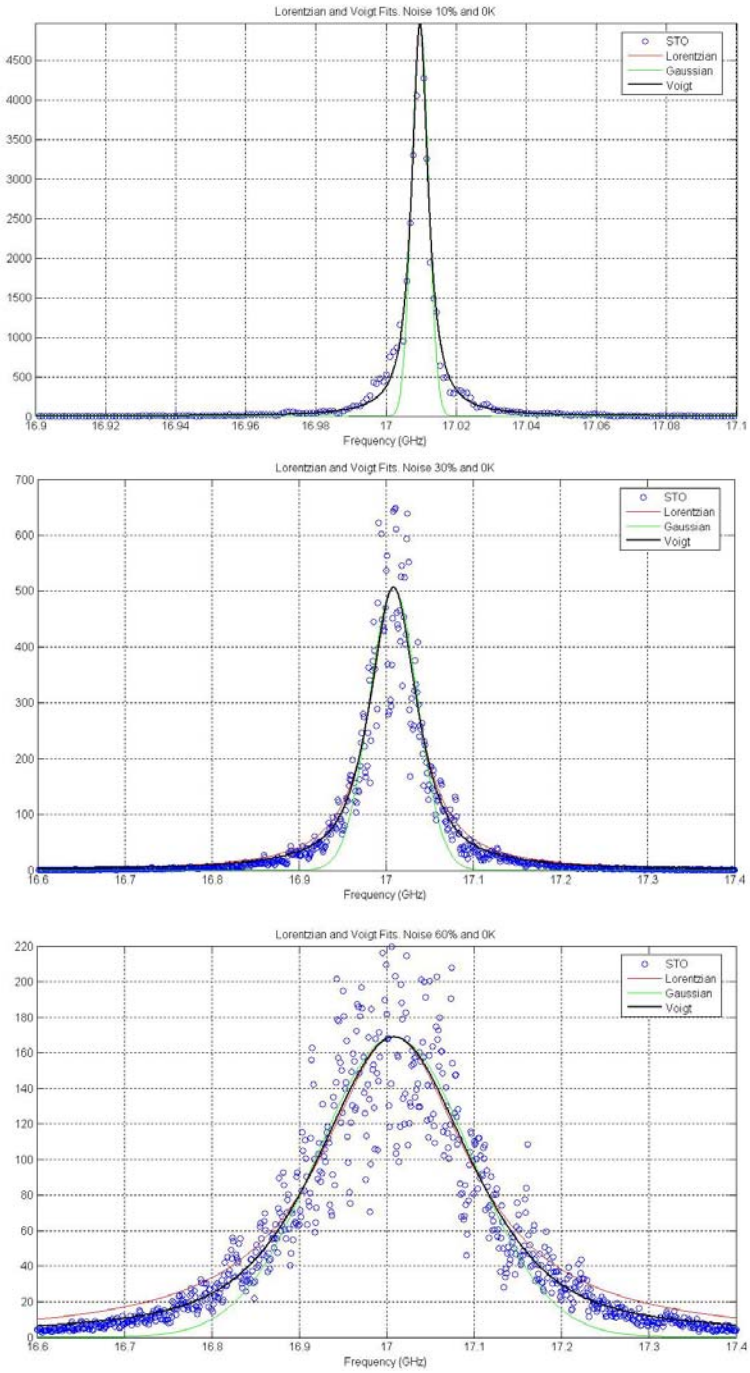

Figure 2.26: Output microwave spectra of oscillations with different noise levels (Iacocca, 2008).

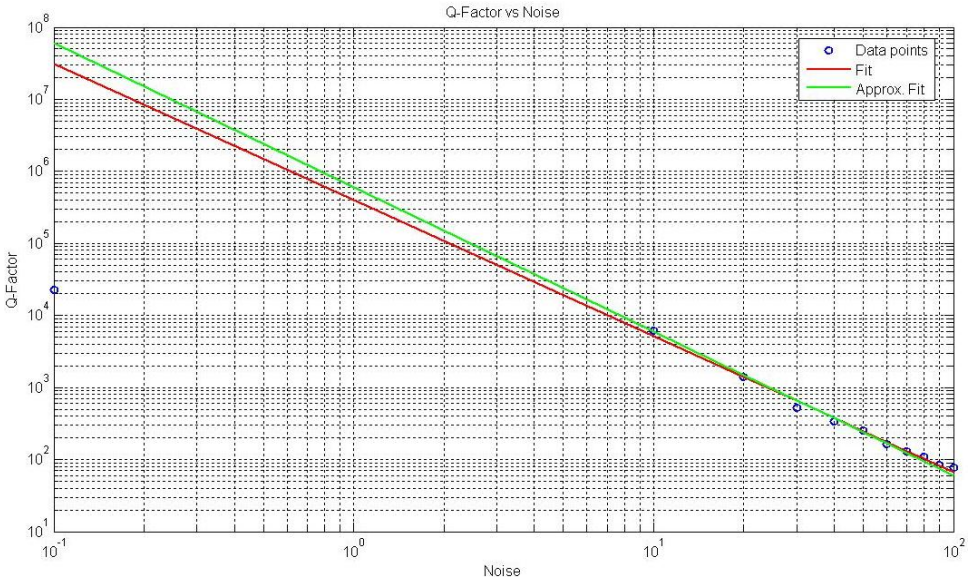

Figure 2.27: Fitted quality factor as a function of *ac* noise (Iacocca, 2008).

steady state value $\Delta\varphi_0$, regardless of the initial values (Zhou et al., 2007).

Depending on the *ac* current amplitude, the system can be under-damped, critically-damped, and over-damped as shown in Fig. (2.31) (Zhou et al., 2007). For larger *ac* driving current, the system undergoes an under-damped ringing transition before it finally reaches the steady state. The ringing behavior is expected to significantly affect the robustness of locking states of two serially connected STOs (Zhou et al., 2007).

This phase shift can furthermore be utilized to improve the synchronization robustness of serially coupled STOs (Zhou et al., 2007).

The synchronization states of N STOs connected in series are also numerically studied (Grollier et al., 2006). More specifically, for STOs connected in series as

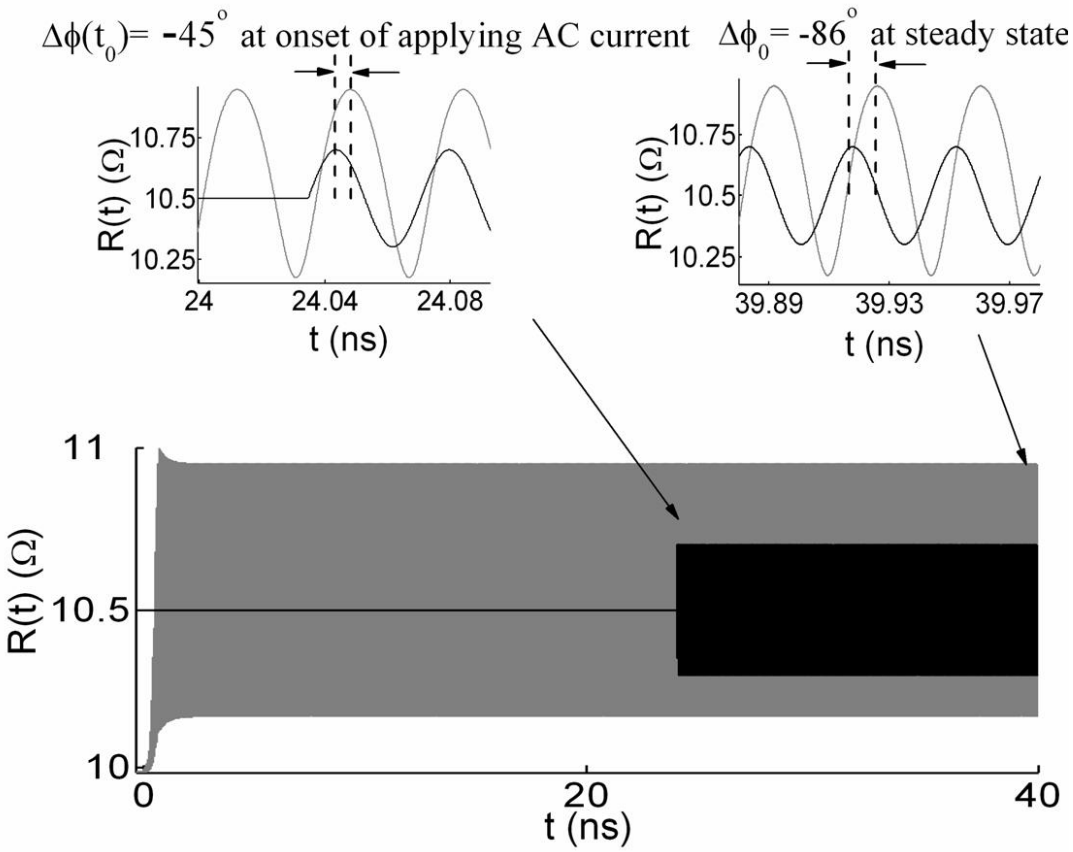

Figure 2.28: A typical simulation result. Bottom figure shows the entire simulation run of 40 ns. Upper left figure shows the STO resistance and I_{ac} as a function of time with an initial phase shift of $-45°$. Upper right figure shows the preferred intrinsic phase shift of $-86°$ after the STO has accommodated its precession to I_{ac} (Zhou et al., 2007).

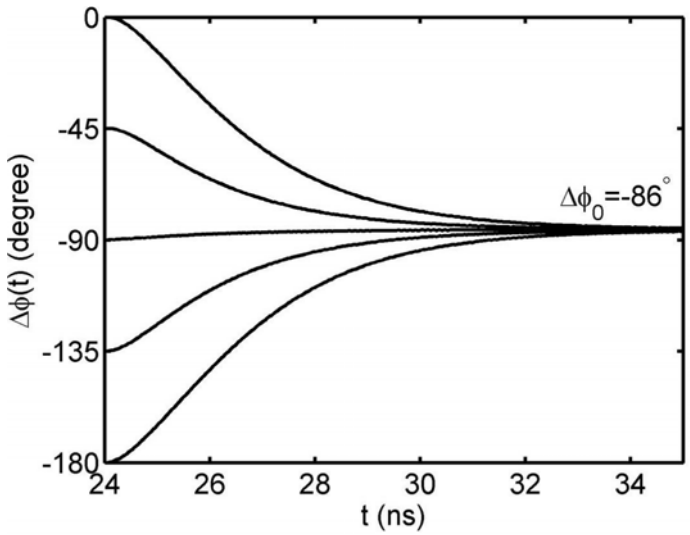

Figure 2.29: The temporal evolution of relative phase shift between the *ac* current and the STO for different initial phase shift (Zhou et al., 2007).

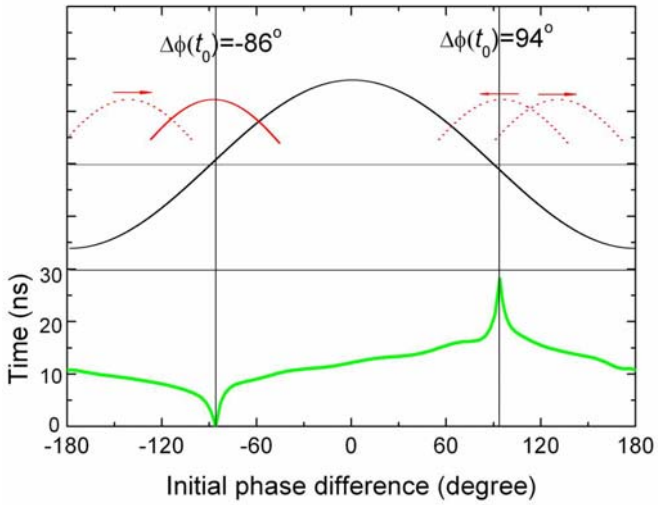

Figure 2.30: Time to reach steady state as a function of initial phase differences (Zhou et al., 2007).

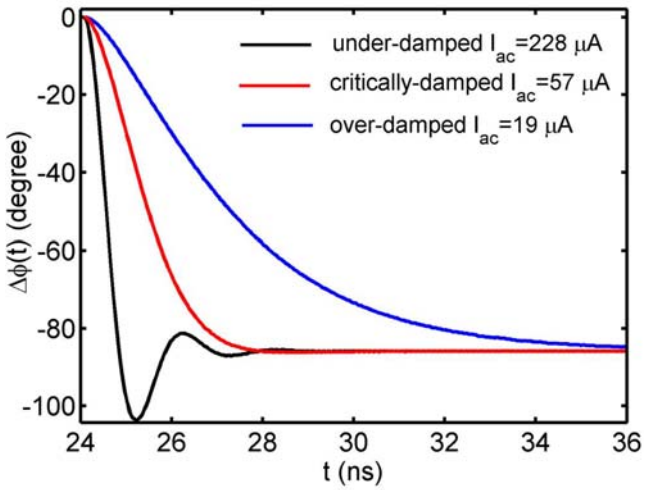

Figure 2.31: The under-damped, critically-damped and over-damped curves of the relative phase shift (Zhou et al., 2007).

shown in Fig. (2.32), the coupling due to the microwave current induced in each oscillator by the oscillations of all others are counted in the calculation with different coupling factors A_{GMR} (Grollier et al., 2006). Fig. (2.33) shows the emitted power by the set of 10 oscillators as a function of the frequency for different coupling parameters A_{GMR}. When $A_{GMR} = 0$, for which the coupling effect is neglected, each oscillator oscillates at its own frequency, and the total emitted power is that emitted by the sum of independent oscillators. For $A_{GMR} =$ 0.03 and 0.05, all the oscillations result in a single peak; in these two cases, there is an increase by a factor of about 100 in the integrated emitted power with respect to the case without coupling ($A_{GMR} = 0$) (Grollier et al., 2006). It has been expected that, under certain conditions for the dispersion of the frequencies,

GMR amplitude and the delay between the magnetic precession and the current oscillation, synchronization can be obtained with an output power increasing as N^2 for a collection of N STOs (Grollier et al., 2006).

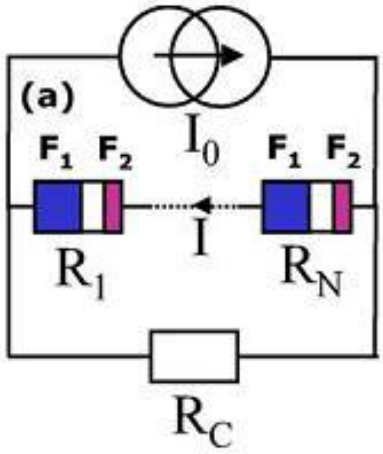

Figure 2.32: Sketch of N oscillators connected in series and coupled to a load R_C (Grollier et al., 2006).

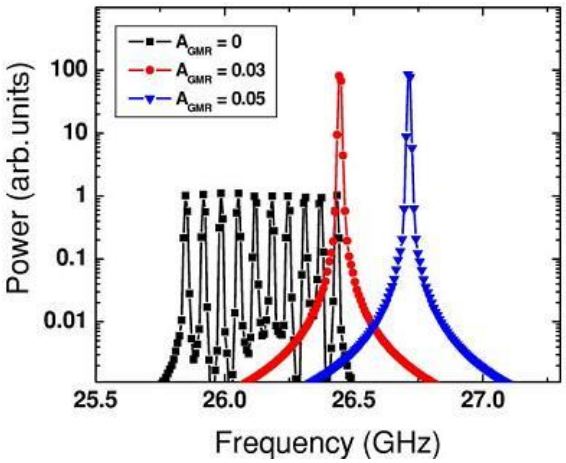

Figure 2.33: Logarithm of the power vs frequency for the set of 10 oscillators for different coupling factors A_{GMR} (Grollier et al., 2006).

Chapter 3

The Dynamic Equation and Macrospin Model

In this chapter a brief overview of the macrospin model is presented. The discussion starts with an introduction of the Landau-Lifshitz-Gilbert (LLG) equation on the basis of physical considerations on the spin magnetic moment of electrons and the well-established relationship with angular momentum through the gyromagnetic ratio in Section 3.1. As a further step, Section 3.2 describes the macrospin model of interest and the generalized Landau-Lifshitz-Gilbert equation that can be numerically solved. A general introduction of the micromagnetic simulations is also presented in Section 3.3.

3.1 The Landau-Lifshitz-Gilbert Equation

Most of the theoretical descriptions are based on the dynamic model developed by Landau and Lifshitz (Landau and Lifshitz, 1935), and subsequently modified by Gilbert (Gilbert, 1955). In this section, both Landau-Lifshitz and Gilbert

equations will be presented as a model to describe the magnetization dynamics, and the differences between them are emphasized in the discussion.

3.1.1 Gyromagnetic Precession

From quantum mechanics, it is well-known that there exists a proportionality relationship between the magnetic spin moment $\boldsymbol{\mu}$ and the angular momentum $\boldsymbol{L}$ of the electrons through the gyromagnetic ratio γ:

$$\boldsymbol{\mu} = -\gamma \boldsymbol{L} \tag{3.1}$$

where

$$\gamma = \frac{g|e|}{2m_e c} \tag{3.2}$$

with $g \simeq 2$ is the Lande g-factor (Sakurai, 1994), e is the electron charge, m_e is the electron mass and c is the velocity of light, and $\gamma = 2.21 \times 10^5\,\mathrm{mA^{-1}s^{-1}}$ is the absolute value of the gyromagnetic ratio (Chen, 2007).

With the appearance of an external magnetic field $\boldsymbol{H}$ applied on the material, a torque will be exerted on the magnetic spin moment of the electrons.

By applying the momentum theorem, the rate of change of the angular momentum can be related to the torque term exerted on the electron by the magnetic field $\boldsymbol{H}$ (Chen, 2007), which can be expressed as

$$\frac{d\boldsymbol{L}}{dt} = \boldsymbol{\mu} \times \boldsymbol{H} \tag{3.3}$$

With Eq. 3.1, this gives an equation which can be used to describe the precession of the spin magnetic moment around the direction of the external magnetic field $\boldsymbol{H}$

$$\frac{d\boldsymbol{\mu}}{dt} = -\gamma\boldsymbol{\mu} \times \boldsymbol{H} \tag{3.4}$$

The frequency of the precession is referred to as the 'Larmor frequency' (Chen, 2007)

$$f_L = \frac{\gamma H}{2\pi} \tag{3.5}$$

Eq. 3.4 can be rewritten for each spin magnetic moment within the elementary volume dV

$$\frac{d\boldsymbol{\mu}_j}{dt} = -\gamma\boldsymbol{\mu}_j \times \boldsymbol{H} \tag{3.6}$$

with the assumption that the external magnetic field $\boldsymbol{H}$ is intended to be spatially uniform within the material. By taking the volume average of both sides of Eq. 3.6, the following equation can be obtained

$$\frac{1}{dV}\frac{d\sum_j \boldsymbol{\mu}_j}{dt} = -\gamma\frac{\sum_j \boldsymbol{\mu}_j}{dV} \times \boldsymbol{H} \tag{3.7}$$

We can define the magnetization vector field $\boldsymbol{M}(\boldsymbol{r})$, such that the product $\boldsymbol{M}(\boldsymbol{r})dV$ represents the net magnetic moment of the elementary volume dV:

$$\boldsymbol{M}(\boldsymbol{r}) = \frac{\sum_j \boldsymbol{\mu}_j}{dV} \tag{3.8}$$

then one can end up with the following equation to describe the continuum gyromagnetic precession

$$\frac{\partial \boldsymbol{M}}{\partial t} = -\gamma \boldsymbol{M} \times \boldsymbol{H} \tag{3.9}$$

3.1.2 The Landau-Lifshitz Equation

The first theoretical description for this precessional motion of the magnetization was developed by Landau and Lifshitz (Landau and Lifshitz, 1935). Fundamentally, the dynamical model is constituted by a continuum precession equation (Eq. 3.9), in which the presence of quantum mechanical effects and anisotropy is phenomenologically taken into account by means of the effective field $\boldsymbol{H}_{eff}$ (d'Aquino, 2004). Then, the Landau-Lifshitz equation can be expressed as

$$\frac{\partial \boldsymbol{M}}{\partial t} = -\gamma \boldsymbol{M} \times \boldsymbol{H}_{eff} \tag{3.10}$$

Firstly, it can be observed that Eq. 3.10 is a conservative (Hamiltonian) equation (d'Aquino, 2004). In addition, if the magnetization rate of change $\frac{\partial \boldsymbol{M}}{\partial t}$ approaches to 0, Eq. 3.10 expresses the equilibrium configuration of the magnetization within the body (d'Aquino, 2004).

Nevertheless, dissipative processes take place within the dynamical magnetization processional motion (d'Aquino, 2004; Arrott, 2002). The theoretical method followed by Landau and Lifshitz consists of introducing a phenomenological torque term to represent the dissipation effect (d'Aquino, 2004). The

additional torque term that drags magnetization in the direction of the effective field is shown in Fig. (3.1) (d'Aquino, 2004). Then, the Landau-Lifshitz equation becomes

$$\frac{\partial \boldsymbol{M}}{\partial t} = -\gamma \boldsymbol{M} \times \boldsymbol{H}_{eff} - \frac{\lambda}{\boldsymbol{M}_s} \boldsymbol{M} \times (\boldsymbol{M} \times \boldsymbol{H}_{eff}) \tag{3.11}$$

with $\lambda > 0$ is a phenomenological constant characteristic of the material (Mallinson, 1987).

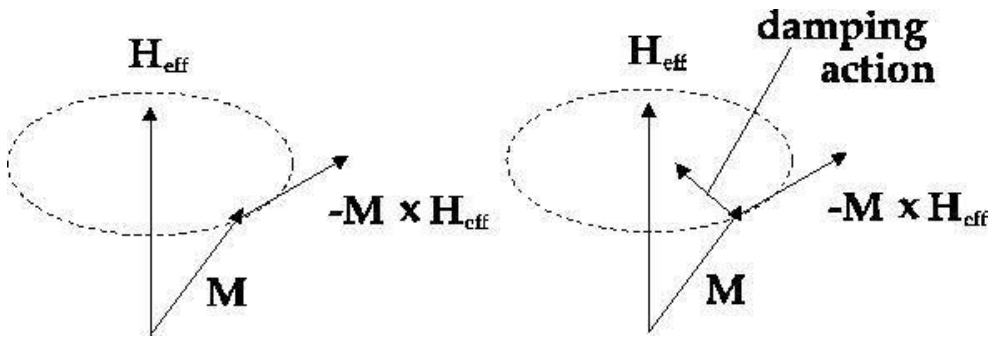

Figure 3.1: Undamped gyromagnetic precession (Left) and damped gyromagnetic precession (Right) (d'Aquino, 2004).

3.1.3 The Landau-Lifshitz-Gilbert Equation

An 'in principle' different dynamical approach was proposed in 1955 by Gilbert to describe the precessional motion of the magnetization (Gilbert, 1955). Since the conservative equation (Eq. 3.10) can be derived from a Lagrangian formulation where the components of the magnetization vector can be treated as the generalized coordinates (Gilbert, 1955), the easiest way to represent the phenomenolog-

ical dissipative process is to introduce an additional torque term, whose components are proportional to the time derivatives of the corresponding components of the magnetization vector (generalized coordinates). According to Gilbert's framework, the additional torque term can be expressed as

$$\frac{\alpha}{M_s}\boldsymbol{M} \times \frac{\partial \boldsymbol{M}}{\partial t} \tag{3.12}$$

which corresponds to the torque term generated by a field $-\frac{\alpha}{\gamma M_s}\frac{\partial \boldsymbol{M}}{\partial t}$, where $\alpha > 0$ is the Gilbert damping coefficient (Gilbert, 1955). This coefficient is also a phenomenological constant depending on the material. Similarly to the case of Landau-Lifshitz equation, the additional term introduced by Gilbert preserves the magnetization magnitude and drags the precessional magnetization to the direction of the effective field (Skrotskii, 1984; Guo and Ding, 2008). Therefore, the precessional dynamics equation (Eq. 3.10), modified by Gilbert, is generally referred to as the Landau-Lifshitz-Gilbert (LLG) equation (Guo and Ding, 2008)

$$\frac{\partial \boldsymbol{M}}{\partial t} = -\gamma \boldsymbol{M} \times \boldsymbol{H}_{eff} + \frac{\alpha}{\boldsymbol{M}_s}\boldsymbol{M} \times \frac{\partial \boldsymbol{M}}{\partial t} \tag{3.13}$$

There is substantial difference between the Landau-Lifshitz and LLG equations although they have very similar appearance in mathematical form (d'Aquino, 2004; Guo and Ding, 2008). In fact, the Landau-Lifshitz equation can be easily obtained from the LLG equation by vector multiplication of both sides of the

LLG equation by $\boldsymbol{M}$ (d'Aquino, 2004; Guo and Ding, 2008)

$$\boldsymbol{M} \times \frac{\partial \boldsymbol{M}}{\partial t} = -\gamma \boldsymbol{M} \times (\boldsymbol{M} \times \boldsymbol{H}_{eff}) + \boldsymbol{M} \times (\frac{\alpha}{\boldsymbol{M}_s} \boldsymbol{M} \times \frac{\partial \boldsymbol{M}}{\partial t}) \tag{3.14}$$

Since $\boldsymbol{M} \cdot \frac{\partial \boldsymbol{M}}{\partial t} = 0$, the equation can be rewritten to get the expression as

$$\boldsymbol{M} \times \frac{\partial \boldsymbol{M}}{\partial t} = -\gamma \boldsymbol{M} \times (\boldsymbol{M} \times \boldsymbol{H}_{eff}) - \alpha M_s \frac{\partial \boldsymbol{M}}{\partial t} \tag{3.15}$$

By substituting Eq. 3.15 in the right hand side of the LLG equation, after some manipulation, it can be shown that

$$\frac{\partial \boldsymbol{M}}{\partial t} = -\frac{\gamma}{1+\alpha^2} \boldsymbol{M} \times \boldsymbol{H}_{eff} - \frac{\gamma \alpha}{(1+\alpha^2) M_s} \boldsymbol{M} \times (\boldsymbol{M} \times \boldsymbol{H}_{eff}) \tag{3.16}$$

One can immediately notice that Eq. 3.16 and Eq. 3.11 are mathematically the same. By identifying

$$\gamma_{LL} = \frac{\gamma_{LLG}}{1+\alpha_{LLG}^2}, \quad \lambda_{LL} = \frac{\gamma_{LLG} \alpha_{LLG}}{1+\alpha_{LLG}^2} \tag{3.17}$$

the Landau-Lifshitz equation is derived from the LLG form (d'Aquino, 2004; Guo and Ding, 2008).

More recently, it has been pointed out by Podio-Guidugli (Guidugli, 2001) that both Landau-Lifshitz and LLG equations 'belong to the same family of damped gyromagnetic precession equations' (d'Aquino, 2004; Guo and Ding, 2008; Guidugli, 2001). However, some considerations about the physical meaning of the Gilbert damping coefficient γ (Guo and Ding, 2008), which can be

expressed as proportional to the ratio between the characteristics of the electrons like mass and charge, have reached the conclusion that the Landau-Lifshitz equation (Eq. 3.11) and the LLG equation (Eq. 3.13) present different physics and are identical only in the limit of vanishing damping ($\lambda_{LL} \to 0$, $\alpha_{LLG} \to 0$) (Guo and Ding, 2008; Guidugli, 2001). Nevertheless, in the limit of infinite damping ($\lambda_{LL} \to \infty$, $\alpha_{LLG} \to \infty$), the Landau-Lifshitz equation and the LLG equation respectively give (Guo and Ding, 2008; Kikuchi, 1956)

$$\frac{\partial \boldsymbol{M}}{\partial t} \to \infty, \quad \frac{\partial \boldsymbol{M}}{\partial t} \to 0 \tag{3.18}$$

Since the result given by the LLG equation is in agreement with the real fact that an extremely large damping effect should produce a very slow motion while the result obtained from the Landau-Lifshtiz equation gives the opposite trend (d'Aquino, 2004; Guo and Ding, 2008; Guidugli, 2001), we can reach the conclusion that the LLG equation is more appropriate to describe magnetization dynamics.

3.1.4 Normalized LLG Equation

In the numerical simulation, it is sometimes needed to investigate which term in the LLG equation is prevalent in given situations, then it is very useful to rewrite the LLG equation in dimensionless units. This 'normalization' considerably simplifies the expressions (d'Aquino, 2004; Guo and Ding, 2008).

By dividing both sides of the LLG equation (Eq. 3.13) by γM_s^2, it can be shown that

$$\frac{1}{\gamma M_s^2}\frac{\partial \boldsymbol{M}}{\partial t} = -\frac{1}{M_s^2}\boldsymbol{M} \times \boldsymbol{H}_{eff} + \frac{\alpha}{\gamma M_s^3}\boldsymbol{M} \times \frac{\partial \boldsymbol{M}}{\partial t} \tag{3.19}$$

Defining

$$\boldsymbol{m} \equiv \frac{\boldsymbol{M}}{M_s}, \quad \boldsymbol{h}_{eff} \equiv \frac{\boldsymbol{H}_{eff}}{M_s} \tag{3.20}$$

and by measuring the time in units of $(\gamma M_s)^{-1}$, Eq. 3.19 can be expressed in the dimensionless form

$$\frac{\partial \boldsymbol{m}}{\partial t} = -\boldsymbol{m} \times \boldsymbol{h}_{eff} + \alpha \boldsymbol{m} \times \frac{\partial \boldsymbol{m}}{\partial t} \tag{3.21}$$

3.2 Macrospin Model

The macrospin approximation assumes that the magnetization of the 'free' layer can be treated as a single macroscopic spin. Magnetization dynamics is most widely investigated using the macrospin model, and there are several excellent papers describing the macrospin model in detail and the numerical solution of the LLG equation (Ralph and Stiles, 2008; Xiao and Zangwill, 2005).

Fig. (3.2) shows the side view of a spin valve structure. A nonmagnetic spacer is 'sandwiched' between a 'fixed' ferromagnetic layer with spatially uniform magnetization $\boldsymbol{M}$ and a 'free' ferromagnetic layer with spatially uniform magnetization $\boldsymbol{m}$. The thin 'free' layer has thickness d, and the positive direct

current flow $J > 0$ is defined as electrons flowing from the 'free' to the 'fixed' layer (Ralph and Stiles, 2008; Zutic et al., 2004). As it is assumed that the magnetization is spatially uniform in both ferromagnetic layers with saturation value M_s, the magnetization of the 'fixed' layer can be expressed as $\boldsymbol{M} = M_s\hat{\boldsymbol{z}}$ while the unit vector in the direction of the magnetization of the 'free' layer $\hat{\boldsymbol{m}} = \boldsymbol{m}/M_s$ is allowed to point in any direction (Ralph and Stiles, 2008; Zutic et al., 2004). In the coordinate system as shown in Fig. (3.3),

$$\hat{\boldsymbol{m}} = \hat{\boldsymbol{x}}\sin\theta\cos\phi + \hat{\boldsymbol{y}}\sin\theta\sin\phi + \hat{\boldsymbol{z}}\cos\theta \tag{3.22}$$

Under the actual geometry and the small thickness of the 'free' ferromagnetic layer, magneto-static shape anisotropy makes the y-z plane an easy plane for $\boldsymbol{m}$, and the z axis is an easy axis in that plane (Ralph and Stiles, 2008). The external parameters are an applied magnetic field H directed along $+\boldsymbol{z}$ and an electric current J that is assumed positive when negatively charged electrons flow from $+x$ to $-x$ (Ralph and Stiles, 2008; Xiao and Zangwill, 2005).

The precessional dynamics of $\hat{\boldsymbol{m}}$ can be described using the generalized LLG equation

$$\frac{d\hat{\boldsymbol{m}}}{dt} = -\gamma\hat{\boldsymbol{m}} \times [\boldsymbol{H}_{eff} + \boldsymbol{H}_T] + \alpha\hat{\boldsymbol{m}} \times \frac{d\hat{\boldsymbol{m}}}{dt} + \frac{\gamma}{\mu_0 M_s}\boldsymbol{N} \tag{3.23}$$

Each term in this LLG equation above will be discussed in detail in the following subsections.

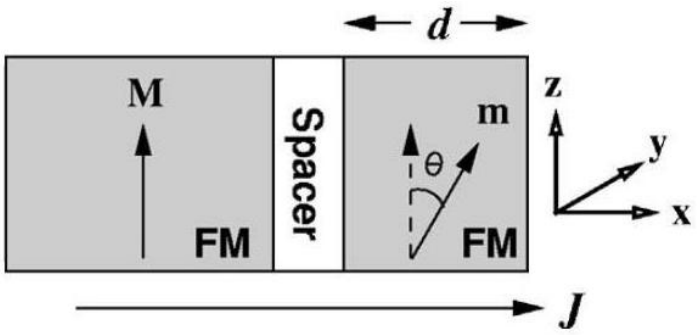

Figure 3.2: Side view of a spin valve (Zutic et al., 2004).

3.2.1 Effective Field

The first term on the right-hand side of the LLG equation (Eq. 3.23) is the conventional magnetic torque with gyromagnetic ratio γ. This torque is driven by an effective field $\boldsymbol{H}_{eff}$ derived from the total energy E of the 'free' layer

$$\mu_0 \boldsymbol{H}_{eff} = -\frac{1}{V}\frac{\partial E}{\partial \boldsymbol{m}} \tag{3.24}$$

where V is the volume of the 'free' layer (Ralph and Stiles, 2008; Xiao and Zangwill, 2005). The energy of the 'free' layer includes a Zeeman energy E_Z which is due to the external magnetic field $\boldsymbol{H}$, a magneto-static shape anisotropy energy E_s, and a surface anisotropy energy which is parametrized by K_u that vanishes in the limit that the 'free' layer thickness $d \to \infty$ (Ralph and Stiles, 2008; Xiao and Zangwill, 2005).

The Zeeman energy is

$$E_Z = \mu_0 M_s V \hat{\boldsymbol{m}} \cdot \boldsymbol{H} \tag{3.25}$$

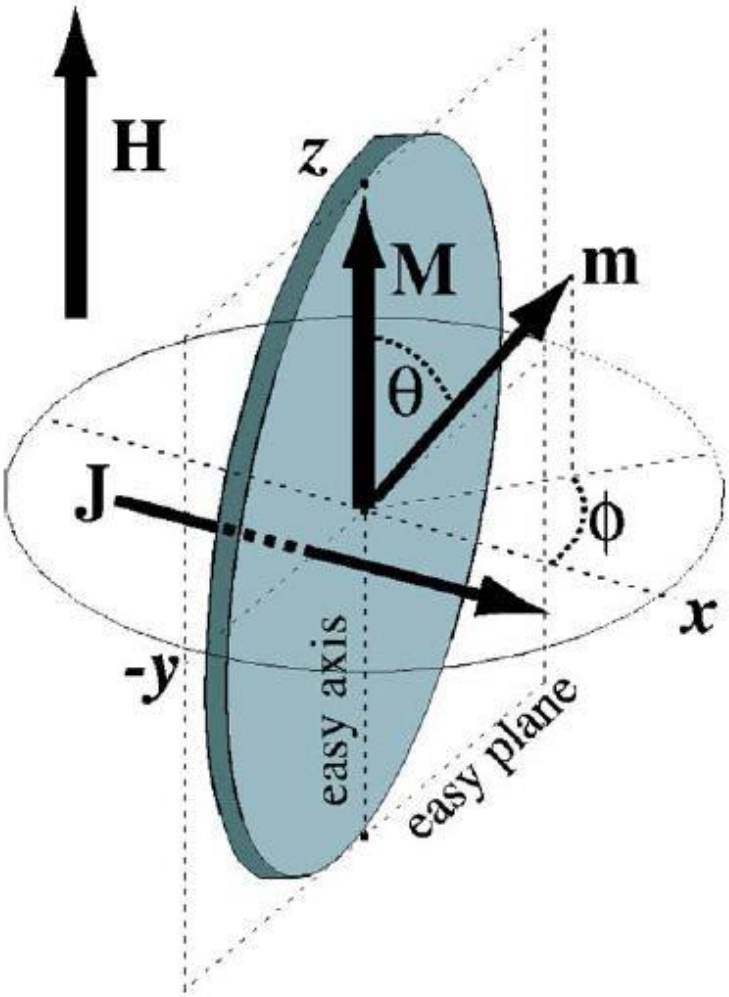

Figure 3.3: The cross section of the 'free' layer lies in y-z plane. The magnetization of the 'fixed' layer is represented by a static macrospin $\boldsymbol{M} \| \hat{\boldsymbol{z}}$. (Xiao and Zangwill, 2005)

The magneto-static shape anisotropy energy is

$$E_s = \frac{1}{2} V \mu_0 M_s \hat{\boldsymbol{m}} \cdot \boldsymbol{H}_d = \frac{1}{2} V \mu_0 M_s^2 \hat{\boldsymbol{m}} \cdot \mathcal{N} \cdot \hat{\boldsymbol{m}} \tag{3.26}$$

where $\boldsymbol{H}_d = M_s \mathcal{N} \cdot \hat{\boldsymbol{m}}$ and $\mathcal{N}$ are the demagnetization field and demagnetization tensor, respectively (Ralph and Stiles, 2008; Xiao and Zangwill, 2005). Referring to the configuration shown in Fig. (3.3), the total energy E of the 'free' layer is

$$\begin{aligned} E = \frac{1}{2} V \mu_0 M_s^2 [L \cos^2\theta + M \sin^2\theta \sin^2\phi + N \sin^2\theta \cos^2\phi] \\ -\mu_0 M_s V H \cos\theta - \frac{2VK_u}{d} \sin^2\theta \cos^2\phi \end{aligned} \tag{3.27}$$

where L, M, N are the demagnetization factors for the $\hat{z}$, $\hat{y}$, $\hat{x}$ directions respectively (Ralph and Stiles, 2008; Xiao and Zangwill, 2005). These terms can be combined to give

$$\frac{2E}{\mu_0 M_s^2 V} = h_L \cos^2\theta + h_M \sin^2\theta \sin^2\phi + h_N \sin^2\theta \cos^2\phi - 2h\cos\theta \tag{3.28}$$

where $h = H/M_s$, and

$$h_L = L - \frac{H_k}{M_s}, \quad h_M = M, \quad h_N = N - \frac{4K_u}{\mu_0 M_s^2 d} \tag{3.29}$$

3.2.2 Damping Term

The Gilbert damping term $\alpha \hat{\boldsymbol{m}} \times \frac{d\hat{\boldsymbol{m}}}{dt}$ in the generalized LLG equation (Eq. 3.23) is used to simulate the effect of energy dissipative processes, such as spin-flip scattering and coupling to lattice vibrations (Ralph and Stiles, 2008; Xiao and

Zangwill, 2005). Although opinions differ as to whether this form of damping should be adopted, this Gilbert damping term is the form that is used by most research groups (Ralph and Stiles, 2008; Zutic et al., 2004; Xiao and Zangwill, 2005). The Gilbert damping coefficient α is usually treated as a phenomenological constant depending on material, although it is not known whether this is an appropriate approximation for situations where the amplitude of magnetic precessional motion is quite large. The Landau-Lifshitz approach to damping replaces the Gilbert term by $\lambda\hat{\boldsymbol{m}} \times (\hat{\boldsymbol{m}} \times \boldsymbol{H}_{eff})$, and the constant λ is also a phenomenological constant characteristic of the material (d'Aquino, 2004; Arrott, 2002; Guo and Ding, 2008).

The difference between these two forms of damping term has been discussed in the previous section. The calculations using both forms for purposes of comparison have been performed within the macrospin model and no significant differences were found (Xiao and Zangwill, 2005).

3.2.3 Thermal Fluctuation

The stochastic vector $\boldsymbol{H}_T$ in the generalized LLG equation (Eq. 3.23) takes into account the effect of finite temperature. Each Cartesian component is chosen at random from a normal distribution with a variance chosen so the system relaxes to a Boltzmann distribution at equilibrium (Xiao and Zangwill, 2005; Xiao et al.,

2007, 2004); specifically,

$$\langle H_T^i(t) H_T^j(t') \rangle = \frac{2k_B T\alpha}{\gamma V \mu_0 M_s} \delta_{ij} \delta(t - t') \tag{3.30}$$

where $i, j = x, y, z$. It has been confirmed numerically that this procedure does indeed produce a Boltzmann distribution of energies at temperature T when $\boldsymbol{N} = 0$ in the LLG equation (Xiao and Zangwill, 2005; Xiao et al., 2007, 2004).

3.2.4 Spin-Transfer Torque

The quantity $\boldsymbol{N}$ in the generalized LLG equation (Eq. 3.24) stands for one of several torque densities that arise from microscopic considerations of the transport of electrons through a spin valve.

3.2.4.1 Spin-Transfer Torque Density

The most important among these torque densities is the spin-transfer torque density $\boldsymbol{N}_{st}$. The conduction current that flows through the spin valve as shown in Fig. (3.2) is spin polarized. Because of the non-collinearity between $\boldsymbol{M}$ and $\boldsymbol{m}$, the incident electron spins that encounter the 'free' layer generally possess a component of angular momentum that is transverse to the magnetization of the 'free' layer itself. This transverse component of angular momentum is largely absorbed by the ferromagnetic layer. Since the 'free' layer is described as a uniformly magnetized body and its magnetization can be treated as a single macroscopic spin, the absorbed angular momentum exerts a torque which is represented on

the right-hand side of Eq. 3.23. Confirmed by a variety of theoretical methods (Slonczewski, 2002; Fert et al., 2004),

$$\boldsymbol{N}_{st} = \eta(\theta)\frac{\hbar}{2e}\frac{J}{d}\hat{\boldsymbol{m}} \times [\hat{\boldsymbol{m}} \times \hat{\boldsymbol{M}}] \tag{3.31}$$

where $\hat{\boldsymbol{M}} = \boldsymbol{M}/M_s$ and $\cos\theta = \hat{\boldsymbol{m}} \cdot \hat{\boldsymbol{M}}$, and it is usually referred to as the 'in-plane' component of the spin-transfer torque.

The different forms of spin-transfer torque that can be found in the literature correspond to different forms for $\eta(\theta)$. The easiest manner is to put $\eta(\theta) = \eta_0$; the result derived from this assumption is a 'sine' approximation to the torque because the remaining angular factors in Eq. 3.31 suggest that the spin-transfer torque density $\boldsymbol{N}_{st}$ is proportional to $\sin\theta$ ($\boldsymbol{N}_{st} \propto \sin\theta$) (Xiao and Zangwill, 2005; Xiao et al., 2004). This form of the torque arises when there is spin-dependent scattering at the 'free' layer interface and the polarization of the injection electrons that flow from the 'fixed' layer to the 'free' layer is independent of the orientation of the 'free' layer. The coefficient $\eta(\theta)$, however, is not always a constant if there is a diffusive component to the current or spin-dependent reflection occurs at the interface (Xiao and Zangwill, 2005; Xiao et al., 2004). These effects are presented in transport theory calculations of $\boldsymbol{N}_{st}$ (Fert et al., 2004).

In 1996, Slonczewski (Slonczewski, 1996, 2002) adopted an approximate form of magnetoelectronic circuit theory (Tserkovnyak et al., 2002) to a spin valve.

The coefficient $\eta(\theta)$ in $\boldsymbol{N}_{st}$ is expressed as

$$\eta(\theta) = \frac{q}{A + B\cos\theta} \tag{3.32}$$

where q, A, and B are material and geometric parameters. This form of $\boldsymbol{N}_{st}$ is usually referred to as the symmetric Slonczewski approximation for the torque (Xiao and Zangwill, 2005).

For the general configuration of a spin valve, it turns out that

$$\eta(\theta) = \frac{q_+}{A + B\cos\theta} + \frac{q_-}{A - B\cos\theta} \tag{3.33}$$

which is referred to as the asymmetric Slonczewski approximation (Xiao and Zangwill, 2005).

Spin-transfer torque represents the non-equilibrium processes that can not be described in energy functional terms. This means that $\boldsymbol{N}_{st}$ does not generate an effective field and no damping of spin-transfer dynamics occurs if $\boldsymbol{H}_{eff} = 0$ and the Landau-Lifshitz form is used for this damping effect (d'Aquino, 2004; Guo and Ding, 2008). On the other hand, since transferring energy to other degrees of freedom may influence the spin-transfer driven motion of the magnetization in the 'free' layer, it is necessary to adopt the Gilbert damping term in the magnetization equation of motion (Xiao and Zangwill, 2005).

3.2.4.2 Current-Induced Effective Field

First-principles calculation shows that the absorption of transverse spin-polarized current at the ferromagnetic interface is not necessarily 100% efficient (Zutic et al., 2004). The remaining fraction gives a slight correction to $\eta(\theta)$ in Eq. 3.31. The remainder is polarized perpendicular to both $\boldsymbol{m}$ and $\boldsymbol{M}$ and contributes a torque density on the 'free' layer of the form

$$\boldsymbol{N}_{eff} = \eta(\theta)\beta\frac{\hbar}{2e}\frac{J}{d}\hat{\boldsymbol{m}} \times \hat{\boldsymbol{M}} \tag{3.34}$$

According to circuit theory, this term is described by the imaginary part of the mixing conductance (Brataas et al., 2000). Apparently, $\boldsymbol{N}_{eff}$ produces motion of $\hat{\boldsymbol{m}}$ identical to that produced by an effective external field oriented along the magnetization direction $\hat{\boldsymbol{M}}$ of the 'fixed' layer, which is generally referred to as the 'out-of-plane' component of the torque.

The contribution of this perpendicular torque term is usually neglected in the calculations because it is much smaller than the 'in-plane' component ($\beta \approx 0.01$ in GMR based spin valve); but this kind of contribution is of critical importance in TMJ devices, since it has been interpreted as demonstrating that $\beta \approx 0.25$ (Zimmler et al., 2004).

3.2.4.3 Spin Pumping

The last contribution to the spin-transfer torque on the 'free' layer originates from the phenomenon which is generally called 'spin pumping' effect. Since the spin-polarized current incident from the nonmagnetic layer can produce magnetization dynamics in the adjacent ferromagnetic 'free' layer, it is possible that the motion of the magnetization of the ferromagnetic layer may influence the spin-polarized current in the adjacent nonmagnetic layer. The most prominent effect is the injection of a spin current into the nonmagnetic layer whenever the magnetization moves. One consequence of the injected spin current is a back-reaction torque that increases the damping of the spin motion (Tserkovnyak et al., 2002; Mills, 2003). This effect has been confirmed by experiments (Ingvarsson et al., 2002; Lenz et al., 2004). The torque density due to spin pumping is given as

$$\boldsymbol{N}_{sp} = \frac{1}{d}\hat{\boldsymbol{m}} \times \boldsymbol{J}_s^{exch} \times \hat{\boldsymbol{m}} \tag{3.35}$$

where $\boldsymbol{J}_s^{exch}$ is the dynamic-exchange current induced by the 'spin pumping' effect (Tserkovnyak et al., 2005).

3.3 Micromagnetic Modeling

However, for many complex systems the macrospin approximation breaks down. For a better understanding of magnetic dynamics, a micromagnetics approach is therefore necessary (Berkov and Miltat, 2008).

The first complete formulation of the micromagnetics method is developed by Brown (W. F. Brown, 1963). In the micromagnetics method, the size of the elementary computational cell is an order of magnitude smaller than the width of a domain wall and much smaller than the extent of domains, and the domains are not postulated but must be derived from the formulation (Hubert and Schafer, 1998). The concept is based on the assumption that the magnitude of the magnetization $\boldsymbol{M}$ is constant for each elementary cell but their directions can change with positions, similar to the concept proposed by Landau and Lifshitz (Hubert and Schafer, 1998; Hillebrands and Ounadjela, 2002). Exchange interaction is formulated as a second order derivative of magnetization with respect to spatial coordinates; and the anisotropy is expressed in terms of the polar angle between $\boldsymbol{M}$ and the uniaxial anisotropy direction. Additionally, the demagnetization is expressed as a spatial integral of the product of an interaction kernel with the magnetization $\boldsymbol{M}$ (Miltat et al., 2002). Analytically, it was possible to solve one-dimensional problems only, like a Bloch wall in an infinitely thick material, where the static interaction can be neglected, or for the Neel wall in a film with theoretically zero thickness (Berkov and Miltat, 2008).

In general, the problem in the micromagnetics method is its three dimensional nature and involves non-linear calculations of both the local interactions represented by exchange and the long-range interactions represented by the de-

magnetization.

With the development of high performance scientific computation, more recently the effectiveness of micromagnetics has been greatly improved, and micromagnetic simulation becomes dominant in the investigation of magnetic dynamics.

In numerical micromagnetics simulations there are two ways to calculate the distribution of the magnetization directions for the model system (Hubert and Schafer, 1998; Hillebrands and Ounadjela, 2002; Miltat et al., 2002):

1. Static Method

In the static method, the magnetization of each computational cell is rotated slowly to the direction of the effective field $\boldsymbol{H}_{eff}$ at that position, and this rotation is compared with a preset tolerance value for all elementary cells throughout the material. The process of rotating the magnetization vectors subsequently in each elementary cell throughout the computational box is continued until the maximum angle is smaller than the required tolerance. It can be shown that in this method the energy always decreases from one iteration to the next (Berkov and Miltat, 2008; Hubert and Schafer, 1998). This method has an advantage if only one minimum exists, but in the case when there are at least two energy minimum values, with a certain barrier between them, the minimization process can converge to the higher minimum without ever crossing over to the lower

minimum (Hubert and Schafer, 1998; Hillebrands and Ounadjela, 2002; Miltat et al., 2002). The micromagnetic formulation based on energy minimization was first used for two-dimensional wall calculations by LaBonte (LaBonte, 1969) and Hubert (Hubert, 1969). For the time being this method is less applied compared to the dynamic one.

2. Dynamic Method (LLG equation of motion)

The torque formulation of the magnetization dynamics described by the Landau-Lifshitz equation was later modified by Gilbert (Gilbert, 1955), using a Lagrange formulation proposed by Döring (Dörling, 1948), to include the damping term in a more consistent manner. The Gilbert formulation of the Landau-Lifshitz equation (LLG equation) is used in the dynamic method.

In the dynamical approach, the LLG equation is numerically integrated for each elementary cell in subsequent fractions of the precession time, and the elementary cell is considered to be homogeneous (Berkov and Miltat, 2008). The direct integration of the LLG equation is carried out until the value of $d\boldsymbol{M}/dt$ is smaller than a preset tolerance value for each elementary cell. In the absence of the external applied magnetic field, the damping parameter can be chosen arbitrarily. It seems that in this situation the dynamical method is not advantageous compared to the static approach (Berkov and Miltat, 2008; Miltat et al., 2002), but actually the result of a dynamic calculation is checked by applying an exter-

nal field pulse and leaving the system to relax and in this way the system will be driven to the lower minimum (Aharoni, 2000).

In most cases static magnetization configurations are in the focus of the research, e.g.: Bloch-Neel wall transition as a function of the film thickness, domain wall structures in nanocrystalline alloys, etc (Hubert and Schafer, 1998; Hillebrands and Ounadjela, 2002; Miltat et al., 2002).

Chapter 4

Capacitance Effect on Microwave Power Spectra of Spin-Torque Oscillator with Thermal Noise

A macro-spin simulation has been carried out to study the thermal stability of a spin-torque oscillator (STO) connected in parallel with a capacitance.

4.1 Introduction

Theory predicted and experiments verified that a spin-polarized current can exert a torque on a nano-sized magnet, which is able to sustain steady precessional motion of the magnetization by counteracting the Gilbert damping. If the nano-magnet is the 'free' layer of a spin valve structure, the steady precession causes a periodic variation of the device resistance, due to giant magneto-resistance (GMR) or tunneling magneto-resistance (TMR) effects, resulting in a detectable *ac* voltage. Such devices, named Spin-Torque Oscillators (STOs), are able to generate frequencies ranging from 5 to 40 GHz, which can be tuned by adjusting

the applied magnetic field and current. STOs have demonstrated quality factors ($Q = f/\Delta f_{FWHM}$) as high as 18,000, which make them appealing as nano-scale radiation sources in wireless communication.

Theoretical efforts to better understand these spin-transfer effects have included analytical approaches, numerical single-domain modeling, and more recently, micromagnetic simulations. Although theory has been able to describe quantitatively many of the experimental facts, there are still a number of results which have not yet found a satisfactory theoretical explanation. At present, a lot of effort is set to model the effect of temperature in STO. In terms of applications, the influence of thermal fluctuations (thermal noise) on STO operation is of critical importance; in the presence of thermal fluctuations, the microwave power spectrum is expected to broaden, decrease in amplitude and shift in frequency with increasing temperature.

In this chapter, to study the impact of realistic thermal fluctuation on an STO, a stochastic magnetic field vector is added into the Landau-Lifshitz-Gilbert-Slonczewski (LLGS) equation. By solving numerically the LLGS equation, we simulate the interaction between an STO and a capacitance connected in parallel, and investigate how the capacitance value influences the thermal stability of the STO system.

4.2 Theoretical Consideration and Numerical Calculation

4.2.1 System Configuration

A giant magneto-resistance (GMR) based STO consisting of a thick magnetic 'fixed' layer, nonmagnetic spacer layer, and a thin 'free' layer is connected in parallel with a capacitance, and an ideal *dc* source I_{dc} is applied (see Fig. (4.1)).

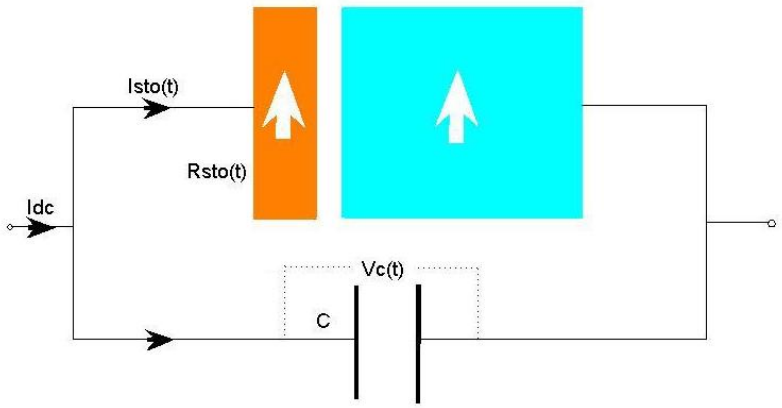

Figure 4.1: Sketch of an STO connected in parallel with a capacitance.

4.2.2 Model Description

The time-evolution of the 'free' layer magnetization is determined by the Landau-Lifshitz-Gilbert (LLG) equation with the Slonczewski spin torque term

$$\frac{d\hat{\boldsymbol{m}}}{dt} = -\gamma\hat{\boldsymbol{m}} \times [\boldsymbol{H}_{eff} + \boldsymbol{H}_T] + \alpha\hat{\boldsymbol{m}} \times \frac{d\hat{\boldsymbol{m}}}{dt} + \gamma\alpha_J\hat{\boldsymbol{m}} \times (\hat{\boldsymbol{m}} \times \boldsymbol{M}) \qquad (4.1)$$

where $\hat{\boldsymbol{m}}$ is the unit vector of the 'free' layer magnetization of the STO, γ is the gyromagnetic ratio, and α is the Gilbert damping parameter. $\boldsymbol{H}_{eff}$ is the effective magnetic field acting on the 'free' layer, which consists of the contribution of the uniaxial magnetic anisotropy field $\boldsymbol{H}_k$, the demagnetization field $\boldsymbol{H}_d$ and an external 'in-plane' applied magnetic field $\boldsymbol{H}_{app}$. The stochastic magnetic field vector $\boldsymbol{H}_T$ is used to represent the effect of finite temperature, and each spatial component of it is chosen at random from a normal distribution. The last term in Eq. 4.1 is the Slonczewski spin torque term, where $\alpha_J = \eta I/2\mu_0 M_s e V_f$ is the spin torque magnitude, with η being the polarization ratio, μ_0 the magnetic vacuum permeability, V_f the volume of the 'free' layer, and M_s the saturation magnetization.

The presence of capacitance will only allow an alternating current to flow through without shunting the total direct current I_{dc} from the STO branch. Considering the continuity of the total *dc* current and equal voltage drop across the two parallel branches, we have the following equations:

$$R_{STO}(t) = \frac{R_{AP} + R_P}{2} - \frac{R_{AP} - R_P}{2}\cos\theta(t) \tag{4.2}$$

$$I_{STO}(t) + \frac{C dV_C(t)}{dt} = I_{dc} \tag{4.3}$$

$$V_C(t) = I_{STO}(t) R_{STO}(t) \tag{4.4}$$

where R_{AP} and R_P are the anti-parallel and the parallel resistance of the STO respectively, $\theta(t)$ is the angle between the magnetization of the 'fixed' layer and that of the 'free' layer, $V_C(t)$ is the instantaneous voltage across the capacitance, and $I_{STO}(t)$ is the instantaneous current flowing through the STO branch, as shown in Fig. (4.1).

Then, after some manipulation, Eq. 4.2, Eq. 4.3 and Eq. 4.4 yield

$$\frac{dI_{STO}}{dt} = \frac{I_{dc} - I_{STO}(t) - CI_{STO}(t) \cdot dR_{STO}(t)/dt}{CR_{STO}(t)} \tag{4.5}$$

The magnetization dynamics of the STO system is given by the solution of Eq. 4.1 and Eq. 4.5, which can be numerically solved by adopting a fourth-order Runge-Kutta algorithm.

The emission power spectra are derived by Fast Fourier Transform (FFT), and we extract the signal characteristics from Lorentzian fitted profiles, from which we obtain output power amplitude, frequency, the full width at half maximum linewidth (FWHM), and quality factor Q.

4.2.3 Fourth-order Runge-Kutta Method

The fourth-order Runge-Kutta algorithm is one of the standard methods to solve differential equations. The algorithm has more precision than Euler method, and it is easy to start programming and relatively fast. The fourth-order Runge-Kutta algorithm is generally considered to provide an excellent balance of power,

precision, and simplicity to program (Cellier and Kofman, 2006).

There are four gradient or 'k' terms which provide a better approximation and convergence to the behavior of the function $f(t, y)$ near the intermediate point $(t_{n+\frac{1}{2}}, y_{n+\frac{1}{2}})$ to calculate y_{n+1}:

$$\begin{aligned} y_{n+1} &= y_n + \frac{1}{6}(k_1 + 2k_2 + 2k_3 + k_4) \\ k_1 = hf(t_n, y_n), \quad k_2 &= hf(t_n + \frac{h}{2}, y_n + \frac{k_1}{2}) \\ k_3 = hf(t_n + \frac{h}{2}, y_n + \frac{k_2}{2}), \quad k_4 &= hf(t_n + h, y_n + k_3) \end{aligned} \tag{4.6}$$

Note that the Runge-Kutta algorithm can converge to the Stratonovich solution depending on the coefficients, and the extra gradients can still be programmed with four calls to the same subroutine (Cellier and Kofman, 2006).

4.2.4 Fast Fourier Transform Algorithm

To see the effects of the thermal noise, the power spectral density (PSD) of the output signal should be studied. The Fourier transform was done with the FFT algorithm, which is a Discrete Fourier Transform (DFT). It is important to notice that this algorithm works properly with two conditions:

- Number of data points proportional to a power of 2.
- The data should have an integer number of periods.

If the latter condition is not satisfied, the resulting FFT will show the so-called 'frequency leakage'. Since it is almost impossible to satisfy both conditions at the

same time, a 'window function', which multiplies the data points, is used. The most common case in which the first condition is satisfied and no window is used, is referred to as the use of a rectangular window because the signal only exists in the sample (see Fig. (4.2)) (Cattani and Rushchitsky, 2007). In fact, the Fourier transform is an integral from $-\infty$ to ∞, so the integration of a sample corresponds to integrating an infinite signal multiplied by a pulse of a certain width. We know that a multiplication in time corresponds to convolution in Fourier space, and that the Fourier transform of a pulse is a sinc, so the frequency leakage is originated from the convolution of the sinc with the Fourier transform of the signal. In the case of a sine wave, we get a sinc at the frequency of oscillation (squared in the PSD)

To prevent this effect, the windows are usually functions that are almost zero at the ends of the sample. A large number of windows have been developed for different situations. We will use 2 windows, the 4 term Blackman-Harris window (Fig. (4.3)) which offers extremely low frequency leakage but a bad ENBW (Equivalent Noise Bandwidth) which describes the broadening of the central lobe, and the Blackman window (Fig. (4.4)) which offers a better ENBW and fairly low frequency leakage (Cattani and Rushchitsky, 2007).

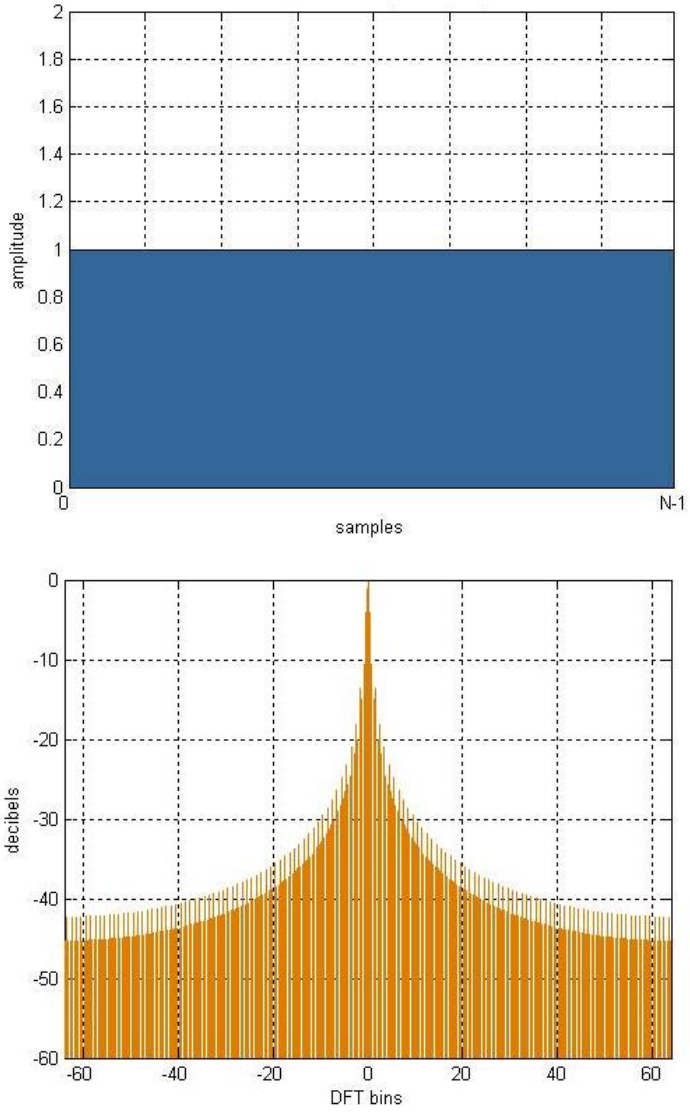

Figure 4.2: Rectangular window function (Top) and spectral leakage from a sinusoid (Bottom) (Cattani and Rushchitsky, 2007).

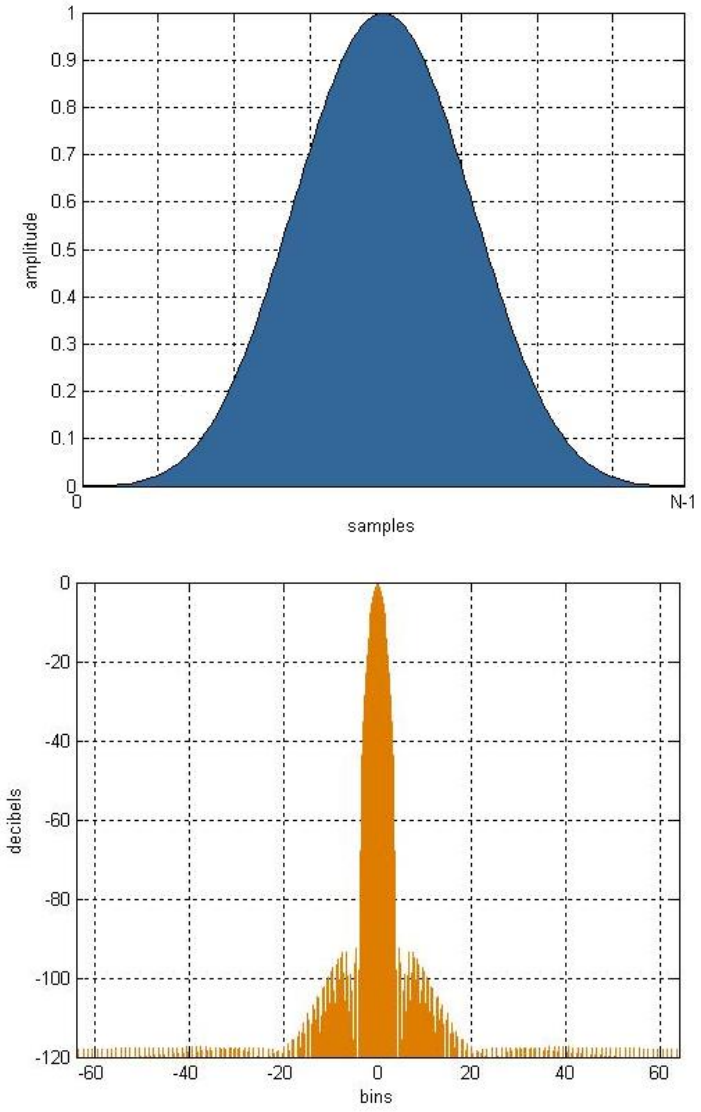

Figure 4.3: 4 term Blackman-Harris window function (Top) and the frequency response (Bottom) (Cattani and Rushchitsky, 2007).

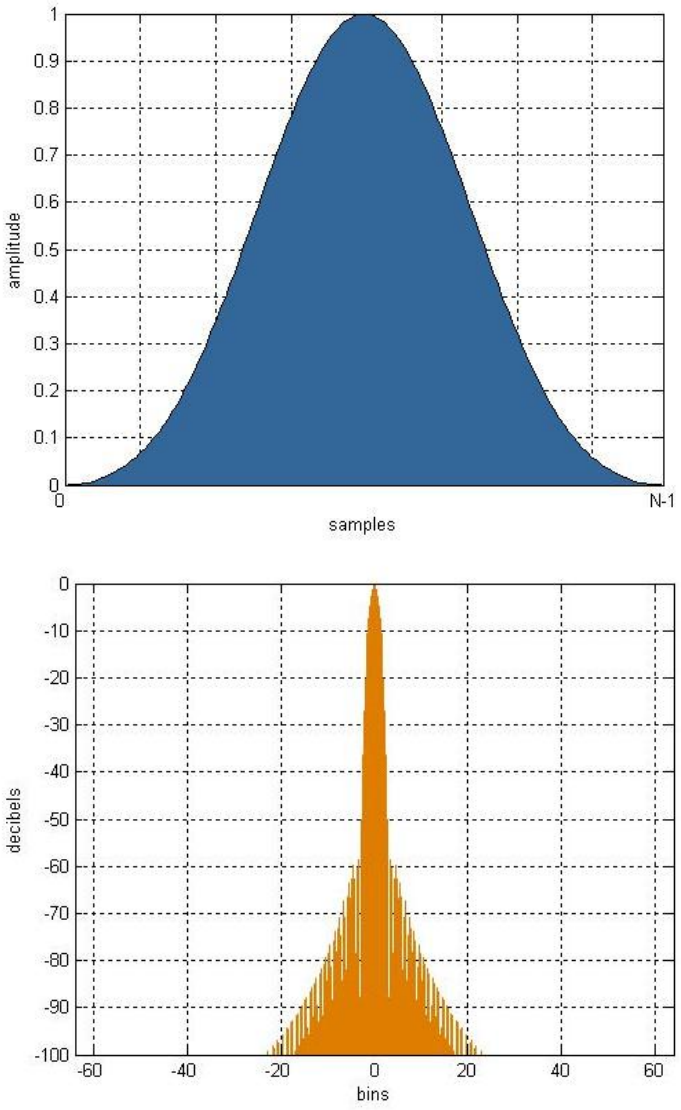

Figure 4.4: Blackman window function (Top) and the frequency response (Bottom) (Cattani and Rushchitsky, 2007).

4.3 Results and Discussion

To simulate a typical GMR based trilayer spin valve, the following primary parameters are adopted: $\alpha = 0.008$, $\gamma = 1.85 \times 10^{11}$ Hz/T, $\eta = 0.54$, $H_{app} = 0.05$ T, $H_d = 4\pi M_s = 0.127$ T, $H_k = 0.02$ T, $R_P = 15.8\ \Omega$, $R_{AP} = 23.4\ \Omega$, and the applied *dc* current $I_{dc} = 8$ mA.

In order to obtain an adequate spectral resolution in the FFT algorithm, long-time simulations (up to 2000 ns, in our case) have to be performed. The time step used in the simulation has to be small enough (0.2 ps) to guarantee numerical convergence and high resolution, which leads to considerable computational effort. Thus, 3 million data points are adopted, and the data are sampled at intervals of 0.6 ps, which give a resolution of 850 kHz. Also, to have a cleaner Fourier transformed spectra, the simulation and FFT are repeated 10 times so that the spectral data may be averaged, and a smoothing of the curve using the Savitsky-Golay method of polynomial fits was used (Savitzky and Golay, 1964).

4.3.1 Resistance of the STO

Fig. (4.5) shows a typical simulation result of the resistance of the oscillation as a function of time. At the very beginning, no capacitance is connected, and the oscillation reaches steady state; at $t = 50$ ns, a capacitance $C = 50$ pF is added in the circuit.

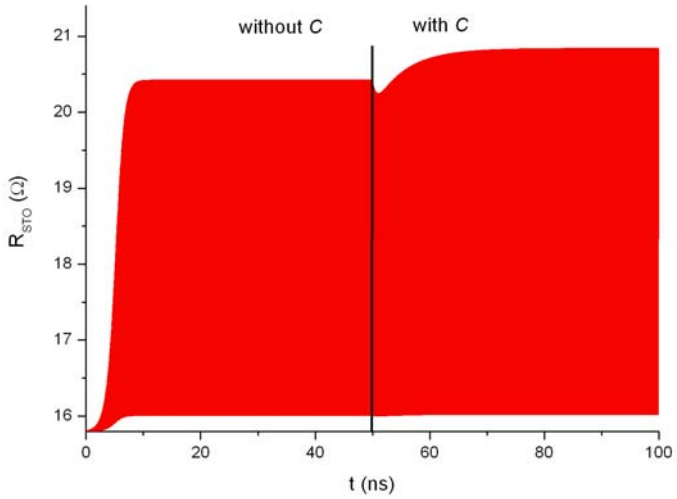

Figure 4.5: Resistance of STO as a function of time.

An enlarged version of the oscillations against time increment is shown in Fig. (4.6). The STO is settled into a steady state precession, and the oscillation of R_{STO} is sinusoidal.

4.3.2 Microwave Power Spectra

In Fig. (4.7) and Fig. (4.8), we show the power spectra of a single STO connected with and without the capacitance $C = 2$ pF at $T = 30$ K and $T = 100$ K.

In the power spectra, it can be observed that, with increasing temperature, the FWHM broadens and the power amplitudes drop dramatically.

At $T = 30$ K, when the capacitance is not connected in the circuit, the fitted Q value is 1550; and when the capacitance is connected in parallel with the STO,

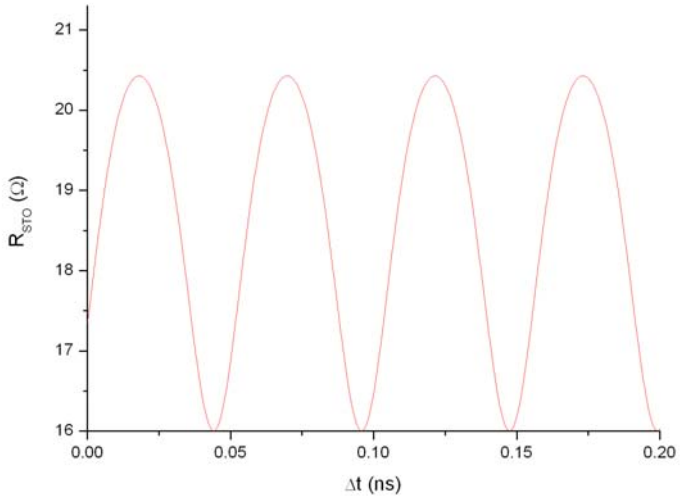

Figure 4.6: Resistance vs Δt.

the Q value is 4200. At $T = 100$ K the fitted Q values are 1100 and 2300 respectively. The power spectrum amplitudes at the two temperatures decrease 44% and 52% respectively, comparing with and without the capacitance in the circuit.

It is quite encouraging that the addition of a small capacitance can positively improve the thermal stability of the STO system and enhance the quality factor Q by a factor of about 2.

Increasing the capacitance is also found to improve the thermal stability of the system even further.

Fig. (4.9) and Fig. (4.10) show the emission power spectra at $T = 30$ K and $T = 100$ K with $C = 100$ pF connected in the circuit respectively. The fitted Q

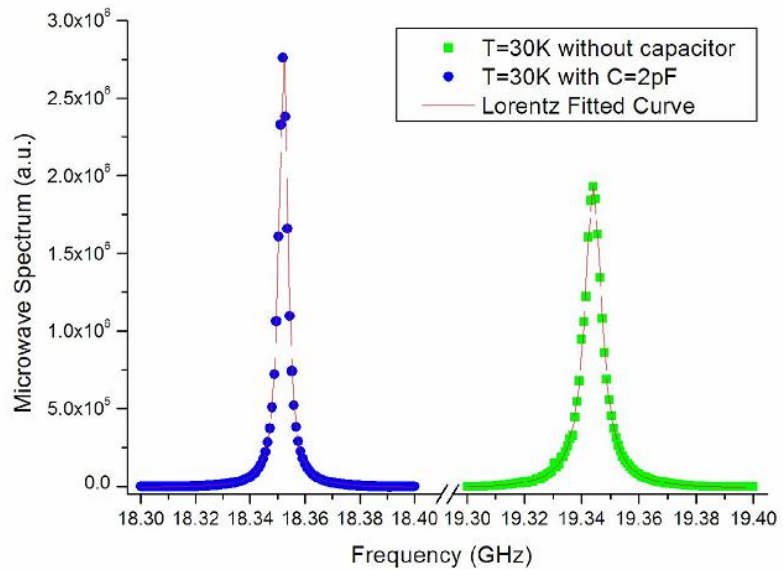

Figure 4.7: Frequency spectra of the *dc*-driven magnetization oscillations at $T = 30$ K without capacitance and with capacitance $C = 2$ pF; Lorentzian fittings are also shown.

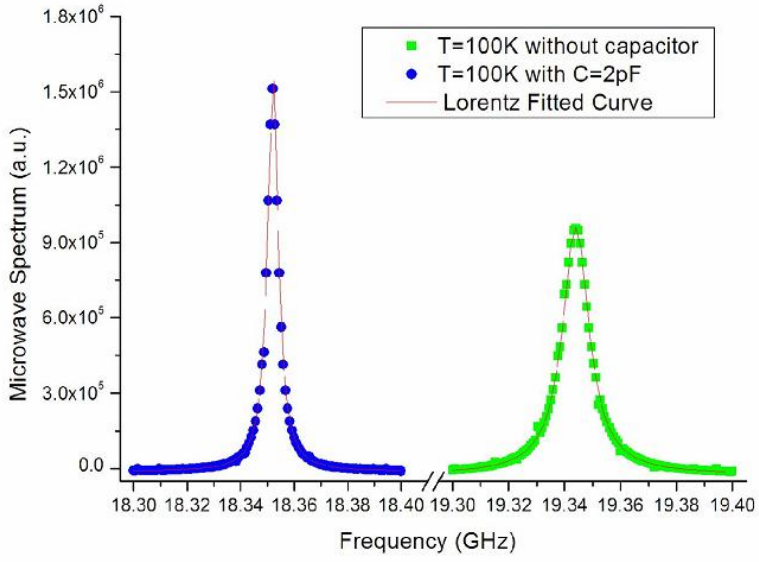

Figure 4.8: Frequency spectra of the *dc*-driven magnetization oscillations at $T = 100$ K without capacitance and with capacitance $C = 2$ pF; Lorentzian fittings are also shown.

values are 8170 and 7010 respectively, and the power spectrum amplitude at the two temperatures drops only 11%.

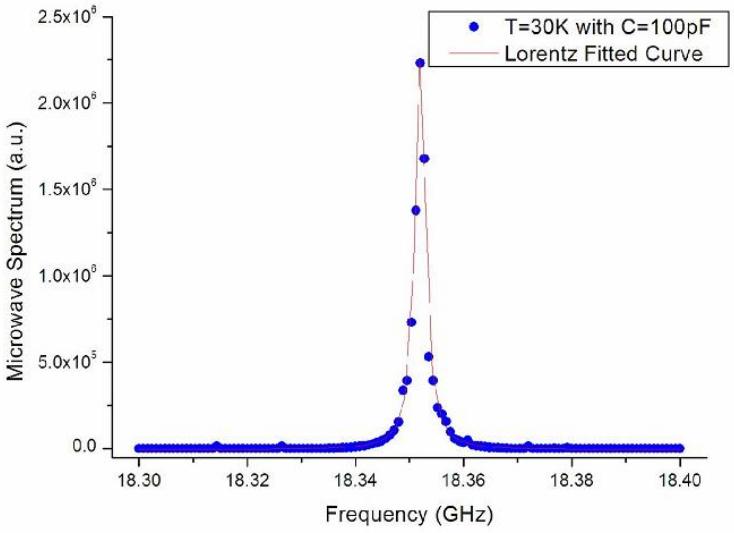

Figure 4.9: The calculated power spectrum at $T = 30$ K and capacitance $C = 100$ pF, with Lorentzian fitting curve.

But with an even larger capacitance, say $C = 200$ pF, connected in the circuit, the influence on the thermal stability is totally opposite (see Fig. (4.11) and Fig. (4.12)). As the power spectrum signal is quite noisy even at low temperature, the spectrum amplitude has been suppressed and the fitted Q factors can not adequately represent the real situation.

A possible factor that may contribute to this capacitance effect on microwave spectra is the amplitude of the precession. It can be observed that the amplitude of the oscillation is larger when the capacitance is connected with the STO than

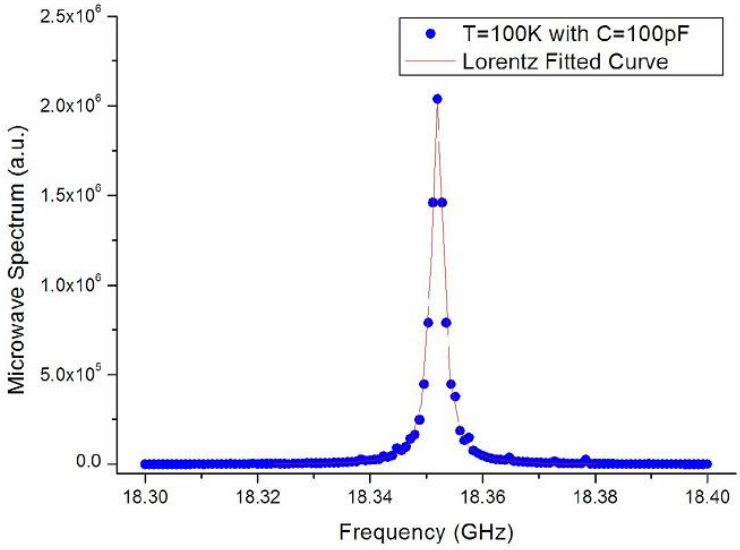

Figure 4.10: The calculated power spectrum at $T = 100$ K and capacitance $C = 100$ pF, with Lorentzian fitting curve.

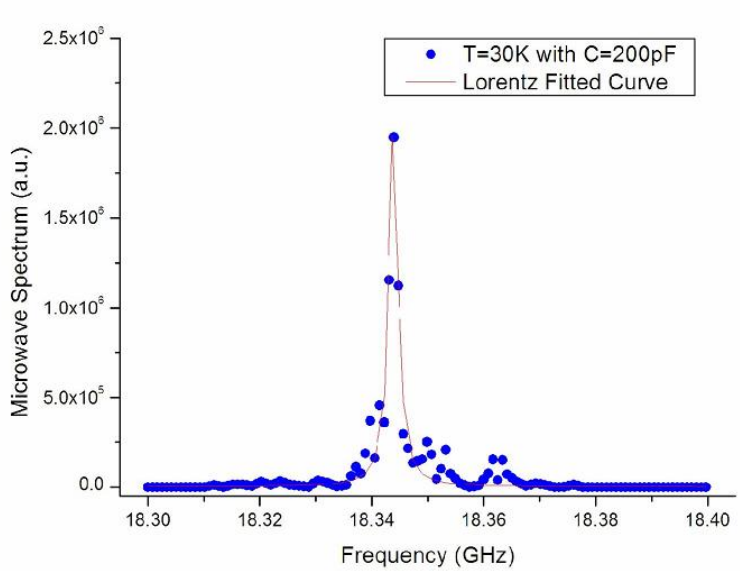

Figure 4.11: The calculated power spectrum at $T = 30$ K with capacitance $C = 200$ pF. Lorentzian fitting is also shown.

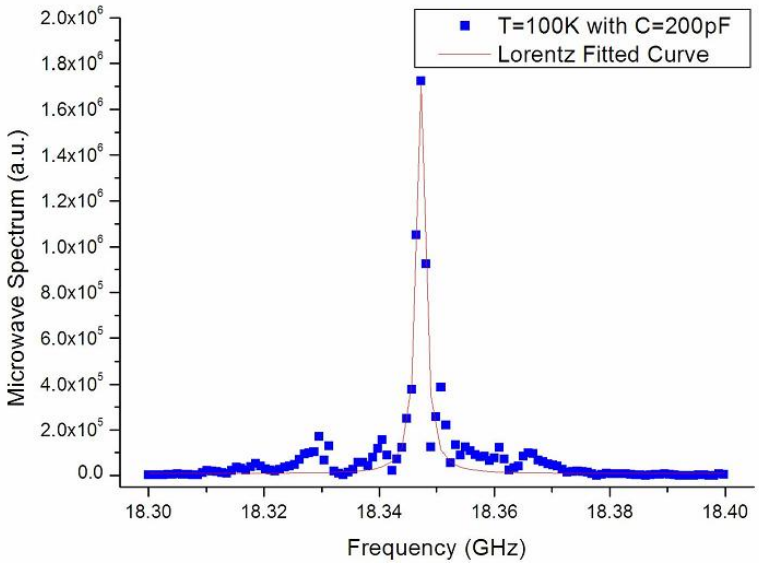

Figure 4.12: The calculated power spectrum at $T = 100$ K with capacitance $C = 200$ pF. Lorentzian fitting is also shown.

without (see Fig. (4.13) and Fig. (4.14)). Smaller oscillation amplitudes make the dynamics more sensitive to thermal fluctuations in quality factor, amplitude, and frequency in the power spectrum.

But with an even larger capacitance in the circuit, it introduces a larger *ac* current in the STO branch, and causes fluctuations in the precessional dynamics (as shown in Fig. (4.15)). Actually, the orbit indeed spreads with high capacitance when it is connected in the circuit; the capacitance effect drives the magnetization precessional orbit more into and out of the steady orbit (black curve), expanding and contracting the cone of precession, leading to a negative influence on the thermal stability of the system. The $I - V$ diagram is shown in Fig. (4.16), with

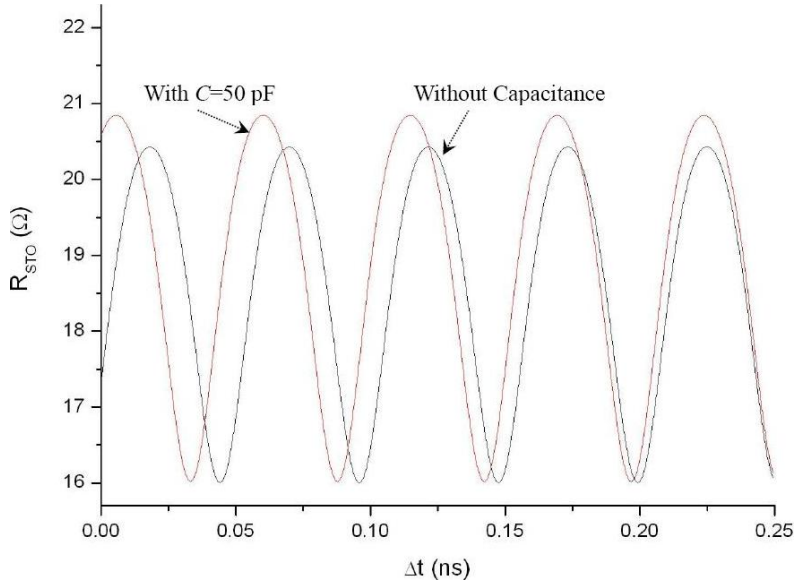

Figure 4.13: Resistance vs t at $T = 100$ K with $C = 50$ pF.

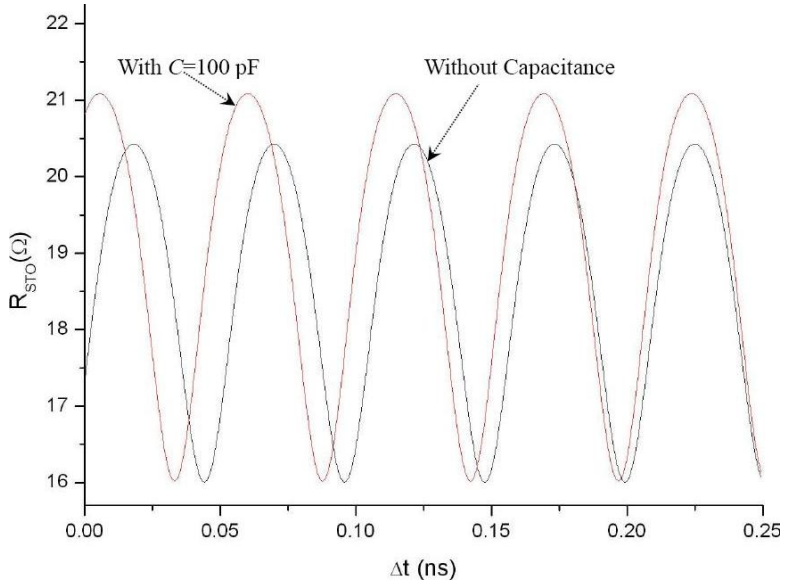

Figure 4.14: Resistance vs t at $T = 100$ K with $C = 100$ pF.

a capacitance $C = 200$ pF connected in the circuit, considerable fluctuation in the current (green curve) can be observed.

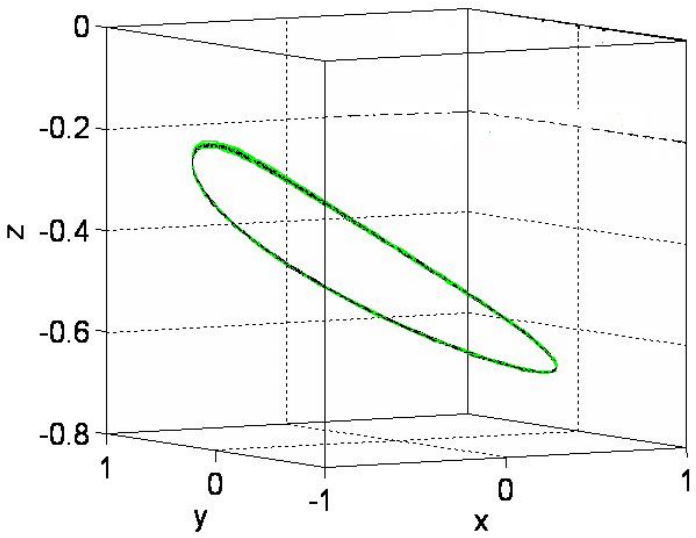

Figure 4.15: Magnetization precessional orbit of $\hat{\boldsymbol{m}}$ with $C = 200$ pF at $T = 30$ K.

The capacitance effect on the Q factor of the microwave power spectra of the STO is shown in Fig. (4.17)

4.3.3 The $I - V$ Phase Shift

Lastly, the result of $I-V$ phase shift, i.e. phase difference between the *ac* current and the voltage across the STO branch, (see Fig. (4.18)) shows that with certain capacitance, the phase shift is 90 degree, which suggests that there may be an optimum capacitance for which the performance of the self-oscillation system can be most enhanced.

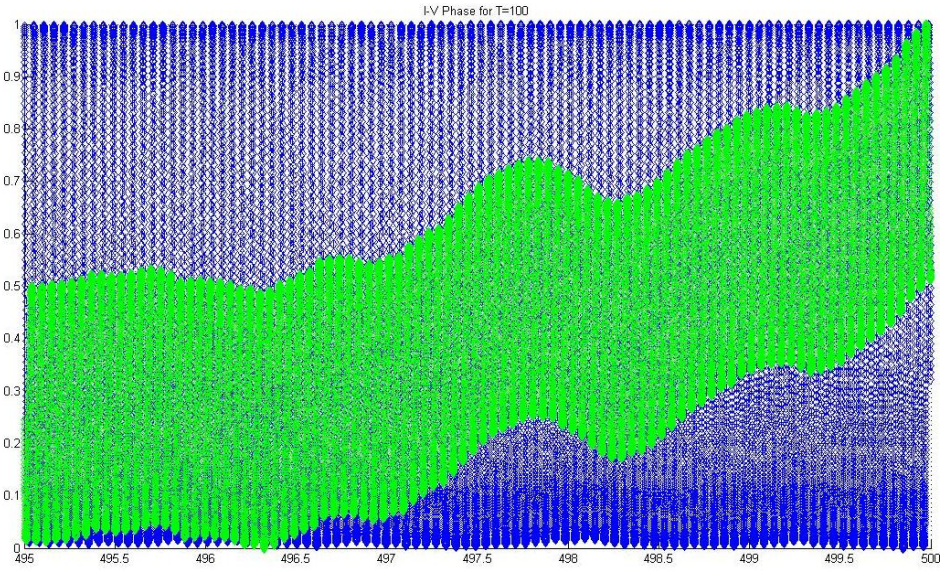

Figure 4.16: The $I - V$ diagram at time interval of 5 ns with $C = 200$ pF at $T = 100$ K.

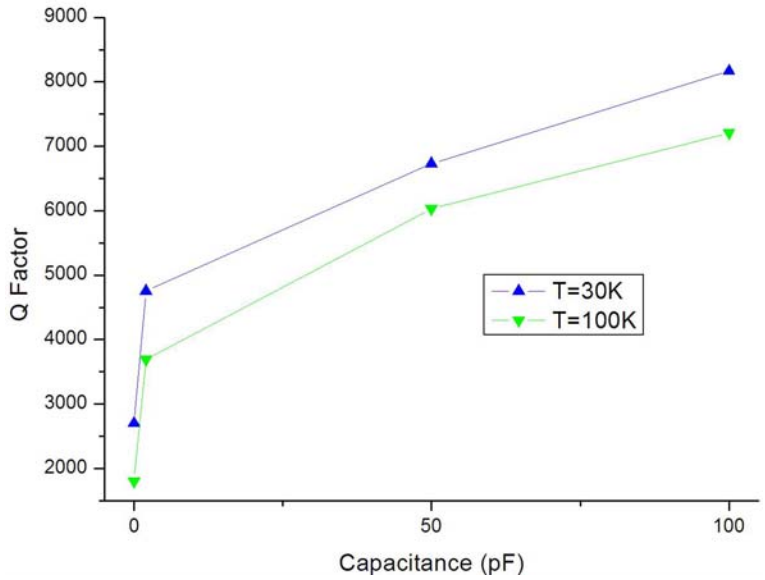

Figure 4.17: The Q factor.

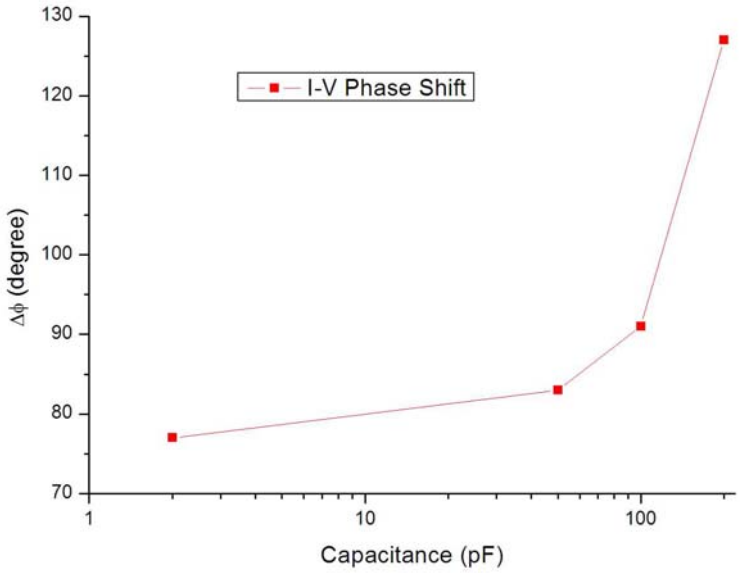

Figure 4.18: The $I - V$ phase shift.

4.4 Conclusion

We have theoretically studied the capacitance effect on microwave power spectra of spin-torque oscillators. By adding a capacitor connected in parallel with the STO, the thermal stability of the system can be improved. It is hence probable that part of the underlying reason for the high quality factors observed in experiments may be ascribed to either intrinsic or extrinsic sources of capacitance in parallel with the STO. The calculated result of $I - V$ phase shift under different conditions suggests that there may be an optimum capacitance for enhancing the thermal stability of the system. This capacitance effect will impact any circuit design based on the present STO technology and will have direct consequences

for, e.g., achieving higher output power and narrower linewidths in STO networks that is required for practical GHz communications applications.

Chapter 5

Path-Independent Capacitive Tuning Effect on Frequency Shifts

It has been demonstrated in the previous chapter that an additional capacitance connected in parallel with an STO may lead to an anomalous shift in the oscillation frequencies of the system which is of practical potential in wireless communications applications. In fact, it has been also experimentally demonstrated that this non-linear frequency shift for an STO can be varied by changing the orientation and magnitude of the external magnetic field or the applied current (Kiselev et al., 2003; Sankey et al., 2005). In this chapter, we will show that the capacitance effect also plays an important role in the frequency tuning.

5.1 Theoretical Consideration and Numerical Calculation

The system configuration adopted in this chapter is the same as the one previously considered in Chapter 4. An STO consisting of a thick magnetic 'fixed' layer, nonmagnetic spacer layer (metal for GMR based STO; dielectric for the MTJ case) and a thin 'free' layer is connected in parallel with a capacitance, and an ideal *dc* source I_{dc} is applied (see Fig. (5.1)).

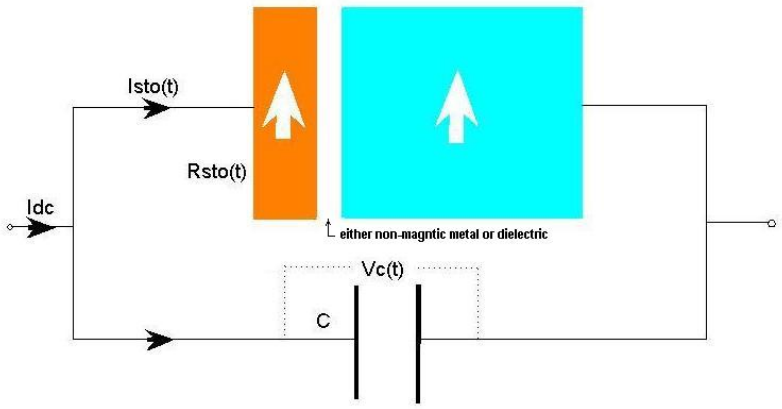

Figure 5.1: Sketch of an STO connected in parallel with a capacitance.

The time-evolution of the free layer magnetization is determined by the Landau-Lifshitz-Gilbert (LLG) equation

$$\frac{d\hat{\boldsymbol{m}}}{dt} = -\gamma\hat{\boldsymbol{m}} \times [\boldsymbol{H}_{eff} + \boldsymbol{H}_T] + \alpha\hat{\boldsymbol{m}} \times \frac{d\hat{\boldsymbol{m}}}{dt}$$
$$+\gamma\alpha_J[\hat{\boldsymbol{m}} \times (\hat{\boldsymbol{m}} \times \boldsymbol{M}) - \beta\hat{\boldsymbol{m}} \times \boldsymbol{M}] \quad (5.1)$$

where $\hat{\boldsymbol{m}}$ is the unit vector of the 'free' layer magnetization of the STO, γ is

the gyromagnetic ratio, and α is the Gilbert damping parameter. $\boldsymbol{H}_{eff}$ is the effective magnetic field acting on the 'free' layer, which consists of the contribution of the uniaxial magnetic anisotropy field $\boldsymbol{H}_k$, the demagnetization field $\boldsymbol{H}_d$ and an external 'in-plane' applied magnetic field $\boldsymbol{H}_{app}$. The stochastic magnetic field vector $\boldsymbol{H}_T$ is used to represent the effect of finite temperature, and each spatial component of it is chosen at random from a normal distribution. The last term in Eq. 5.1 stands for the spin-transfer torque effect arising from the absorption of the spin current component which is transverse to the magnetization of the 'free' layer. We take into account both the parallel and perpendicular components of the spin-transfer torque acting on the 'free' layer.

The transverse spin current component is almost completely absorbed by the ferromagnetic film within a very short distance of the interface (usually a few lattice constant) (Gmitra et al., 2006; Stiles and Zangwill, 2002). Therefore, the corresponding spin-torque $\boldsymbol{\tau}$ per unit volume, acting on the 'free' layer, can be calculated as (Stiles and Zangwill, 2002)

$$\boldsymbol{\tau} = \frac{\hbar}{2}\boldsymbol{j}_{\perp} \tag{5.2}$$

where $\boldsymbol{j}_{\perp}$ is normal to the magnetization component of the spin current at the interface between the nonmagnetic spacer and 'free' layers. The 'in-plane' component $\boldsymbol{\tau}_{\parallel}$ of the torque can be expressed as $\boldsymbol{\tau}_{\parallel} = -a\hat{\boldsymbol{m}} \times (\hat{\boldsymbol{m}} \times \boldsymbol{M})$. Consequently, the 'out-of-plane' component $\boldsymbol{\tau}_{\perp}$ of the torque can be generally expressed

as $\boldsymbol{\tau}_{\perp} = b\hat{\boldsymbol{m}} \times \boldsymbol{M}$ (Gmitra et al., 2006). By taking into account the geometry of the trilayer structure shown in the Fig. (5.2), one can write (Gmitra et al., 2006)

$$\boldsymbol{\tau}_{\parallel} = -\boldsymbol{e}_{\parallel}\frac{\hbar}{2}(j_x \cos\theta\cos\varphi + j_y \cos\theta \sin\varphi - j_z \sin\theta) \tag{5.3}$$

$$\boldsymbol{\tau}_{\perp} = -\boldsymbol{e}_{\perp}\frac{\hbar}{2}(j_x \sin\varphi - j_y \cos\varphi) \tag{5.4}$$

where $\boldsymbol{e}_{\parallel} = \hat{\boldsymbol{m}} \times (\hat{\boldsymbol{m}} \times \boldsymbol{M})$ and $\boldsymbol{e}_{\perp} = \hat{\boldsymbol{m}} \times \boldsymbol{M}$, respectively, and the spin current components are calculated in the nonmagnetic spacer at the interface with the 'free' layer (Gmitra et al., 2006).

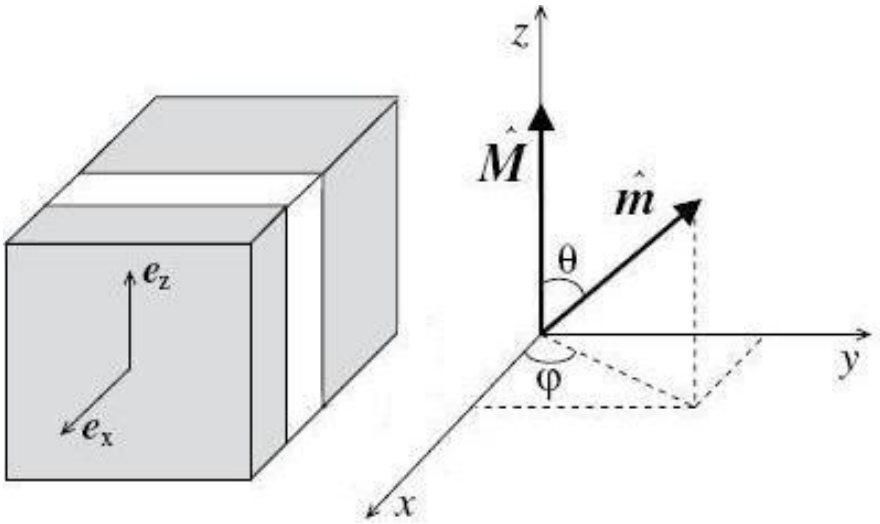

Figure 5.2: Schematic structure of the STO. The angles θ and φ describe the orientation of the magnetization $\hat{\boldsymbol{m}}$ (Gmitra et al., 2006).

The parameter $\beta = a/b$ depends on the applied current I_{dc}. Since the 'out-of-plane' component $\boldsymbol{\tau}_{\perp}$ is usually much smaller than the 'in-plane' component $\boldsymbol{\tau}_{\parallel}$, e.g., $\beta \approx 0.01$ in GMR based spin valve geometries, the effect of perpendicular

torque is usually neglected in the calculations for the sake of simplicity. But in MTJ devices, it has been interpreted as demonstrating that $\beta \approx 0.25$ (Zimmler et al., 2004), then this kind of contribution is of critical importance in the magnetization dynamics.

The perpendicular spin torque in MTJ was recently studied experimentally by measuring the critical switching current at different magnetic fields, and the direction of the torque was found to be able to reverse as the polarity of the biased voltage changed (Li et al., 2008). This result is contradictory to the previous observation, and the mechanism responsible for this phenomenon is still yet to be explained by existing theory. In order to get a comprehensive qualitative analysis of the capacitive effect on MTJ devices, we adopt both signs for the parameter β (called 'opposite sign' when β is positive, and 'same sign' when β is negative).

The presence of capacitance will only allow an alternating current to flow through without shunting the total direct current I_{dc} from the STO branch. Considering the continuity of the total *dc* current and equal voltage drop across the two parallel branches, we have the following equations

$$R_{STO}(t) = \frac{R_{AP} + R_P}{2} - \frac{R_{AP} - R_P}{2} \cos\theta(t) \tag{5.5}$$

$$I_{STO}(t) + \frac{C dV_C(t)}{dt} = I_{dc} \tag{5.6}$$

$$V_C(t) = I_{STO}(t) R_{STO}(t) \tag{5.7}$$

where R_{AP} and R_P are the antiparallel and the parallel resistance of the STO respectively, $\theta(t)$ is the angle between the magnetization of the 'fixed' layer and that of the 'free' layer, $V_C(t)$ is the instantaneous voltage across the capacitance, and $I_{STO}(t)$ is the instantaneous current flowing through the STO branch, as shown in Fig. (5.1).

Then, following the same manipulation as in the previous chapter, Eq. 5.5, Eq. 5.6 and Eq. 5.7 yield

$$\frac{dI_{STO}}{dt} = \frac{I_{dc} - I_{STO}(t) - CI_{STO}(t) \cdot dR_{STO}(t)/dt}{CR_{STO}(t)} \tag{5.8}$$

The magnetization dynamics of the system is given by the solution of Eq. 5.1 and Eq. 5.8, which can be numerically solved by using a fourth-order Runge-Kutta algorithm.

5.2 Results and Discussion

To simulate typical GMR based trilayer spin valve and MTJ devices, the following primary parameters are adopted: $\alpha = 0.008$, $\gamma = 1.85 \times 10^{11}$ Hz/T, $\eta = 0.35$, $H_{app} = 0.2$ T, $H_d = 4\pi M_s = 1.6$ T, $H_k = 0.1$ T, $R_P = 15.8\ \Omega$, $R_{AP} = 23.4\ \Omega$, and parameter β is set as a constant value of ± 0.25 for the MTJ type devices and 0 for GMR based spin valve.

5.2.1 Capacitance Effect on the Oscillation Frequency with Thermal Fluctuation

It has been already experimentally demonstrated (Mistral et al., 2006) that the oscillation frequency will decrease with increasing temperature (Fig. (5.3)).

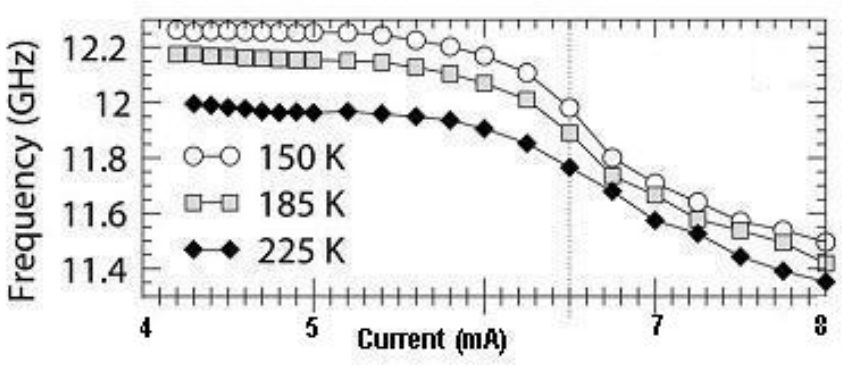

Figure 5.3: Frequency vs applied current under different temperatures (Mistral et al., 2006).

This kind of phenomenon has also been observed in our calculations. Fig. (5.4) shows the results of the oscillation frequency as a function of operating temperature. Although the decline in the frequency is not as significant as that measured in the experiment, similar trends have been obtained under different applied currents.

When the capacitance is connected in parallel with the STO, the oscillation frequency of the system no longer changes with the varying temperature. Fig. (5.5) shows typical simulation results of the fitted oscillation frequencies with different capacitances incorporated in the circuit. It is obvious that once the

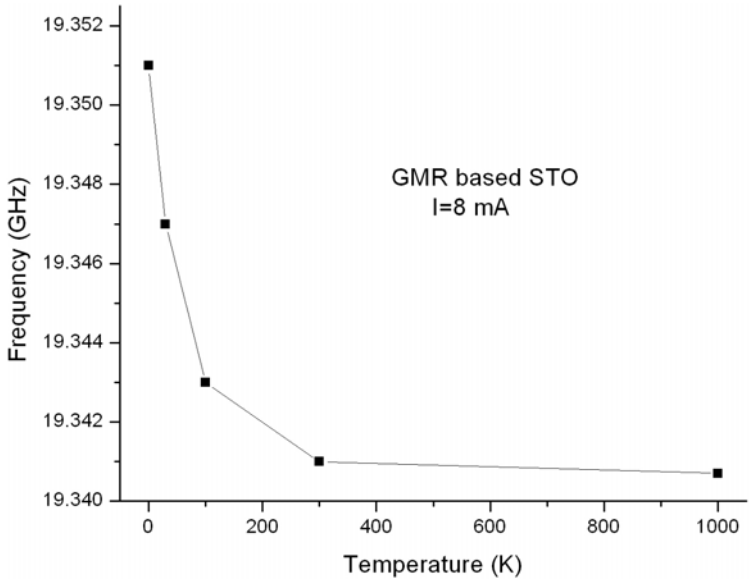

Figure 5.4: Frequencies as a function of temperature at $I = 8$ mA.

additional capacitance is connected in parallel with the STO, the frequencies of the steady oscillation are exactly the same under different operation temperatures.

This is not unexpected. A possible factor that may contribute to this capacitance effect on frequency shift with thermal fluctuation is the competition between these two external influences on the magnetization dynamics. With the additional capacitance in the circuit, it introduces an *ac* current in the STO branch and causes fluctuations in the precessional dynamics. The effect of thermal noise is taken into account by incorporating the fluctuation field H_T into the effective field H_{eff} in the modified LLG equation, and this will also have the same influence on the magnetization precessional orbits of Fig. (4.15) shown in

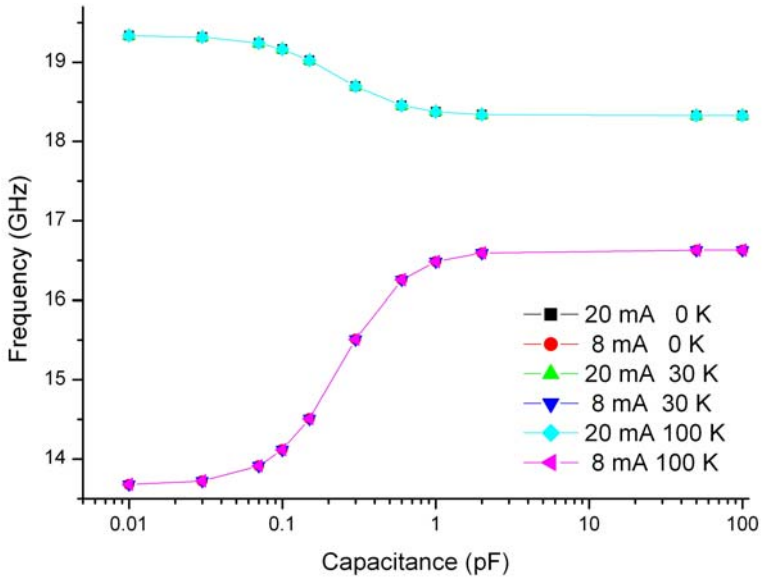

Figure 5.5: Oscillation frequencies of a GMR based STO incorporated with different capacitance under different temperatures.

the previous chapter. The thermal energy, however, is of the order of $k_\beta T/2$. Compared with the instantaneous energy $\frac{1}{2}CV_C(t)^2$ stored in the capacitance, the effect of thermal fluctuation on the precessional dynamics is so limited that it can be considered as a perturbation. But with a small capacitance, e.g. 0.01 pF, in the circuit, and the operation temperature is extremely high say 1,000 K, for which the thermal energy is comparable with the instantaneous energy of the capacitance, the influence of the thermal fluctuation starts to emerge.

It is also interesting to note that the oscillation frequency, at certain applied *dc* current, will increase or decrease significantly with varying capacitance; this will be discussed in the following section.

5.2.2 Capacitive Tuning Effect on the Oscillation Frequency

As it has been confirmed in our calculations that the effect of thermal fluctuation on nonlinear frequency shift will be eliminated with the appearance of the additional capacitance in the circuit, we will only describe the computational results obtained under the operation temperature at 0 K.

Fig. (5.6) shows how the intrinsic oscillation frequency of the GMR based spin valve and MTJ type device depends on the applied *dc* current without the additional capacitance connected in parallel with the STO. As I_{dc} increases, the oscillation frequency for the three types of STO decreases, and the precession mode is 'in-plane' (IP). The opposite trend can be observed for the onset of 'out-of-plane' (OOP) precession.

We now connect the capacitance into the calculation. As shown in Figs. (5.7)-(5.9), the oscillation frequencies can be tuned by varying the capacitance.

When the I_{dc} is 8 or 10 mA, the precessional mode is IP and an increase in capacitance would bring about a decrease in oscillation frequency for the GMR configuration, as shown in Fig. (5.7).

With yet larger I_{dc}, i.e., 15, 17, and 20 mA, the precessional mode transfers from IP to OOP. By increasing the capacitance, the frequency increases for the GMR configuration (see Fig. (5.8)).

When the *dc* current is just below the IP/OOP critical region, where only

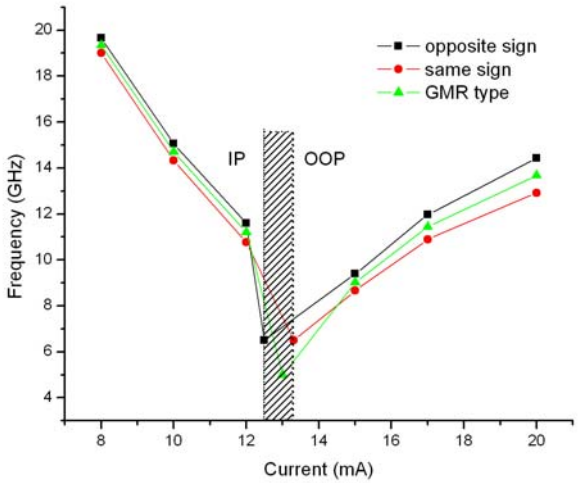

Figure 5.6: STO oscillation frequency as a function of I_{dc}.

IP precessional mode is expected, it is found that the mode can be switched to OOP with increasing capacitance, and versa vice (see Fig. (5.9)). This is quite an unexpected result, since the precessional mode should be determined by the applied dc current initially, and would not be affected by other external factors.

Another issue that deserves careful attention is that the frequency does not vary monotonically with capacitance for MTJ type device. Fig. (5.10)) shows how the oscillation frequency depends on the capacitance for MTJ based cases, and the peak/trough can be observed at certain capacitance, which is quite an unexpected result as well.

The result of $I - V$ phase shift, i.e. phase difference between the ac current and the voltage across the STO branch is also given in Fig. (5.11). By comparing

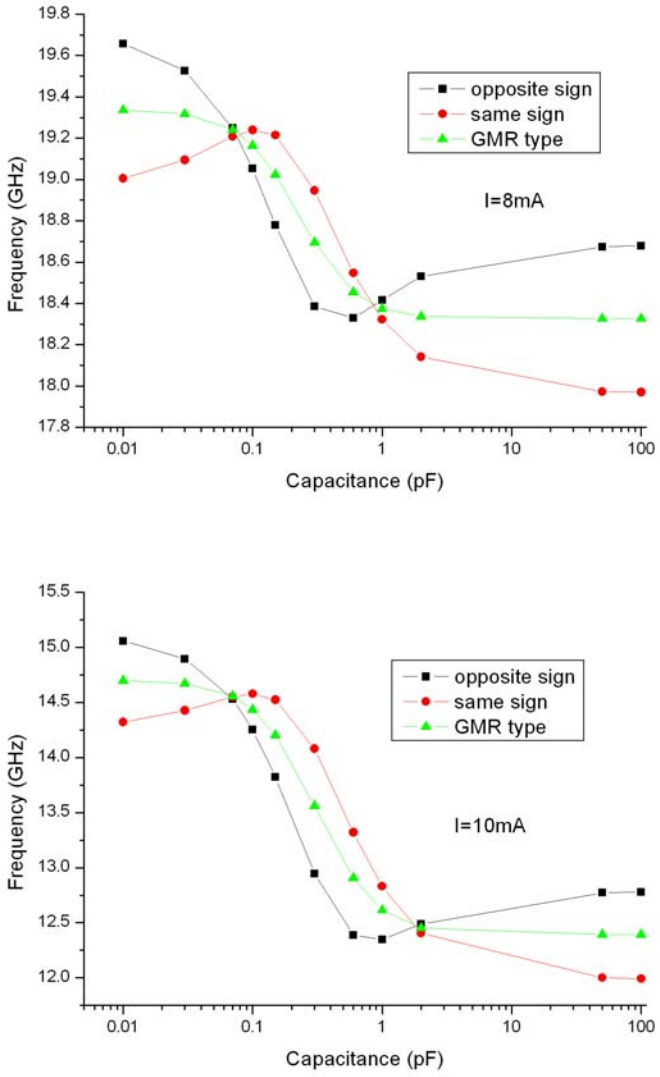

Figure 5.7: Capacitive tuning effect on oscillation frequencies at 8 and 10 mA.

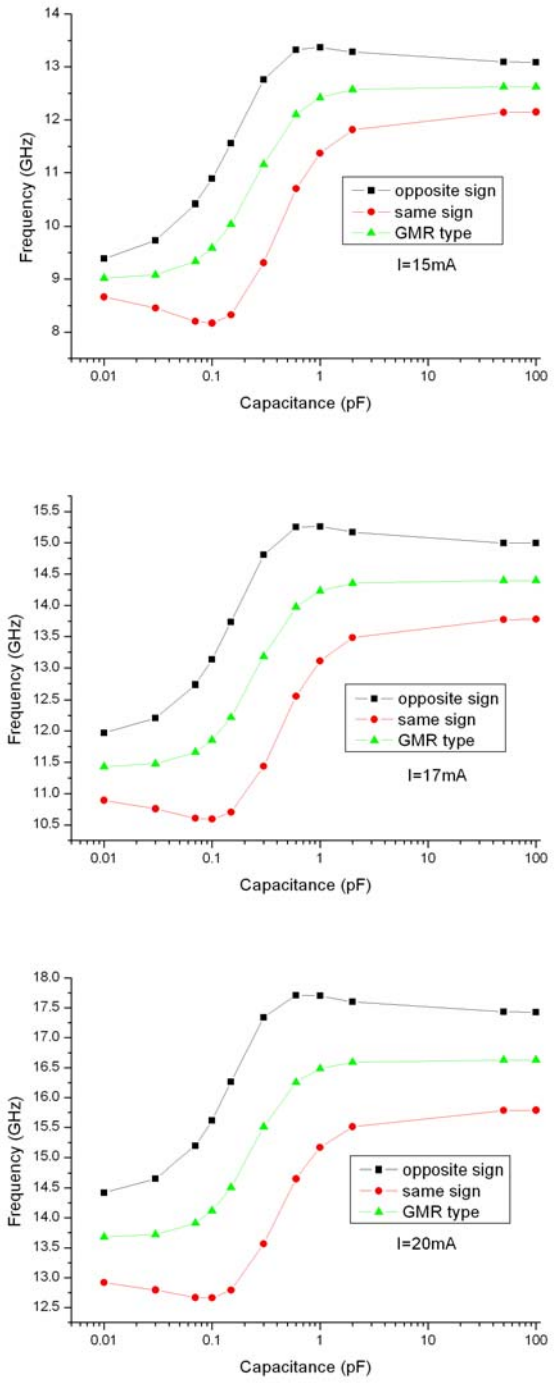

Figure 5.8: Capacitive tuning effect on oscillation frequencies at 15, 17, and 20 mA.

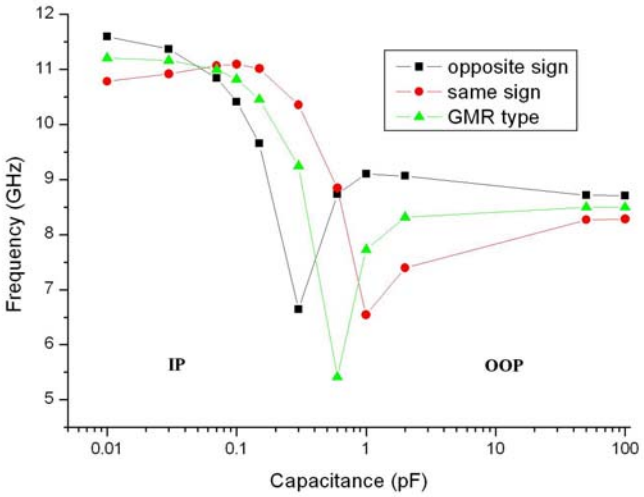

Figure 5.9: Capacitive tuning effect on oscillation frequencies at 12 mA.

the $I - V$ phase shit, we can find that there is not much of a difference between the three types when the capacitance is above a certain value at which point the preferred phase shift is around 90 degrees. Fig. (5.12) shows that when the capacitance is around 0.7 pF, anti-phase locking can be observed.

5.2.3 Path-independent Capacitive Tuning Effect

In the previous calculation, the additional capacitance has been connected in the circuit at the very beginning, as shown in Fig. (5.13), and we have found the capacitance tuning effect on frequency shifts of the STO system.

Now, the bias current I_{dc} is fixed and the capacitance is changed during the process of the calculation. In other words, the value of capacitance has been

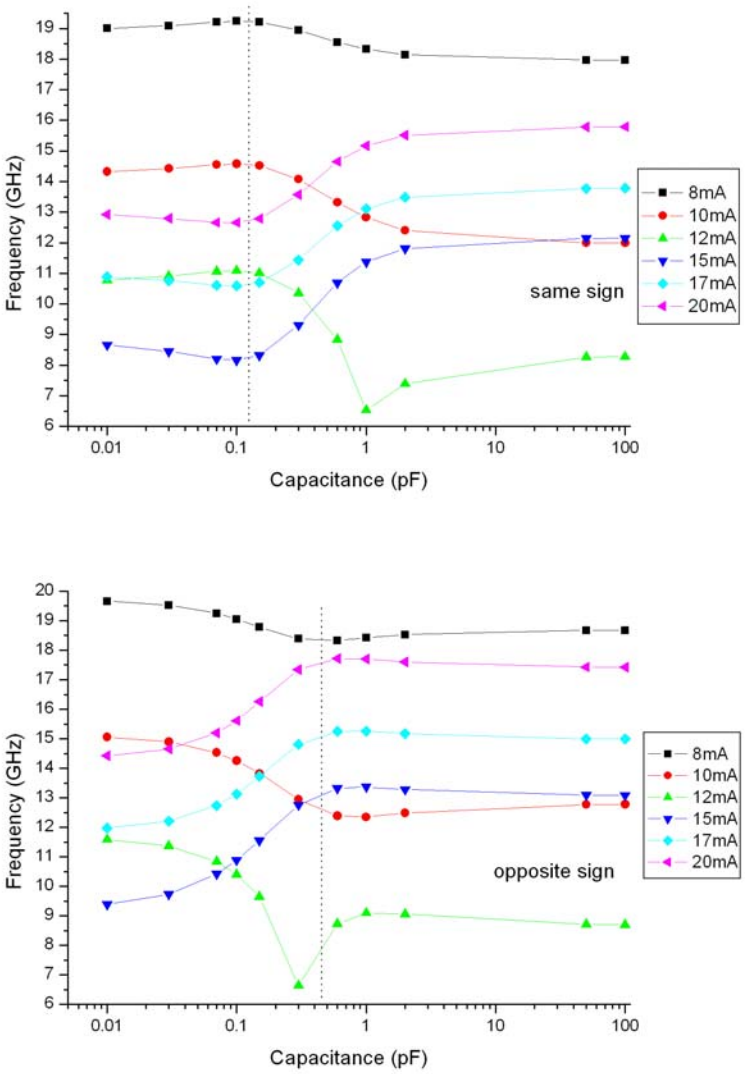

Figure 5.10: Capacitive tuning effect on oscillation frequencies for MTJ based devices.

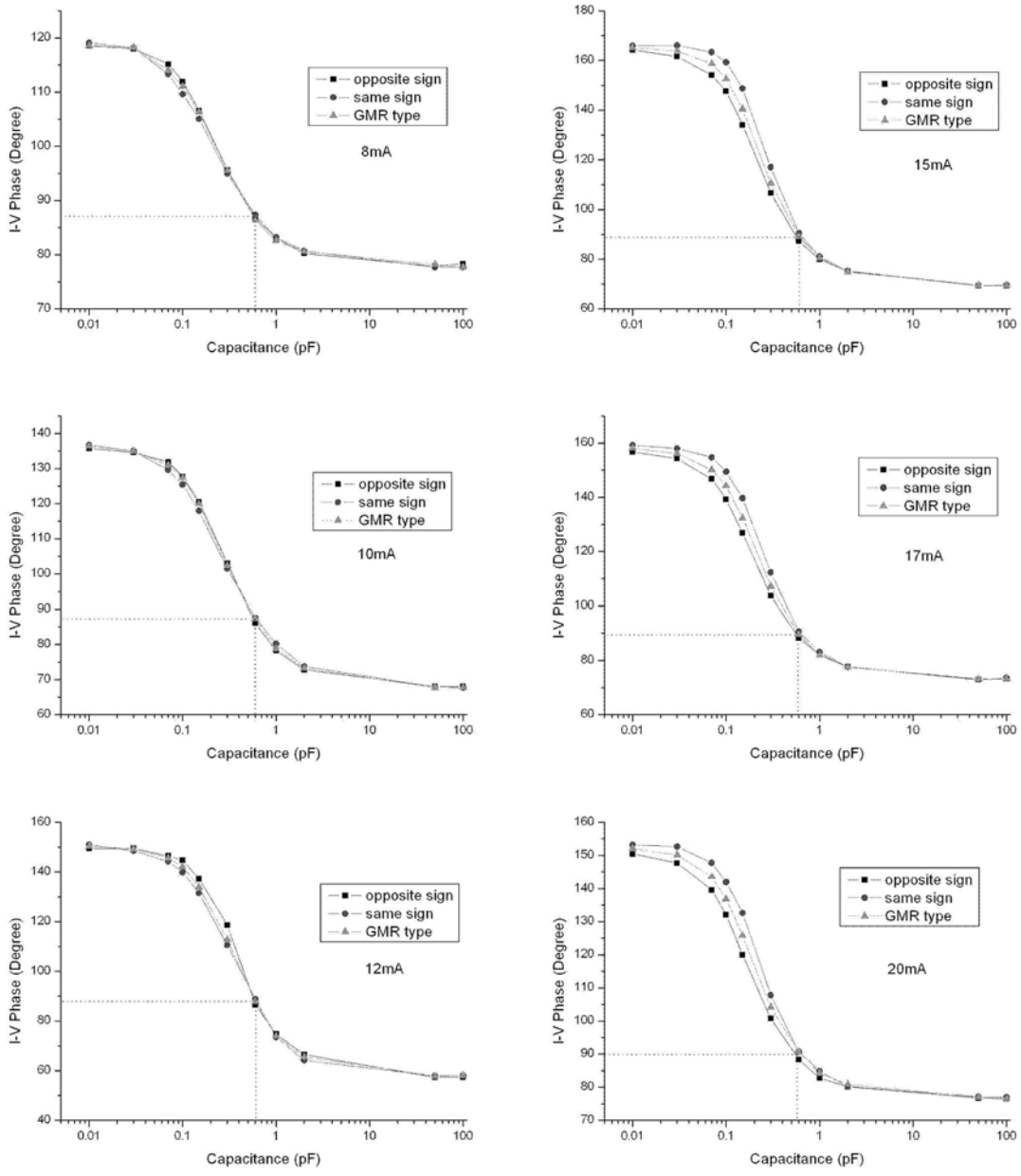

Figure 5.11: The $I-V$ phase shift.

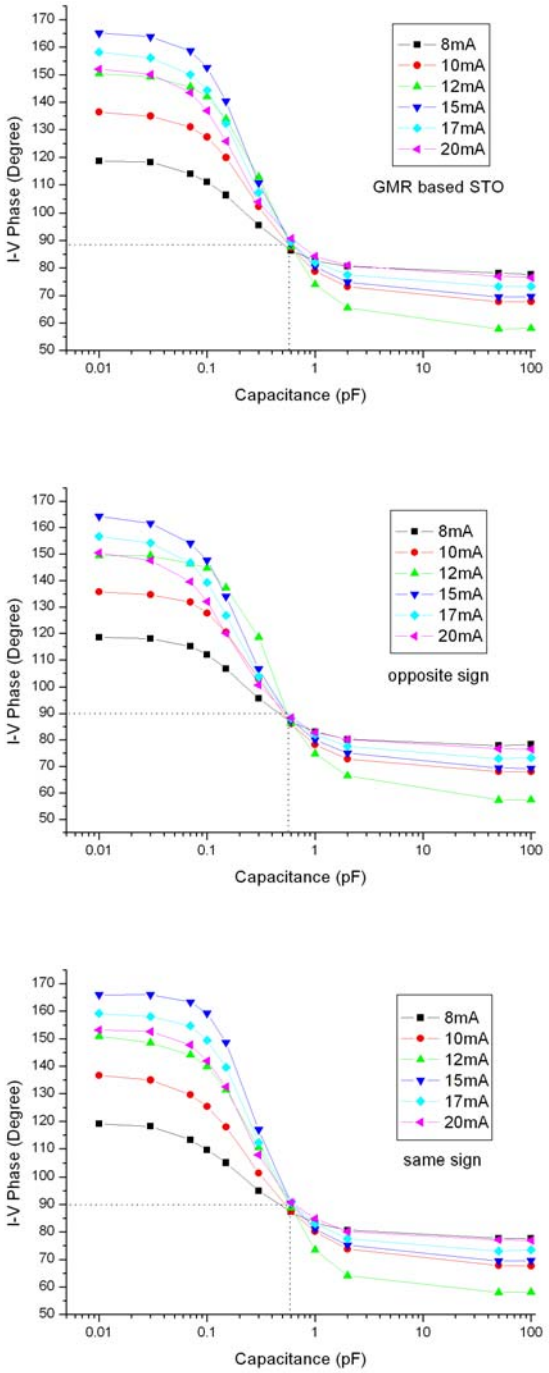

Figure 5.12: The $I-V$ phase shift.

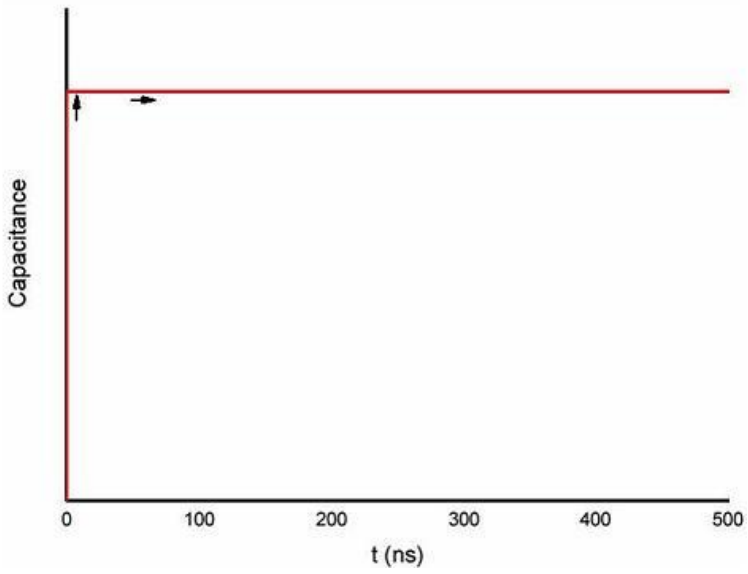

Figure 5.13: The appearance of the capacitance in the circuit as a function of operation time.

turned up and down while the STO is operating. The capacitance was changed at different time-steps, and each time interval is long enough (20-50 ns) to ensure the oscillation can reach the steady state as shown in Fig. (5.14). When the oscillation becomes steady at each step, the frequency is consistent with the result obtained in the first calculation.

Furthermore, even in the case the capacitance is changed smoothly with the time (see Fig. (5.15)), once the the capacitance stops varying the precessional oscillation will eventually become steady and the frequency still is exactly the same as in the first calculation in the previous section.

Confirmed by many times of simulation, it is safe to conclude that the capac-

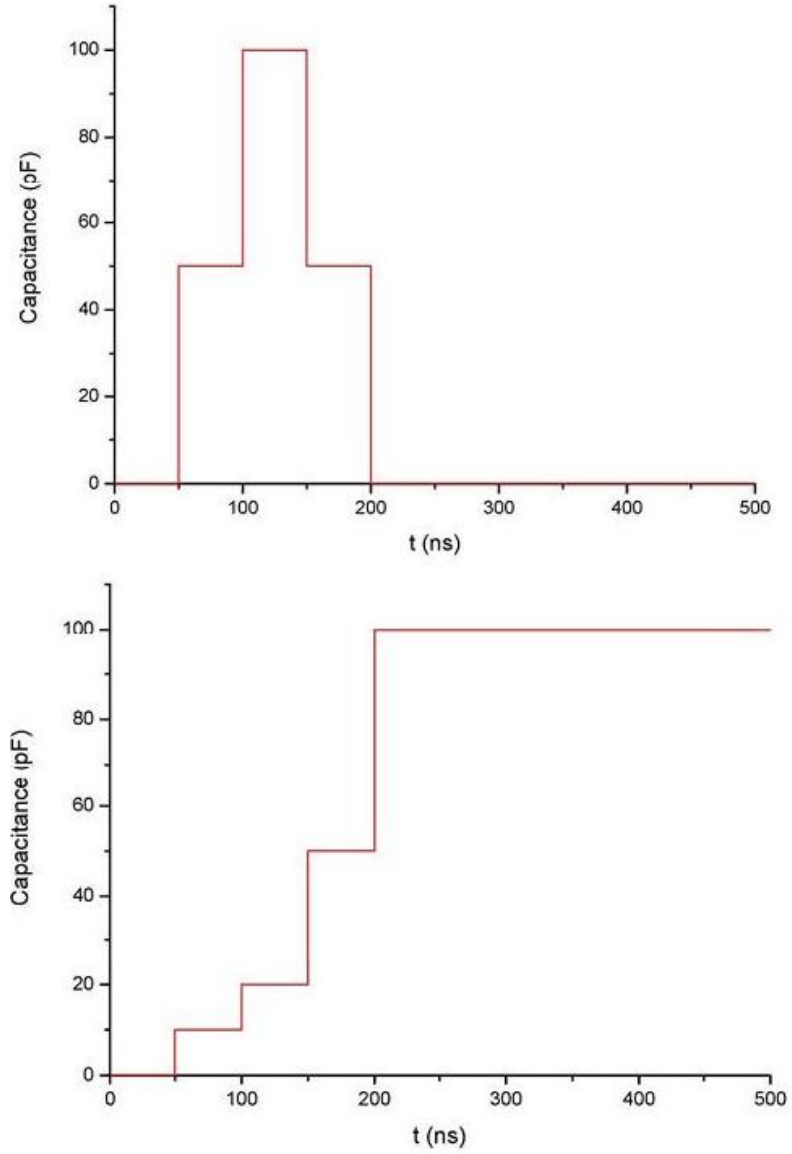

Figure 5.14: The capacitance is tuned at each time interval.

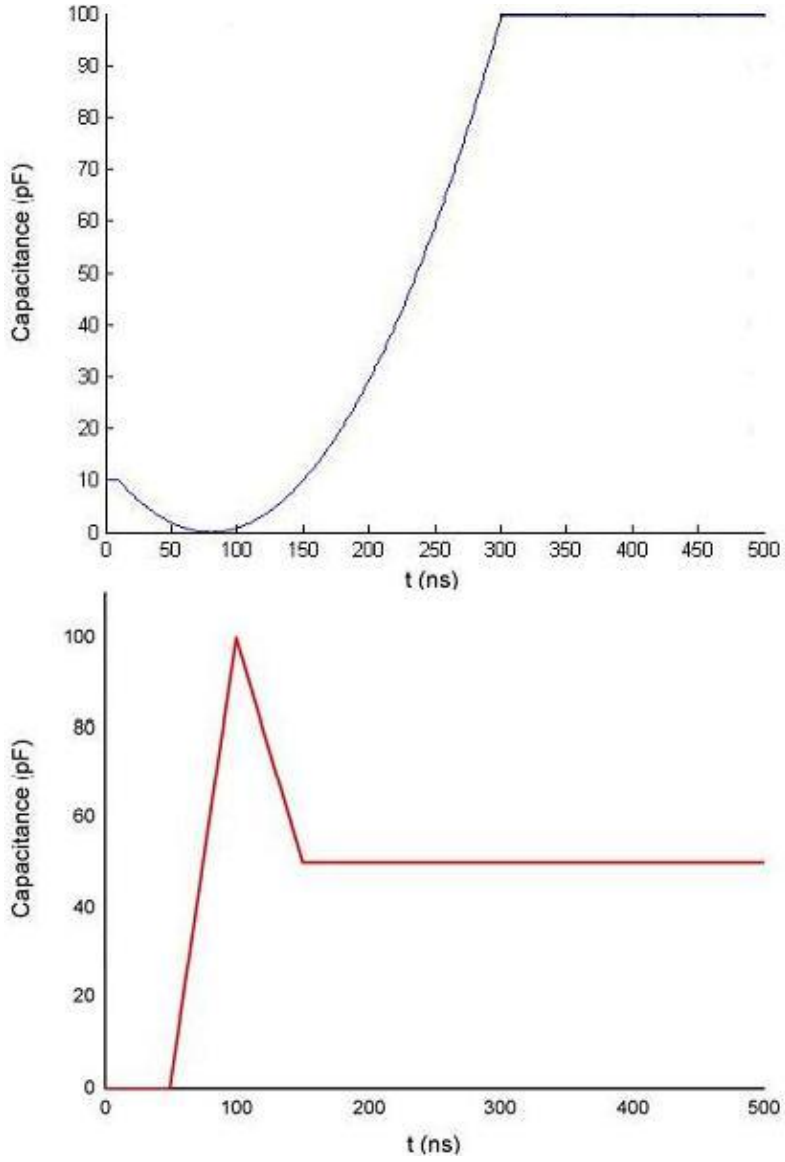

Figure 5.15: The capacitance is changed smoothly with time.

itive tuning effect on frequency shifts of STO is 'path-independent'. In our case, the oscillation frequency of the system is determined just by the applied current I_{dc} and the additional capacitance C.

5.2.4 Non-linear Theory of Microwave Generation

In order to interpret the nonlinear frequency shift in the STO, an analytic theory has been developed by Slavin to study the current-induced microwave generation in the magnetic nano-structure (Kim et al., 2008).

As has been pointed out by Slavin in his unpublished manuscript (presented in INTERMAG Conference 2008) that spin-torque oscillator can be seen as an auto-oscillatory system. Moreover, Slavin also presents the explicit interpretation of the forced dynamics of the oscillation due to an external signal which is described in the model by expressing the 'deriving term' $f(t) = f_e e^{-i\omega_e t}$ to represent an external harmonic signal:

$$\frac{dc}{dt} + i\omega(|c|^2)c + \Gamma_+(|c|^2)c - \Gamma_-(|c|^2)c = f_e e^{-i\omega_e t} \tag{5.9}$$

where $c(t)$ is the complex amplitude of the auto-oscillations, which indicates both the power $p = |c|^2$ and the phase $\phi = arg(c)$ of the oscillations; $\omega(p)$ is the resonance frequency of the 'resonant element'; $\Gamma_+(p)$ is the damping rate for the energy dissipative process; $\Gamma_-(p)$ is the 'negative' damping rate which describes the effective action of the external or internal energy source (Kim et al., 2008). In

general, the resonance frequency $\omega(p)$ and both damping rates $\Gamma_{\pm}(p)$ are functions of the auto-oscillation power $p = |c|^2$, which makes the auto-oscillatory system a nonlinear system. f_e and ω_e are, respectively, the complex amplitude and frequency of the external signal.

In our case, as the frequency of the *ac* current induced by the additional capacitance is consistent with the oscillation frequency of the STO, therefore ω_e is $\omega(p)$. Then, it is more convenient to express the equation as two real equations for the power $p = |c|^2$ and phase $\phi = arg(c)$ of the oscillations

$$\frac{dp}{dt} + 2[\Gamma_+(p) - \Gamma_-(p)]p = 2|f_e|\sqrt{p}\cos\omega_e t + \phi - \psi_e \tag{5.10}$$

$$\frac{d\phi}{dt} + \omega(p) = -\frac{|f_e|}{\sqrt{p}}\sin\omega_e t + \phi - \psi_e \tag{5.11}$$

where $|f_e|$ is the real amplitude and $\psi_e = arg(f_e)$ is the initial phase of the external 'driving' force.

Since $\omega(p) \neq const$ for the nonlinear oscillation, it is necessary to consider the above two equations at the same time for the power p and phase ϕ of the oscillation. In the limit of a weak external signal $|f_e| \to 0$, as pointed by Slavin, it is possible to expand these equations in a Taylor series by treating the 'driving' force amplitude $|f_e|$ and the power deviation $\delta p = p - p_0 \approx |f_e|$ as small parameters. In the first order on these parameters, the following can be obtained:

$$\frac{d\delta p}{dt} + 2\Gamma_p\delta p = 2|f_e|\sqrt{p_0}\cos\omega_e t + \phi - \psi_e \tag{5.12}$$

$$\frac{d\phi}{dt} + \omega_g = -\frac{|f_e|}{\sqrt{p_0}} \sin \omega_e t + \phi - \psi_e - N\delta p \tag{5.13}$$

In the equations above, there is an additional 'forcing' term $-N\delta p$, which, according to Slavin, can be substantially more important than the 'driving' term proportional to the amplitude $|f_e|$. As it has been indicated in Chapter 4, the appearance of an additional capacitance will affect the oscillation power in a nontrivial way, and a small change in the oscillation power δp may result in matching of the nonlinear eigen-frequency $\omega(p) \approx \omega_g + N\delta p$ of the oscillation to the frequency of the external *ac* current induced by the additional capacitance in the circuit. Applying this analytical consideration to our calculated results, we can qualitatively understand how the effect of capacitance influences the nonlinear frequency shift of STO. However, the mechanism of the IP/OOP transfer at $I_{dc} = 12$ mA is still lacking of a sound explanation.

5.3 Conclusion

We studied the capacitive tuning effect on oscillation frequencies. It is found that the oscillation frequency only varies with the value of capacitance, and will not change much with temperature in both GMR and MTJ based situations. The precessional mode is determined by the applied *dc* current and the oscillation frequencies can be tuned by varying the capacitance. For the 'in-plane' (IP) precessional mode, an increase in capacitance would bring about a decrease in

oscillation frequency for the GMR configuration; for the 'out-of-plane' (OOP) mode, the frequency shifts in the opposite way. For MTJ, the frequency does not vary monotonically with capacitance, which is quite an unexpected result. When the *dc* current is just below the IP/OOP critical region, where only IP precessional mode is expected, it is found that the mode can be switched to OOP with increasing capacitance. An analytical theory has been borrowed to try to explain the mechanism of nonlinear frequency shifts.

Chapter 6

Conclusion

6.1 Summary of Thesis

This thesis describes the theoretical study and numerical simulation of the capacitance effect on spin-torque oscillators with thermal fluctuation based on typical giant magneto-resistance (GMR) trilayer spin valve system and magnetic tunneling junction (MTJ) structure.

In our macrospin model, typical trilayer spin valve device structures have been adopted, with one 'fixed' and one 'free' ferromagnetic layer separated by a nonmagnetic spacer. The dynamics of the 'free' layer magnetization is determined by the Landau-Lifshitz-Gilbert-Slonczewski (LLGS) equation. To study the temperature effects on spin torque behavior, we model the thermal fluctuations by adding a Langevin random field to the effective field in the LLGS equation.

The capacitance effect on the microwave power spectra of an STO was initially investigated with thermal fluctuation. In the presence of thermal noise,

the microwave power spectrum gets broadened with increasing temperature. By adding a capacitance connected in parallel with the STO, the thermal stability of the system can be improved. It is hence probable that part of the underlying reason for the high quality factors observed in experiments may be ascribed to either intrinsic or extrinsic sources of capacitance in parallel with the STO. The calculated result of $I - V$ phase shift under different conditions suggests that there may be an optimum capacitance for enhancing the thermal stability of the STO system.

Apart from the thermal stability, we studied the capacitive tuning effect on oscillation frequencies. The LLGS equation has been developed to simulate the dynamics of precessional modes in the case of MTJ by adding a perpendicular term to the Slonczewski 'in-plane' spin-torque term. It is found that the oscillation frequency only varies with the value of capacitance, and will not change much with temperature in both GMR and MTJ based situations. The precessional mode is determined by the applied *dc* current and the oscillation frequencies can be tuned by varying the capacitance. For the 'in-plane' (IP) precessional mode, an increase in capacitance would bring about a decrease in oscillation frequency for the GMR configuration; for the 'out-of-plane' (OOP) mode, the frequency shifts in the opposite way. For MTJ, the frequency does not vary monotonically with capacitance, which is quite an unexpected result. When the *dc* current is just

below the IP/OOP critical region, where only IP precessional mode is expected, it is found that the mode can be switched to OOP with increasing capacitance.

This capacitance effect on thermal stability and frequency tuning will impact any circuit design based on the present STO technology and will have direct consequences for, e.g., achieving higher output power and narrower linewidths in tunable nano-sized oscillator networks that is required for practical GHz wireless communications applications.

6.2 Future Work

The results in this thesis lay the groundwork for a good understanding of capacitance effect on spin-torque oscillators. But it also seems to have raised more questions than it has answered. There are several lines of research arising from this work which should be pursued.

Firstly, we adopted the macrospin model in our calculations. The macrospin approximation assumes that the magnetization of the 'free' layer can be treated as a single macroscopic spin and neglects the spatial variation of the magnetization. Although macrospin approximation is most widely used in the investigation of magnetization dynamics, it breaks down for many complex systems. For a further understanding of the capacitance effect on the magnetic dynamics of STOs, a micromagnetic simulation is therefore necessary.

Secondly, in the present simulations the additional capacitance is treated as an ideal capacitor in the equivalent circuit. The impedance of the capacitance, however, is inversely proportional to the frequency, i.e. for very high frequency *ac* currents the reactance of the capacitor approaches zero. Thus, a capacitor is almost a short circuit to a very high frequency *ac* current. As the oscillation frequency of the STO system is extremely high, the form of capacitance in the calculation formula can be further developed to present its real operation situation in the high frequency region.

As for a network of STOs, an initial work of the effect of capacitance on the synchronization of a pair of serially connected STOs has been finished with Zhou (Zhou et al., 2008). By tuning the capacitance in the system, the synchronization state of the oscillators is much enhanced. However, the influence of thermal fluctuation has not been taken into account. Further investigation into the capacitance effect on the 'independent' and 'dependent' magnetic dynamics of a series of STOs with thermal noise should be undertaken.

Bibliography

Aharoni A. Introduction to the Theory of Ferromagnetism. Oxford University Press, 2000.

Akerman J.. Toward a universal memory. Science, 308:508, 2005.

Arrott A. Plenary Lecture: Progress in Micromagnetics. Moscow Internation Symposium on Magnetism, 2002.

Baibich M. N., Broto J. M., Fert A., VanDau F. N., Petroff F., Etienne P., Creuzet G., Friederich A., and Chazelas J. Giant magnetoresistance of (001)fe/(001)cr magnetic superlattices. Phys. Rev. Lett., 61:2472, 1988.

Berger L. Emission of spin waves by a magnetic multilayer traversed by a current. Phys. Rev. B, 54:9353, 1996.

Berger L. Effect of interfaces on gilbert damping and ferromagnetic resonance linewidth in magnetic multilayers. J. Appl. Phys., 90:4632, 2001.

Berkov D. and Gorn N.. Transition from the macrospin to chaotic behavior by spin-torque driven magnetization precession of a square nanoelement. Phys. Rev. B, 71:052403, 2005.

Berkov D. V. and Miltat J.. Spin-torque driven magnetization dynamics: Micromagneticmodeling. J. Magn. Magn. Mater., 320:1238, 2008.

Bertotti G, Serpico C., Mayergoyz I. D., Bonin R., Magni A., and d'Aquino M. Magnetization self-oscillations induced by spin-polarized currents. IEEE Trans. Magn., 41:2574, 2005.

Bland T., Lee K., and Steinmuller S. The spintronics challenge. http://physicsworld.com/cws/article/print/32278, 2008.

Bonin R., Bertotti G., Mayergoyz I. D., and Serpico C.. Spin-torque-driven magnetization dynamics in nanomagnets subject to magnetic fields perpendicular to the sample plane. J. Appl. Phys., 99:08G508, 2006.

Brataas A., Nazarov Y. V., and Bauer G. E. W. Finite-element theory of transport in ferromagnetcnormal metal systems. Phys. Rev. Lett., 84:2481, 2000.

Brataas A., Tarara G., and Bauer G. E. W.. Ballistic and diffuse transport through a ferromagnetic domain wall. Phys. Rev. B, 60:3406, 1999.

Brown Jr. W. F. Micromagnetics. New York: Interscience, 1963.

Bibliography

Brumfiel G. Magnetic effect sends physicists into a spin. Nature, 426:110, 2003.

Buttiker M., Imry Y., Landauer R., and Pinhas S. Generalized many-channel conductance formula with application to small rings. Phys. Rev. B, 31:6207, 1985.

Cattani C. and Rushchitsky J. Wavelet and Wave Analysis as Applied to Materials With Micro or Nanostructure. World Scientific, 2007.

Cellier F. and Kofman E. Continuous System Simulation. Springer Verlag, 2006.

Chen H. F. Atomic Physics. University of Science and Technology of China Press, 2007.

Chopra H. D. and Hua S. Z. Ballistic magnetoresistance over 3000 percent in Ni nanocontacts at room temperature. Phys. Rev. B, 66:020403, 2002.

Chtchelkanova A., Wolf S., and Idzerda Y. Magnetic intercations and spin transport. Kluwer Academic/Plenum Publishers, 2003.

Chung S. H., Munoz M., Garcia N., Egelhoff W. F., and Gomez R. D.. Universal scaling of ballistic magnetoresistance in magnetic nanocontacts. Phys. Rev. Lett., 89:287203, 2002.

Consolo G., Azzerboni B., Finocchio G., Lopez-Diaz L., and Torres L. Influence of the oersted field in the dynamics of spin-transfer microwave oscillators. J. Appl. Phys., 101:09C108, 2007.

d'Aquino M. Nonlinear Magnetization Dynamics in Thin-Film and Nano-Particles. Universita Degli Studi Di Napoli "Federico II", 2004.

Deac A. M., Fukushima A., Kubota H., Maehara H., Suzuki Y., Yuasa S., Nagamine Y., Tsunekawa K., Djayaprawira D. D., and Watanabe N. Biasdriven large power microwave emission from mgo-based tunnel magnetoresistance devices. arXiv, 0803:213, 2008.

Dorling W. On the inertia of walls between weiss domains (in german). Z. Naturforsch, 3a:373–379, 1948.

Doudin B. and Viret M. Ballistic magnetoresistance? J. Phys.: Condens. Matter, 20:083201, 2008.

Egelhoff J. W. F., Gan L., Ettedgui H., Kadmon Y., Powell C. J., Chen P. J., Shapiro A. J., Mcmichael R. D., Mallett J. J., Moffat T. P., Stiles M.D., and Svedberg E. B. Artifacts in ballistic magnetoresistance measurements. J. Appl. Phys., 95:7554, 2004.

Bibliography

Fert A., Cros V., George J. M., Grollier J., Jaffres H., Hamzic A., Vaures A., Faini G., Youseff J. B., and Gall H. L. Magnetization reversal by injection and transfer of spin: experiments and theory. J. Magn. Magn. Mater., 69:184406, 2004.

Fiederling R., Keim M., Geuscher G., Ossau W., Schmidt G., Waag A., and Molenkamp L. W. Injection and detection of a spin-polarized current in a light-emitting diode. Nature, 402:787, 1999.

Fuchs G. D., Sankey J. C., and Pribiag V. S.. Spin-torque ferromagnetic resonance measurements of damping in nanomagnets. Appl. Phys. Lett., 91:062507, 2007.

Garcia N., Munoz M., and Zhao Y. W. Magnetoresistance in excess of 200 percent in ballistic ni nanocontacts at room temperature and 100 oe. Phys. Rev. Lett., 82:2923, 1999.

Garcia N., Munoz M., Qian G. C., Roher H., Saveliev I. G., and Zhao Y. W. Ballistic magnetoresistance in a magnetic nanometer sized contact: An effective gate for spintronics. Appl. Phys. Lett., 79:4550, 2001.

Gilbert T. L.. A lagrangian formulation of the gyromagnetic equation of the magnetic field. Phys. Rev., 100:1243, 1955.

Gmitra M., Horvath D., Wawrzyniak M., and Barnas J. Current-induced spin dynamics in spin-valve structures. Phys. Stat. Sol. (b), 243:219, 2006.

Grollier J., Cros V., and Fert A. Synchronization of spin-transfer oscillators driven by stimulated microwave currents. Phys. Rev. B, 73:060409(R), 2006.

Guidugli P. P.. On dissipation mechanisms in micromagnetics. Eur. Phys. J. B, 19:417, 2001.

Guo B. L. and Ding S. J. Landau-Lifshitz Equations. Chinese Academy of Sciences, World Scientific Publishing Company, 2008.

Gurzhi R. N., Kalinenko A. N., Kopeliovich A. I., Yanovsky A. V., Bogachek E. N., and Landman U. Injection and detection of a spin-polarized current in a light-emitting diode. Journal of Superconductivity: Incorporating Novel Magnetism, 16:201, 2003.

Hillebrands B. and Ounadjela K. Spin Dynamics in Confined Magnetic Structures I. Springer, 2002.

Hirota E., Sakakima H., and Inomata K. Giant magneto-resistance devices. Springer-Verlag, 2002.

Bibliography

Hua S. Z. and Chopra H. D. Monte carlo renormalization group study of the dynamic scaling of hysteresis in the two-dimensional ising model. Phys. Rev. B, 66:060401, 2003.

Hubert A. Stray-field-free magnetization configurations. Phys. Stat. Sol., 32:519–534, 1969.

Hubert A. and Schafer R. Magnetic Domains: The Analysis of Magnetic Microstructures. Springer, 1998.

Iacocca E. Spin torque oscillator phase locking to a noisy alternating current. IEEE Intermag 2008, 2008.

Imai H., Sushko Y. V., Kubo Y., and Shimakawa Y. Carrier density change in the colossal-magnetoresistance pyrochlore . Phys. Rev. B, 62:18, 2000.

Ingvarsson S., Ritchie L., Liu X. Y., Xiao G., Slonczewski J. C., Trouilloud P. L., and Koch R. H. Role of electron scattering in the magnetization relaxation of thin ni81fe19 films. Phys. Rev. B, 66:214416, 2002.

Ji Y., Chien C. L., and Stiles M. D. Current-induced spin-wave excitations in a single ferromagntic layer. Phys. Rev. Lett., 90:106601, 2003.

Jin S., Tiefel T. H., and McCormack M. Thousandfold change in resistivity in magnetoresistive la-ca-mn-o films. Science, 246:413, 1994.

Julliere M. Tunneling between ferromagnetic films. Phys. Lett., 54A:225, 1975.

Kaka S., Pufall M. R., Rippard W. H., Silva T. J., Russek S. E., and Katine J. A. Mutual phase-locking of microwave spin torque nano-oscillators. Nature, 437:389, 2005.

Katine J. A., Albert F. J., Buhrman R. A., Myers E. B., and Ralph D. C. Current-driven magnetization reversal and spin-wave excitations in Co/Cu/Co pillars. Phys. Rev. Lett., 84:3149, 2000.

Kikuchi R. On the minimum of magnetization reversal time. J. Appl. Phys., 27:1352, 1956.

Kim T. H., Uehara M., and Cheong S. W.. Large room-temperature intergrain magnetoresistance in double perovskite. Appl. Phys. Lett., 74:1737, 1999.

Kim J. V., Tiberkevich V., and Slavin A. N.. Generation linewidth of an autooscillator with a nonlinear frequency shift: Spin-torque nano-oscillator. Phys. Rev. Lett., 100:017207, 2008.

Bibliography

Kiselev S. I., Sankey J. C., Krivorotov I. N., Emley N. C., Schoelkopf R. J., Buhrman R. A., and Ralph D. C. Microwave oscillations of a nanomagnet driven by a spin-polarized current. Nature, 425:380, 2003.

Krivorotov I. N., Emley N. C., Sankey J. C., Kiselev S. I., Ralph D. C., and Buhrman R. A.. Time-domain measurements of nanomagnet dynamics driven by spin-transfer torques. Science, 307:228, 2005.

LaBonte A. E. Two-dimensional bloch- type domain walls in ferromagnetic films. J. Appl. Phys., 40:2450–2458, 1969.

Landau L. D. and Lifshitz E. M.. On the theory of magnetic permeability dispersion in ferromagnetic solids (in russian). Phys. J., 8:153, 1935.

Lee K. J., Deac A., Redon O., Nozieres J. P., and Dieny B.. Excitations of incoherent spin-wave due to spin-transfer torque. Nature Mater., 3:877, 2004.

Lee Y. M., Hayakawa J., Ikeda S., Matsukura F., and Ohno H. Effect of electrode composition on the tunnel magnetoresistance of pseudo-spin-valve magnetictunnel junction with a mgo tunnel barrier. Appl. Phys. Lett., 90:212507, 2007.

Lenz K., Tolinski T., Lindner J., Kosubek E., and Baberschke K. Evidence of spin-pumping effect in the ferromagnetic resonance of coupled trilayers. Phys. Rev. B, 69:144422, 2004.

Li Z., Zhang S., Diao Z., Ding Y., Tang X., Apalkov D. M., Yang Z., Kawabata K., and Huai Y. Perpendicular spin torque in magnetic tunnel junctions. Phys. Rev. Lett., 100:246602, 2008.

Maekawa S. and Shinjo T. Spin dependent transport in magnetic nanostructures. Taylor and Francis, 2002.

Mallinson J. On damped gyromagnetic precession. IEEE Trans. Magn., 23:4, 1987.

Mallinson J.C. Magneto-resistive and spin valve heads : fundamentals and applications. Academic Press, 2002.

Mancoff F. B., Rizzo N. D., Engel B. N., and Tehrani S. Phase-locking in doublepoint-contact spin-transfer devices. Nature, 437:393, 2005.

McGuire T. R. and Potter R. I. Anisotropic magnetroresistance in ferromagnetic 3d alloys. IEEE Trans. Magn., 11:1018, 2003.

Bibliography

Mills D. L. Ferromagnetic resonance relaxation in ultrathin metal films: The role of the conduction electrons. Phys. Rev. B, 68:014419, 2003.

Miltat J., Albuquerque G., and Thiaville A. An Introduction to Micromagnetics in the Dynamical Regime. Springer, 2002.

Mistral Q., Kim J. V., Devolder T., Crozat P., Chappert C., Katine J. A., Carey M. J., and Ito K. Current-driven microwave oscillations in current perpendicular-to-plane spin-valve nanopillars. Appl. Phys. Lett., 88:192507, 2006.

Montigny B. and Miltat J.. Micromagnetic simulations of current-induced microwave excitations. J. Appl. Phys., 97:10C708, 2005.

Moodera J.S., Nassar J., and Mathon G. Spin-tunneling in ferromagnetic junctions. Annu. Rev. Mater. Sci., 29:381, 1999.

Myers E. B., Ralph D. C., Katine J. A., Louie R. A., and Buhrman R. D. Current-induced switching of domains in magnetic multilayer devices. Science, 285:867, 1999.

Nagaev E. L. Colossal magnetoresistance and phase separation in magnetic semiconductors. Imperial College Press, 2002.

Parkin S. S. P. Ultrathin Magnetic Structures II. Springer-Verlag, 1994.

Parkin S. S. P. The magic of magnetic multilayers- introduction to this group of papers. IBM Journal of Research and Development, 42:1, 1998.

Persson J., Zhou Y., and Akerman J. Phase-locked spin torque oscillators: Impact of device variability and time delay. J. Appl. Phys., 101:09A503, 2007.

Petit S., Baraduc C., Thirion C., Ebels U., Liu Y., Li M., Wang P., and Dieny B. Spin-torque influence on the high-frequency magnetization fluctuations in magnetic tunnel junctions. Phys. Rev. Lett., 98:077203, 2007.

Pippard A. B.. Magnetoresistance in metals. Cambridge University Press, 1989.

Pribiag V. S., Krivorotov I. N., Fuchs G. D., Braganca P. M., Ozatay O., Sankey J. C., Ralph D. C., and Buhrman R. A. Magnetic vortex oscillator driven by d.c. spin-polarized current. Nature Phys., 3:498, 2007.

Bibliography

Pufall M. R., Rippard W. H., Kaka S., Silva T. J., and Russek S. E. Frequency modulation of spin-transfer oscillators. Appl. Phys. Lett., 86:082506, 2005.

Pufall M. R., Rippard W. H., Russek S. E.,Kaka S., and Katine J. A.. Electrical measurement of spin-wave interactions of proximate spin transfer nanooscillatiors. Phys. Rev. Lett., 97:087206, 2006.

Ralph D. C. and Stiles R. D. Spin transfer torque. J. Magn. Magn. Mater., 320:1190, 2008.

Rippard W. H., Pufall M. R., Kaka S., Russek S. E., and Silva T. J.. Directcurrent induced dynamics in cofe/nife point contacts. Phys. Rev. Lett., 92:027201, 2004.

Rippard W. H., Pufall M. R., Kaka S., Silva T. J., and Russek S. E. Injection locking and phase control of spin transfer nano-oscillators. Phys. Rev. Lett., 95:067203, 2005.

Rippard W. H., Pufall M. R., and Russek S. E.. Comparison of frequency, linewidth, and output power in measurements of spin-transfer nanocontact oscillators. Phys. Rev. B, 74:224409, 2006.

Sakurai J. J. Morden Quantum Mechanics. Addison Wesley, 1994.

Sankey J. C., Braganca P. M., Garcia A. G. F., Krivorotov I. N., Buhrman R. A., and Ralph D. C. Spin-transfer-driven ferromagntic resonance of individual nanomagnets. Phys. Rev. Lett., 96:227601, 2006a.

Sankey J. C., Braganca P. M., and Garcia A. G. F. Spin-transfer-driven ferromagnetic resonance of individual nanomagnets. Phys. Rev. Lett., 96:227601, 2006b.

Sankey J. C., Krivorotov I. N., Kiselev S. I., Braganca P. M., Emley N. C., Buhrman R. A., and Ralph D. C. Mechanisms limiting the coherence time of spontaneous magnetic oscillations driven by dc spin-polarized currents. Phys. Rev. B, 72:224427, 2005.

Savitzky A. and Golay M. J.E. . Smoothing and differentiation of data by simplified least squares procedures. Anal. Chem., 36:1627, 1964.

Serpico C., Bertotti G., d'Aquino M., Bonin R., and Mayergoyz I. D.. Transient dynamics leading to self-oscillations in nanomagnets driven by spin-polarized currents. IEEE Trans. Magn., 41:3100, 2005.

Silva T. J. and Rippard W. H. Developments in nano-oscillators based upon spin-transfer point-contact devices. J. Magn. Magn. Mater., 320:1260, 2008.

Bibliography

Skrotskii G. V. The landau-lifshitz equation revisited. Sov. Phys. Usp., 27:977, 1984.

Slavin A. N. and Tiberkevich V. S.. Current-induced bistability and dynamci range of microwave generation in magnetic nanostructures. Phys. Rev. B, 72:094428, 2005.

Slonczewski J. C. Conductance and exchange coupling of two ferromagnets separated by a tunneling barrier. Phys. Rev. B, 39:6995, 1989.

Slonczewski J. C. Current-driven excitation of magnetic multilayers. J. Magn. Magn. Mater., 159:L1, 1996.

Slonczewski J. C. Excitation of spin waves by an electric current. J. Magn. Magn. Mater., 195:261, 1999.

Slonczewski J.. Currents and torques in metallic magnetic multilayers. J. Magn. Magn. Mater., 247:324, 2002.

Smith N., Katine J. A., Childress J. R., and Carey M. J.. Thermal and spintorque noise in ccp (tmr and/or gmr) read sensors. IEEE Trans. Magn., 42:114, 2006.

Stiles M.D. and Zangwill A.. Anatomy of spin-transfer torque. Phys. Rev. B, 66:014407, 2002.

Sun J. Z.. Spin-current interaction with a monodomain magnetic body: A model study. Phys. Rev. B, 62:570, 2000.

Tiberkevich V., Slavin A. N., and Kim J. V.. Microwave power generated by a spin-torque oscillator in the presence of noise. Appl. Phys. Lett., 91:192506, 2007.

Tserkovnyak Y., Brataas A., and Bauer G. E. E.. Enhanced gilbert damping in thin ferromagnetic films. Phys. Rev. Lett., 88:117601, 2002.

Tserkovnyak Y. , Brataas A.,Bauer G. E. W., and Halperin B. I. Nonlocal magnetization dynamics in ferromagnetic heterostructures. Rev. Mod. Phys., 77:1375, 2005.

Tsoi M., Jansen A. G. M., Bass J., Chiang W. C., Seck M., Tsoi V., and Wyder P. Excitation of a magnetic multilayer by an electric current. Phys. Rev. Lett., 80:4281, 1998.

Tsoi M. Magnetic tunnel junctions: Spin-torque measured up. Nature Physics, 4:17, 2008.

Tulapurkar A. A., Suzuki Y., and Fukushima A. Spin-torque diode effect in magnetic tunnel junctions. Nature, 438:339, 2005.

Bibliography

TUNAMOS. Tunable NAno-Magnetic OScillators for integrated transceiver applications. http://www.imec.be/tunamos/public/index.html, 2008.

Verluijs J. J., Bari M. A., and Coey J. M. D. Magnetoresistance of half-metallic oxide nanocontacts. Phys. Rev. Lett., 87:026601, 2001.

von Helmolt R., Wecker J., Holzapfel B., Schultz L., and Samwer K. Giant negative magnetoresistance in perovskitelike labamno ferromagnetic films. Phys. Rev. Lett., 71:2331, 1993.

von Helmolt R., Wecker J., Samwer K., Haupt L., and Barner K. Intrinsic giant magnetoresistance of mixed valence la-a-mn oxide (a=ca,sr,ba). J. Appl. Phys., 76:6925, 1994.

Xi H. W. and Lin Z.. In-plane magnetization dynamics driven by spin-polarized currents in magnetic nanostructures. Phys. Rev. B, 70:092403, 2004.

Xi H., Yang Y. Z., Ouyang J., Shi Y. M., and Gao K. Z.. Spin waves excited by dc currents injected into single ferromagntic thin films. Phys. Rev. B, 75:174411, 2007.

Xiao J., Zangwill A., and Stiles M.D.. Boltzmann test of Slonczewski's theory of spin-transfer torque. Phys. Rev. B, 70:172405, 2004.

Xiao J. and Zangwill A. Macrospin models of spin transfer dynamics. Phys. Rev. B, 72:014446, 2005.

Xiao J., Zangwill A., and Stiles M.D.. A numerical method to solve the Boltzmann equation for a spin valve. Euro. Phys. J. B, 59:415, 2007.

Yang Z., and Zhang S. Magnetoresistance and resistance of magnetic nanoconstriction. Phys. Rev. B, 70:094404, 2004.

Zhou Y., Persson J., and Akerman J. Intrinsic phase shift between a spin torque oscillator and an alternating current. J. Appl. Phys., 101:09A5101, 2007.

Zhou Y., Guan B., Shin F. G., and Akerman J.. Capacitance Enhanced Synchronization of Pairs of Spin-Torque Oscillators. AMC 2008, 2008.

Zhu X. C., Zhu J. G., and White R. M.. Spin transfer excited regular and chaotic spin waves in current perpendicular to plane spin valves. J. Appl. Phys., 95:6630, 2004.

Bibliography

Zimmler M. A., Ozyilmaz B., Chen W., Kent A. D., Sun J. Z., Rooks M. J., and Koch R. H. Current-induced effective magnetic fields in Co/Cu/Co nanopillars. Phys. Rev. B, 70:184438, 2004.

Zutic I., Fabian J., and Sarma S. D. Spintronics: Fundamentals and applications. Rev. Mod. Phys., 76:323, 2004.